Scuola Internazionale Superiore di Studi Avanzati - Trieste

Quantum Monte Carlo simulations of two dimensional ^{3}He: low-density gas-liquid coexistence on substrates and iterative backflow wave functions for strongly correlated systems

Candidate: Michele Ruggeri

Supervisor: Saverio Moroni

30.10.2015
SISSA - Via Bonomea 265 - 34136 Trieste - Italy

Abstract

In this thesis we show results of Quantum Monte Carlo simulations for fluid ^{3}He in the ground state. We studied ^{3}He in a quasi two dimensional environment [1] and we designed a new class of trial wave functions for strongly correlated fermions [2].

^{3}He is a typical example of Fermi liquid, and is the focus of several theoretical and experimental studies; since two dimensional ^{3}He in the ground state is believed to be a homogeneous liquid up to freezing, two dimensional ^{3}He is the ideal system to study the effects of correlation in a wide density range. In this thesis we have worked in two regimes: we studied the behaviour of low density ^{3}He adsorbed on substrates and we designed a new class of trial wave function to be used in the strongly correlated, high density systems.

While great focus has been devoted to study the strongly correlated regime at high density, some important questions about the low density behaviour of this system still have to be addressed. Recent experimental data were interpreted as the evidence of the formation of self bound puddles of liquid ^{3}He adsorbed on graphite [38, 39]; it was also argued that the the appearance of this liquid phase does not depend on the substrate, but is an intrinsic property of two dimensional ^{3}He. This is in stark contrast with theoretical studies, that exclude the presence of a self bound liquid.

We performed Quantum Monte Carlo simulations, using the Variational Monte Carlo and the Fixed Node - Diffusion Monte Carlo methods, to investigate the presence of a low density liquid phase in two dimensional ^{3}He and in ^{3}He adsorbed on alkali, magnesium and graphite substrates. Our results exclude the formation of a self bound liquid in the strictly two dimensional environment, while in the presence of substrates the situation changes; on weakly attractive substrates the formation of a liquid phase is indeed possible, while on stronger substrates, that are closer approximations of the two dimensional system, we can't observe any liquid. We find out however that the corrugation a the substrate helps the stabilization of a liquid phase, and can lead to phase coexistence of different fluid phases even on a substrate as strong as graphite.

When performing Quantum Monte Carlo simulations it is crucial to have good trial wave functions. Designing good wave functions on the other hand is a hard task, especially when we study Fermi liquids at high density. Including backflow transformations has proven to significantly increase the quality of trial wave functions for Fermi liquids, especially at high density, but some results still show a poor quantitative agreement with experimental data for example for the spin polarization of ^{3}He [18].

We introduce a new class of trial wave functions for strongly correlate Fermi systems. These wave functions are based on iterated backflow transformations and on the

introduction of correlations between backflow coordinates. While exact results are usually not available in Quantum Monte Carlo simulations of Fermi system our iterative backflow procedure allows to define a set of increasingly accurate wave functions that can be used to obtain both a strict upper bound and a strict lower bound to the exact ground state energy, and have an estimate of the exact energy. While the inclusion of iterative backflow transformations leads to slower computations the overall computational cost of the simulations scales as the cube of the size of the simulated system; this is the same size scaling of wave function with just one backflow transformation that are routinely employed.

We used these wave functions to study two dimensional ^{3}He at freezing. We could obtain variational energy estimates that are significantly lower than the ones available in literature; moreover the upper and lower bound we could obtain for ^{3}He allowed us to give an estimate for the ground state energy that is in good agreement with exact data obtained with the Transient Estimate technique.

Having seen the good results that can be obtained using these wave functions we used them to simulate another system, three dimensional ^{4}He; we studied this system in different conditions, at negative pressure, at equilibrium and at freezing; in all cases we could obtain variational energies that are lower than the ones obtained using Shadow Wave Functions, and the upper and lower bounds for the energy are consistent with exact Diffusion Monte Carlo data. The good results we obtained in the study of a Bose system suggest that the iterative backflow transformations could find applications that can go well beyond the simulations of strongly correlated fermions.

Contents

Introduction

Helium systems provide one the most typical example of quantum fluids. Helium in fact does not solidify in the ground state without the presence of a large external pressure. This is due to the fact that helium atoms have a very weak polarizability and a very small mass. This means on one hand that they are only weakly interacting and on the other have a large kinetic energy even in the ground state. Both these effects hinder solidification. The delocalization of the atoms in a quantum fluid leads to a very large importance of indistinguishability and the strong repulsion at short distances leads to strong correlations in the high density regime [4].

In this thesis we focus on the study of fluid ^{3}He, performed with Quantum Monte Carlo simulations. Our work can be divided in two parts: the study of low density ^{3}He in a (quasi) two dimensional environment and the design, implementation and first applications of a new class of trial wave functions for strongly correlated Fermi systems.

The general consensus is that in two dimensions ^{3}He in the ground state is a homogeneous gas at all densities, but there is no conclusive evidence of this behaviour; recent experimental data [38, 39] suggest the formation of a self bound liquid in ^{3}He adsorbed on a graphite substrate, in a temperature range between 4 and 80 mK. This result is especially interesting, as theoretical computations exclude the presence of a liquid phase for two dimensional ^{3}He [22, 13].

We note however that most of the theoretical computations used to describe this system focus on an idealized, strictly two dimensional system. Here we consider a more realistic quasi two dimensional environment, in which the interaction of helium atoms with a substrate, the corrugation of the substrate or the presence of multiple helium layers are explicitly taken into account.

In our computations we use Quantum Monte Carlo simulations. Quantum Monte Carlo simulations are a class of stochastic computation techniques designed to deal with problem in quantum mechanics. They are extremely versatile, and are used to obtain remarkably accurate results for a wide range of problems. While these techniques are powerful they do have some limitations. Fermi systems for instance are particularly difficult to study with these methods. Projector Monte Carlo techniques in fact can in principle be used to exactly compute physical quantities at the ground state for any quantum system, but in practice they can be used only when dealing with Bose systems in the ground state. When dealing with Fermi systems instead one has to resort to variational estimates, the reason being the sign problem.

The results obtained with ground state Quantum Monte Carlo simulations heavily

depend on the quality of the trial wave functions that are used to describe the physical system under analysis. Part of our work was to design a new class of wave functions to deal with strongly correlated Fermi fluids. The idea at the basis of these new wave functions is that backflow transformations, routinely used in simulations of Fermi systems, can be iterated; wave functions including more iterations give a more accurate description of interparticle correlations and more accurate nodal surfaces that greatly improves the accuracy of Quantum Monte Carlo results.

In the first chapter of this thesis we shall review previous results on (quasi) two dimensional ^{3}He; we will discuss both theoretical models and numerical computations, as well as the main experimental results involving ^{3}He adsorbed on substrates. We will focus in particular on recent heat capacity measurements that suggest the presence of self bound liquid ^{3}He adsorbed on graphite.

In the second chapter we review the Quantum Monte Carlo techniques we used in our simulations: Variational Monte Carlo and Diffusion Monte Carlo. The sign problem is also discussed, along with the Fixed Node approximation.

In the third chapter we show results of simulations of quasi two dimensional ^{3}He; we start by determining the low density equation of state for a strictly two dimensional system and then we include a substrate. At first we introduce weakly interacting substrates, i.e. alkali metals and magnesium, then we use graphite. When simulating graphite we shall discuss the role of the corrugation of the substrate on the properties of the adsorbed helium; we also study the behaviour of the second layer of ^{3}He adsorbed on a graphite structure.

In the fourth chapter we introduce a new class of trial wave functions, based on the iterative application of the backflow transformations that already routinely used in the simulations of Fermi systems. We shall define our wave function, estimate their computational cost and show how they can be used to estimate the ground state energy of a Fermi system. We then use them to simulate two physical systems: two dimensional ^{3}He at freezing density and three dimensional ^{4}He at different densities; the bosonic simulations were performed even if exact results are already available for Bose systems to evaluate the quality of our new wave functions, and to assess the accuracy of the extrapolations of exact ground state energies.

We finally present some final remarks and an outlook for future studies.

Chapter 1

Two dimensional ^{3}He

Before addressing the main topics of this thesis it is important to review some existent results on two dimensional ^{3}He. We discuss some theoretical model used to describe fluid ^{3}He, such as the Landau Fermi liquid theory, and present numerical results. We also present experimental data on ^{3}He adsorbed on substrates, focusing on the low density behaviour.

1.1 Theoretical description

Providing a theoretical prediction of physical properties of ^{3}He is not an easy task; the strong correlations that are present at high densities are in fact extremely difficult to take into account [3]. The most successful phenomenological model used to describe Fermi liquids and to interpret experimental data is the Landau Fermi liquid theory.

The crudest approximation one can make when studying a fluid, especially at very low density, is to treat it like an ideal gas, so that analytical computations can be performed. This of course give poor results in a strongly interacting system like ^{3}He but observing experimental data one can observe that the qualitative behaviour of physical system is not that different from the predictions of the ideal Fermi gas model; for example the specific heat is linear in temperature at low temperatures, even if the slope is different from the one predicted by the theory. The disagreement between theory and experiment grows larger as the density of the system increases.

A better description of fluid ^{3}He is given by the Landau Fermi liquid theory [5]. The basis of the Landau theory is that it is possible to build a one on one correspondence between the states of an ideal and an interacting Fermi system. Let us consider a non interacting system; the ground state is the Fermi sphere, and each state can be uniquely determined by stating the occupation number of each single particle state. This is possible because low energy excitations can be written in term of creations of particles and holes. Now we imagine to switch on interactions. If we adiabatically turn on the interaction we obtain in the end the states of the fully interacting system. The point is that each non interacting state corresponds to a single fully interacting state, and the ordering of the states is not affected, as the states have the same symmetry. The main consequence of this correspondence is that the states of the interacting system

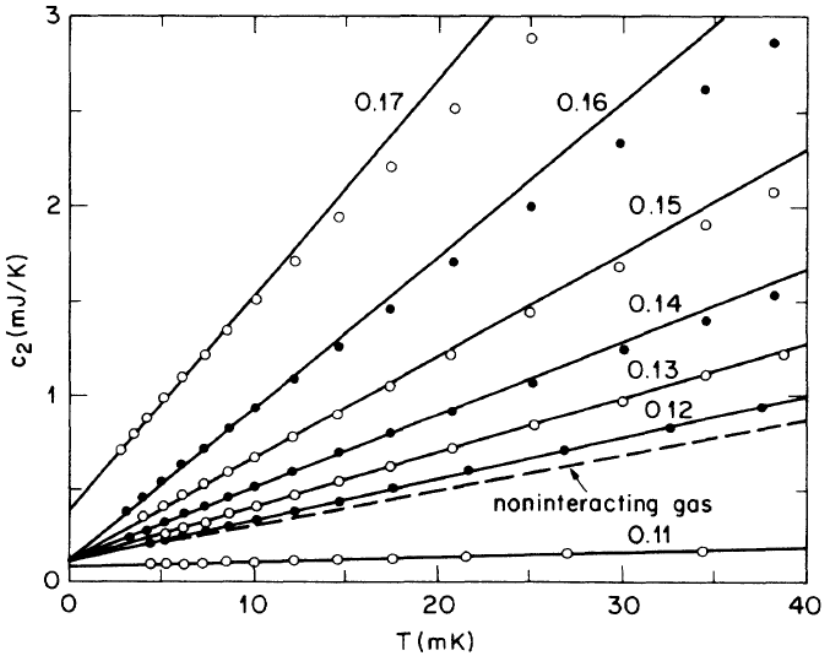

Figure 1.1: Heat capacity of the second layer of ^{3}He adsorbed on graphite [33]. Discrepancies between experimental data and the behaviour of the ideal Fermi gas are evident. Each data set refers to a different coverage. The numbers refer to the total coverages, expressed in atoms/Å^2

.

can be described using the occupation numbers of single particle states of an ideal gas of quasiparticles; we can thus compute thermodynamic quantities for an interacting system using the theory of the non interacting Fermi gas. The only thing that really changes is that in all the quantities there is some renormalization that is described by the introduction of the phenomenological Landau parameters, as the effective mass m^* and the $F-$parameters. For example using the Landau theory the specific heat and the spin susceptibility in two dimensions are

$$C_V = \frac{m^*}{m} C_V^{(0)} = \frac{\pi m^* A k_B^2}{3\hbar^2} T \tag{1.1}$$

and

$$\chi = \frac{1}{1+F_0^A} \frac{m^*}{m} \chi^0 = \frac{A}{\pi\hbar^2} \frac{m^*}{1+F_0^A} \tag{1.2}$$

where the superscript (0) refers to the properties of a non interacting system, m^* is the effective mass, T is the temperature, A is the area of the sample and F_0^A is one of the Landau parameters. The main problem of Landau theory is that it is phenomenological, in the sense that all the Landau parameters have to determined experimentally.

During the years lattice models, based on the Hubbard model [6], were also used to give a description of ^{3}He [7], especially to explain magnetic anomalies. We mention for example the paramagnon model [8] or the quasi-localized model [9].

Several Quantum Monte Carlo computations were performed to study two dimensional ^{3}He, using both the Variational Monte Carlo technique [10] and the Diffusion Monte Carlo technique [11] with the Fixed Node approximation [12]. The equation of state in two dimensions for ^{3}He, ^{4}He and a hypothetical mass 3 boson was determined with Variational and Diffusion Monte Carlo [13], and from these equations of state we can note strong differences in the behaviour of the different helium species. In two dimensions ^{4}He forms a self bound liquid [14] while ^{3}He does not; it is interesting to look at the equation of state of the mass 3 boson: this hypothetical particle forms a bound liquid in spite of its very light mass; it is then evident that the real source of the different behaviour of the two helium isotopic species is not the difference in mass but their different particle symmetry. We show the computed equations of states in figure 1.2. The possibility of the formation of a self bound liquid was also studied via variational simulations of puddles of helium [14]; Variational Monte Carlo simulations of system of different sizes in a circular box with hard walls were performed, both for ^{4}He and for ^{3}He, introducing a form factor to model the size and shape of the puddles. These computations predict the formation of puddles for bosonic systems (that are very weakly bound in the case of mass 3 boson) while the existence of puddles for fermionic ^{3}He is excluded.

When comparing numerical results with experiment for two dimensional system one should take care: in fact it is of course impossible to realize in laboratory a strictly two dimensional environment, and experiments are performed adsorbing helium atoms on a suitable substrate (for example graphite). Experimental measures of properties of helium liquid films in general seem largely independent of the substrate, so comparisons between experiments and models in two dimensions are routinely made [21].

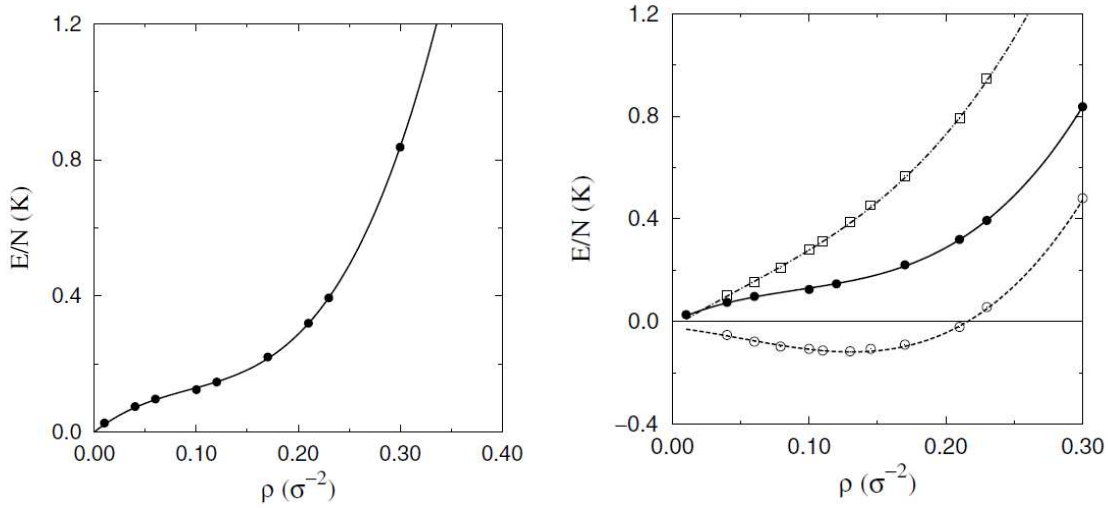

Figure 1.2: Left panel: equation of state obtained with Diffusion-Fixed Node Quantum Monte Carlo simulations for two dimensional ^{3}He. Right panel: comparison between Monte Carlo energies of ^{3}He (solid line) and mass three bosonic helium (circles); the squares are the sum of the boson energy and the Fermi gas kinetic energy [13], that gives a crude estimate of the fermionic equation of state (Wu-Feenberg expansion) [15].

Even if effective mass and susceptibility enhancement seem substrate independent [41] the presence of a substrate can affect other properties of the adsorbed ^{3}He; for example the freezing density [33] or the magnetic properties of the solid phase [35] seem to depend on the substrate. In the case of the formation of a puddles of liquid at low density [38, 39] we can argue that the zero point motion along the z direction of the helium atoms, the change of the effective interaction between helium, and the presence of the corrugation could help the stabilization of a liquid phase[24].

A theoretical work focused on helium on a graphite substrate was made by Novaco and Campbell in 1975 [22]; in their computations the variational principle was used to determine the equation of state of a quasi two dimensional helium system in the presence of a graphite substrate. It was found that the effect of the substrate is very weak and helium behaves mostly as in a strictly two dimensional system: ^{4}He forms a weakly self bound liquid, while ^{3}He doesn't. We show the equation of state in figure 1.3.

Another variational computation was made by Miller and Nosanow [23] using the quantum theory of corresponding states, again in a strictly two dimensional effective environment. It is predicted here that in Fermi system a liquid-gas coexistence is possible, but due to the approximations introduced the results of these computations are not conclusive.

The behaviour of a strictly two dimensional ^{3}He system and a three dimensional system of ^{3}He atoms adsorbed on a graphite substrate was compared by Brami, Joly and Lhuillier using Variational Monte Carlo simulations [24]; very significant differences between the two systems were found, most remarkably it was found out that in presence of a substrate ^{3}He forms a self bound liquid. It should be noted however that the results

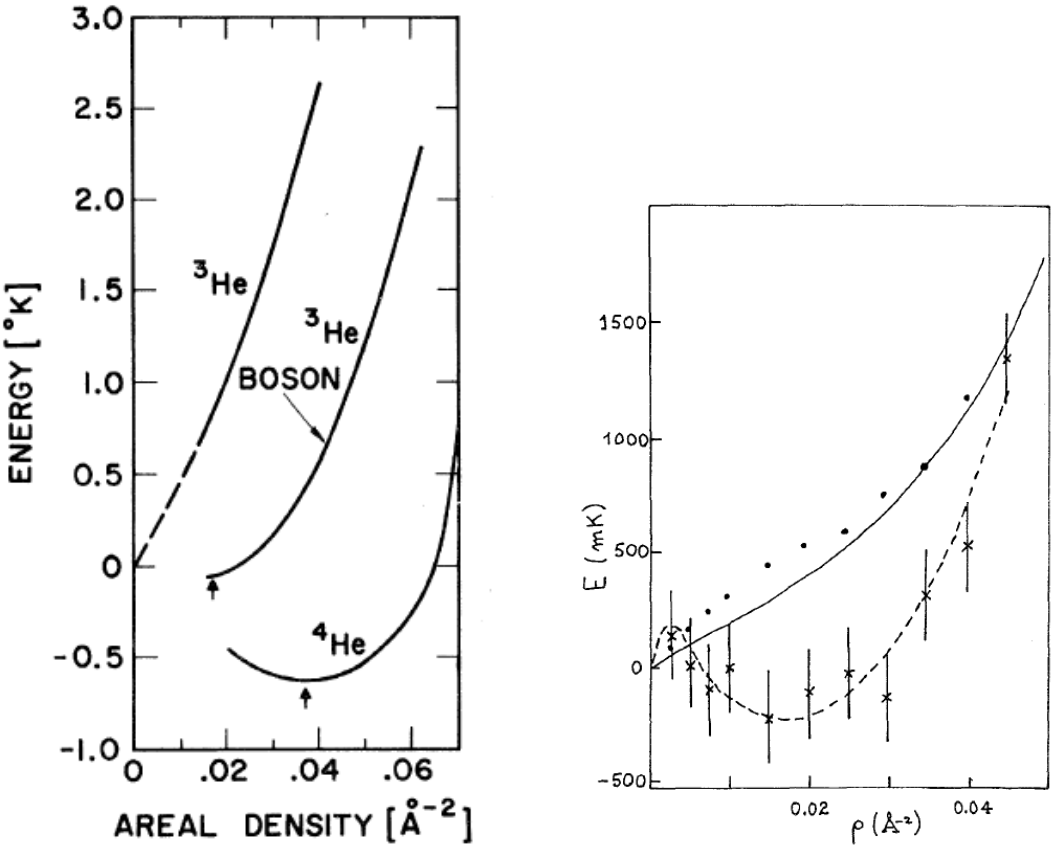

Figure 1.3: Left: Variational equation of state ^{3}He, both fermionic and bosonic and ^{4}He adsorbed on graphite from [22]. We can see the different behaviour of the three systems: the equation of state for ^{4}He displays a large minimum, indicating the presence of a self bound liquid. Bosonic ^{3}He displays a weakly bound liquid phase while in the case of fermionic ^{3}He the equation of state is monotonically increasing, meaning that the system is always a homogeneous gas. Right: Variational Monte Carlo equation of state for ^{3}He from [24]; the points refer to a strictly two dimensional system, the crosses to a system adsorbed on graphite; the dashed line is a spline interpolation of these data to guide the eye; the solid line is the equation of state for 2D helium from [22].

of the energy estimates for the quasi two dimensional system could not be reproduced [14, 25].

The evaluation of the energy as a function of the spin polarization is another complicated issue, at least at high density. In strongly correlated fluids the dependence of the energy on the polarization is in general very weak, and the fixed node approximation used in the vast majority of fermionic Quantum Monte Carlo simulations can give a significant bias to the energy, especially at high density [16, 17, 18, 19]. An exact technique, the Transient Estimate technique [19], can be used to obtain exact results for the energy as a function of the polarization, and to estimate the spin susceptibility of two dimensional ^{3}He [20]. While this technique is computationally very demanding the obtained results were much more accurate than the fixed node results; fixed node simulations performed with standard wave functions in fact may not even reproduce the Pauli paramagnetism of liquid helium, instead predicting a spin polarized ground state at high density [20]. In order to obtain more accurate results better wave functions have to be employed [18].

1.2 Experimental results: helium on substrates

A large literature exists on experimental studies on helium systems adsorbed on substrates; mostly the experiments consist in measurements of thermal capacity and spin susceptibility, from which it is possible to evaluate the effective mass and the Landau parameters.

In this section we are going to review experimental data on quasi two dimensional helium adsorbed on graphite substrates; firstly we are going to discuss the properties of a graphite substrate and then we review experimental data. In this part we are going to follow the review by Godfrin and Lauter [26] and references therein. We conclude with the discussion of recent experiments dealing with the observation of a self bound liquid phase for ^{3}He adsorbed on graphite.

A large number of experiments has been performed adsorbing helium atoms on substrates made of Grafoil, i.e. exfoliated graphite. The interaction between helium atoms and the carbon substrate is a rapidly varying potential, strongly repulsive at short distance, when there is overlap between the electrons in the substrate and the ones in the helium atom, then displays a minimum and finally smoothly increases at large distances. An important feature of the graphite substrate is the corrugation: the interaction depends not only on the distance between substrate and atom, but also on the atomic position along the surface. The potential minimum for ^{3}He on graphite has a magnitude of about -200 K, while the corrugation, that has the same periodicity of the graphite substrate, has an amplitude of about 40 K. We emphasize that corrugation is a feature that is usually neglected in theoretical computations.

Since ^{3}He has a small mass, even in the ground state there is a substantial kinetic energy; this is also due to the strong localization inposed by the substrate along the z axis, according to the Heisenberg uncertainty principle. The binding energy is thus significantly smaller than the depth of the potential well, and is estimated to be about 136 K; the mean distance between the substrate and the ^{3}He is $\langle z \rangle = 2.88$ Å. We note

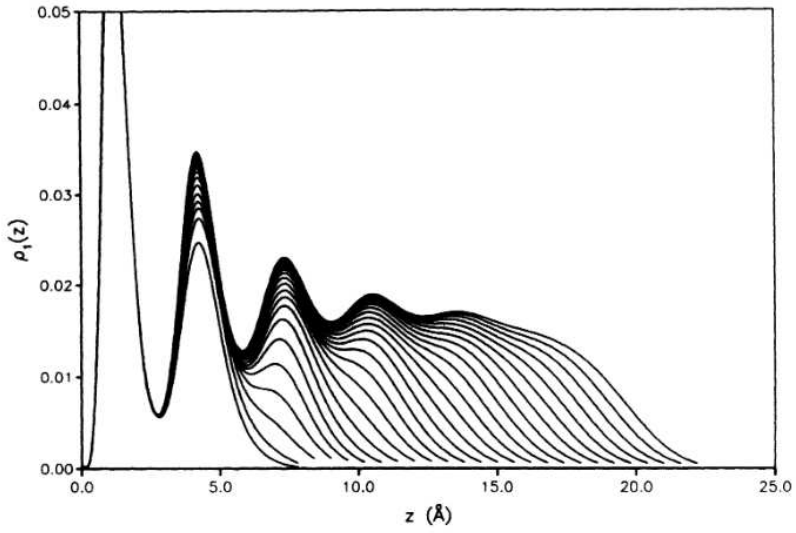

Figure 1.4: Density profile of helium atoms adsorbed on a strong substrate (such as graphite) for $n = 0.12$ to 0.39 atoms/Å2, as computed in [32].

that since ^{4}He atoms have a larger mass but the same interaction with the substrate, the adsorption energy in this case is larger, and the mean distance smaller, and so ^{4}He is viable as a preplating for experiments with ^{3}He films. The excited states of a ^{3}He atom in the graphite adsorption potential are well separated from the ground state, the energy gap between the first excited state and the ground state being of the order of 60 K.

The corrugation of the potential is not enough to localize a single atom in the plane; a helium atom can thus be approximately considered as a free particle in two dimensions. The presence of the corrugated substrate leads to an increase of the effective mass of helium atoms of about 3% [28]; we refer to this effective mass as the band mass m_B, to distinguish it from the effective mass m^* used in the Landau Fermi liquid theory.

The interaction between helium atoms is characterized by a strong short range repulsion and a weakly attractive long range tail, with a very shallow minimum; it can be modelled with a Lennard-Jones 6-12 potential, or with more sophisticated potentials such as the Aziz potentials [29, 30] or the SAPT2 potential [31]. The helium-helium interaction is significantly weaker than the interaction with the substrate; having a strong substrate has the effect of preventing the formation of three dimensional clusters and in general hinders the formation of self bound liquids.

We now discuss the low temperature phase diagram of ^{3}He on graphite, looking at the features of the system at progressively higher helium densities; the effect of the substrate and thus the quasi two dimensionality of the system is important only for the first two helium layers. Further layers in fact are much less defined, having a much larger overlap (as can be seen in figure 1.4, and in these cases a two dimensional description is not appropriate.

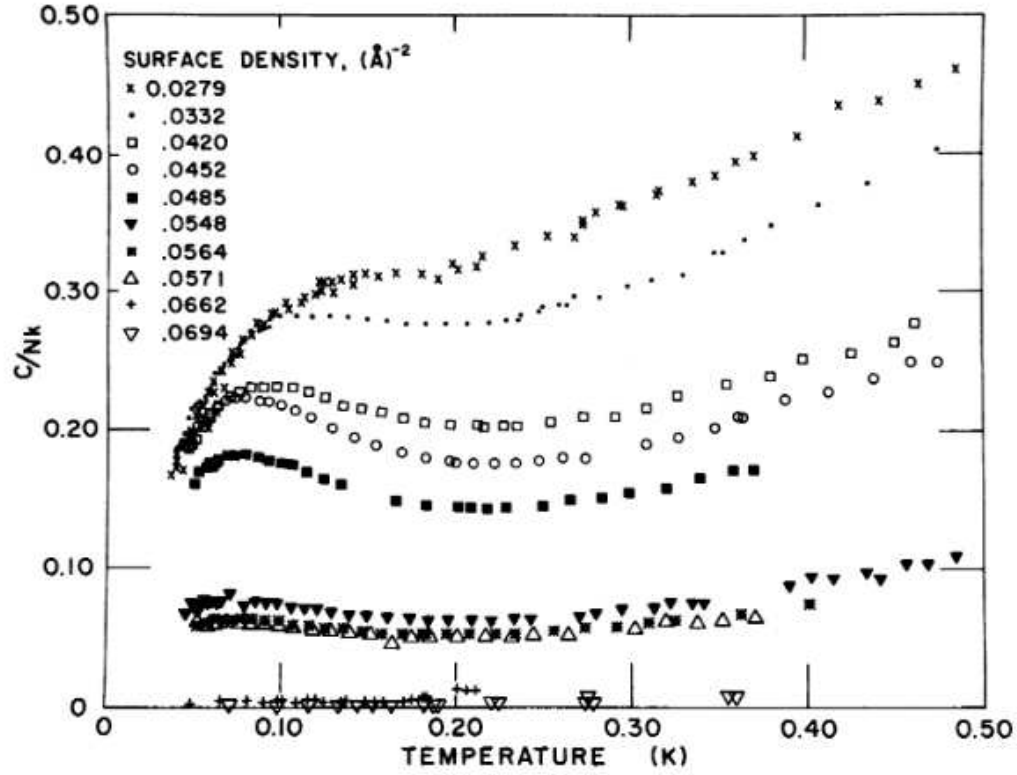

Figure 1.5: Heat capacity of the first layer of ^{3}He adsorbed on graphite, as a function of the temperature and for different coverages. For fluid films at low temperature the linear dependence predicted by Landau's Fermi liquid theory begins to be seen around 0.1 K; around 0.2 K a typical plateau can be observed. The commensurate phase displays a very low heat capacity.

The phase diagram is inferred by specific heat measurements [33]; in the fluid phase the specific heat is characterized by a linear dependence on T, while in solid phases there is a phonon contribution and a spin contribution. Anomalies in specific heat are explained with the presence of defects, especially at very low density, or phase transitions.

At extremely low densities (less than 0.002 Å^{-2}) helium atoms are mostly localized; the specific heat is solid-like, and the atoms are thought to form patches at substrate defects; the contribution of these atoms to thermal or magnetic properties of the sample has to be subtracted to the total specific heat of magnetization to obtain the properties of the solid and the liquid.

Increasing the density a homogeneous fluid phase is observed. We show in figure 1.5 the specific heat as a function of the temperature for the fluid phase.

At high temperatures, larger than 1 K, the specific heat is constant and has a value of Nk_B, as a classical fluid; at lower temperatures quantum effects lead to a plateau in the heat capacity that is close to that observed in bulk helium [34]. At low temperatures ($T < 0.1$K) quantum degeneracy effects are observed, and the specific

heat is linear in T, as predicted by Landau Fermi liquid theory. From the slope of the specific heat the effective mass m^* can be estimated as a function of the areal density ρ. The Fermi liquid nature of low temperature ^{3}He is confirmed by spin susceptibility measurements, that confirm the predictions of Landau theory and allow estimates of not only the effective mass but also the Landau parameter F_0^a. This is not a trivial result, as the applicability of Landau theory for a strongly interacting system is not obvious. Both the paramagnon [8] and the quasi localized [9] models are in rather good agreement with measures of effective mass and Landau parameter F_0^a.

The behaviour of fluid ^{3}He isn't however completely clear: the consensus is that the fluid is homogeneous down to zero temperature, but recent measurements suggest the existence of a self bound liquid at very low density [36, 37, 38, 39]. A transition to a phase with puddles of self bound liquid may be compatible with an anomaly in the specific heat present at very low temperatures (about 3 mK); we note however that this anomaly may be explained also by other phenomena, such as a superfluid transition or the freezing of localized spins.

At the density of about $\rho = 0.043$ Å^{-2} a fluid-commensurate solid phase coexistence begins. This solid phase is very stable, and its formation is due to the fact that even if the graphite potential is not strong enough to localize the atoms at low densities, the increased pressure in two dimensions is enough to induce the formation of a lattice. As correlations are especially important near solidification, this transition can be seen as a Mott correlation-induced transition [40]. The first solid phase that is found is a commensurate solid phase, with a triangular lattice with one helium atom every three sites of the graphite lattice. This registered "1/3" phase is quite commonly found in gases adsorbed on graphite.

At higher coverages in the phase diagram appears a complex region, in which several stable commensurate phases exist. This is made possible by the strong corrugation of the graphite substrate and the formation of domain walls.

At coverages higher than 0.078 Å^{-2} helium atoms form a triangular incommensurate lattice; the decoupling from the graphite comes from the increase in zero point energy as the density increases, that strongly reduces the effects of correlations. Here two main contribution to the specific heat can be measured: at temperature larger that a few mK we can see a contribution proportional to T^2/Θ_D^2, due to phonons; at very low temperatures instead the dominating contribution is due to the ordering of nuclear spins. This contribution is proportional to T^{-2}. This two features can be seen very clearly in a log-log plot as the one in figure 1.6.

At densities of the order of 0.108 Å^{-2} we can observe promotion of atom to a second layer. The first layer provide a smooth, weakly attractive substrate, to the atoms in the second layer, with a binding energy of about 25 K. The second layer at high temperatures displays a quantum non degenerate Fermi fluid behaviour, like bulk ^{3}He. Again in specific heat measurements a plateau can be observed at temperatures around 0.1 K. At lower temperatures, about up to 50 mK, the degenerate character becomes evident, and a heat capacity which is linear in the temperature can be observed, as predicted by Landau theory. Here an excess specific heat is observed. This term is independent on the coverage, and it may be due to spin fluctuations. In general we

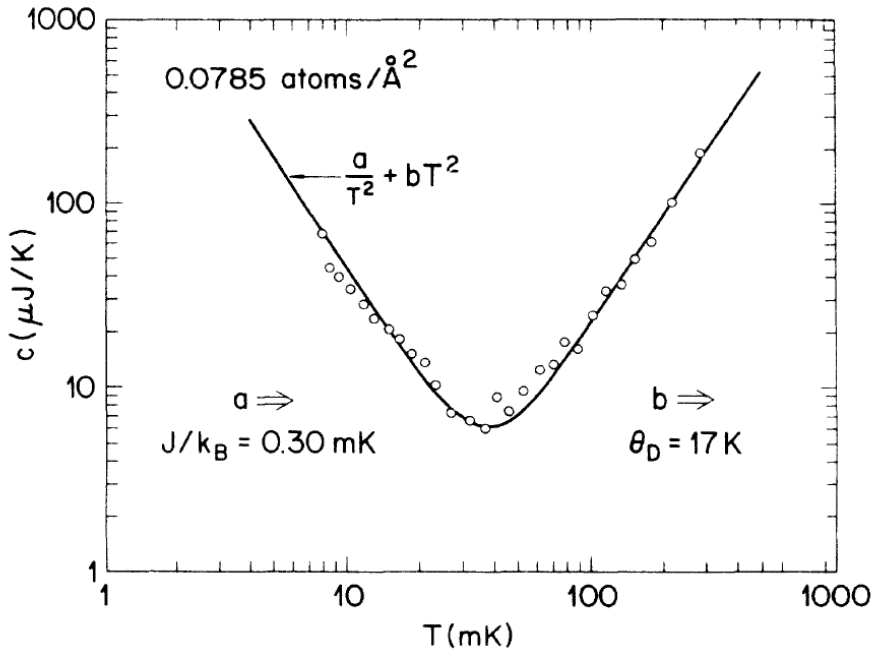

Figure 1.6: Log-log plot of the heat capacity of an incommensurate solid monolayer ^{3}He adsorbed on Grafoil; below 30 mK the heat capacity is dominated by nuclear spins, above by phonons [33]

can say that the properties of the fluid phase do not depend much on the substrate: magnetic properties, effective mass and Landau parameters do not change much if we consider the first monolayer, the second monolayer or a monolayer adsorbed on a ^{4}He preplating, or even with a HD preplating [41, 42]. The magnetic susceptibility is always well described by a modified Fermi gas expression. The similarity of experimental measurements obtained in different environments can be observed in figure 1.7.

The fluid phase in the second layer is thought to be homogeneous, but again it is not possible to completely exclude the formation of a self bound liquid at low density.

Further increase in density has the effect of solidifying the second layer.

The first solid phase is thought to be triangular and commensurate, even if there is no direct proof for this assumption. This assumption is anyway reasonable as for its density is very low, and at this density no incommensurate phase exists in the first layer, not even for the heavier ^{4}He.

In the second layer effects due to graphite corrugation are strongly suppressed by the first helium layer; the commensuration of the solid file in the second layer here is intended with respect to the first solid ^{3}He layer.

Increasing the density of the second layer leads once again to the coexistence of several commensurate phases, and eventually to the formation of a solid which is incommensurate with respect to the first solid layer.

We show in figure 1.8 phase diagrams for the first two layers of a ^{3}He film on a graphite substrate [33]. The phase separations are obtained from specific heat data,

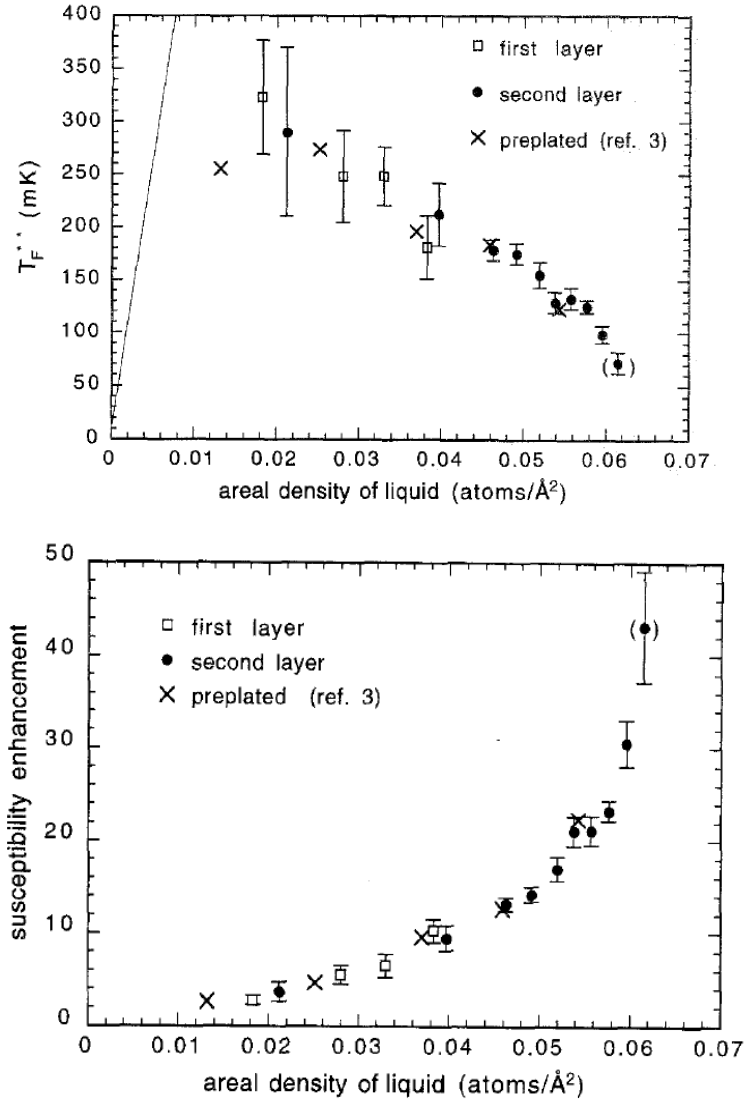

Figure 1.7: Effective Fermi temperature and susceptibility enhancement as functions of the liquid areal density of ^{3}He adsorbed on graphite [41], obtained with NMR measurements.

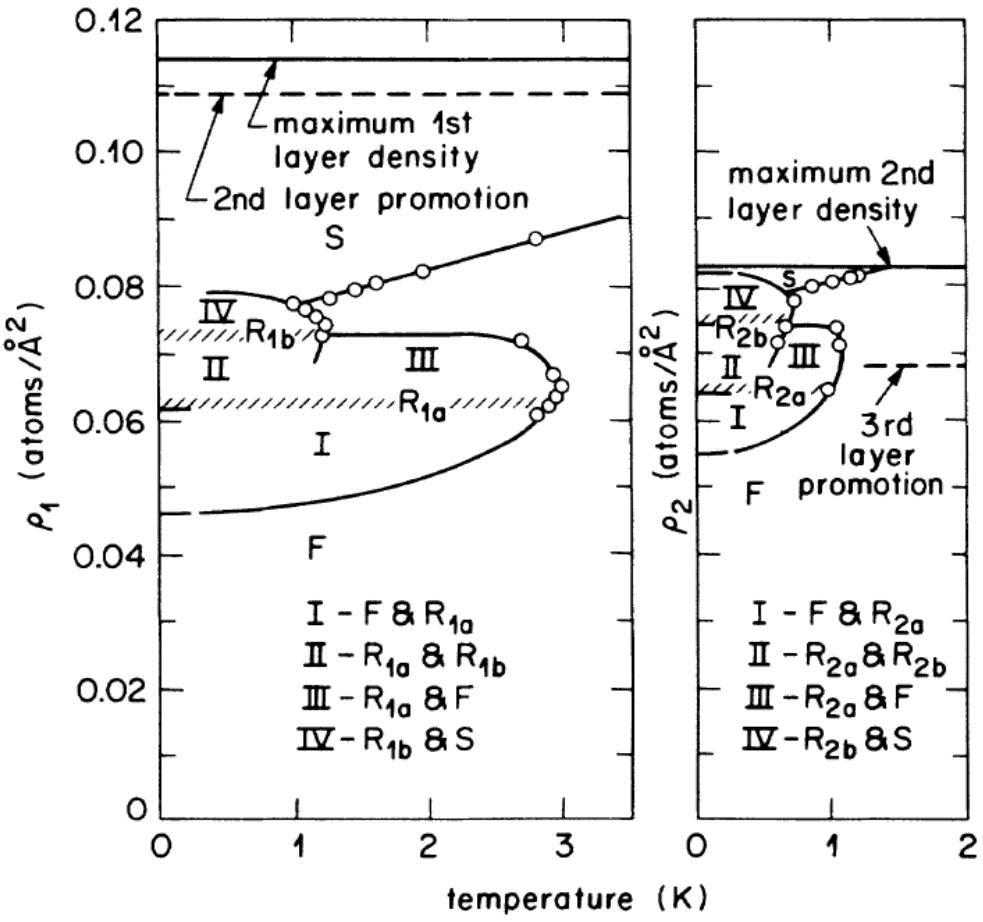

Figure 1.8: Phase diagrams for the first and second layers of ^{3}He adsorbed on graphite. The label F, R, and S refer to fluid, registered solid and incommensurate solid respectively. Roman numerals refer to coexistence regions. Data points refer to locations of heat capacity peaks [33].

and the similarity between the two leads to the assumption that the phase inside these boundaries are equivalent. We have to note however that in the first layer the registered phase is commensurate with the graphite, while the registered phase in the second layer is commensurate with the first layer: the lower melting temperature here reflects the much smaller corrugation of the substrate.

Further coverage increase leads to the formation of more layers, that display very large overlap and no sign of solidification; the overlap between these layers is much larger than the one between the first two, so that the definition of layers is in this case somewhat blurred; here we are not going to discuss the properties of these thick ^{3}He films. For further information we refer to the experimental work by Greywall [33], or the review by Godfrin and Lauter [26].

We emphasize that the behaviour of the low density fluid is not clear: the general

consensus in the past was that the ^{3}He films is a homogeneous fluid in the ground state, but some experimental results suggest the presence of puddles of a self bound liquid. The formation of these puddles was firstly suggested by Gasparini [36, 37]. Measuring the heat capacity of a mixture of ^{4}He and ^{3}He at very low ^{3}He densities he observed the linear dependence on T predicted by Landau theory

$$C = \frac{k_B^2 \pi}{3\hbar^2} m^* A T = \gamma T \tag{1.3}$$

where k_B is Boltzmann constant, m^* is the effective mass and A is the area available to the fluid. The slope of the specific heat as a function of the temperature should be constant for homogeneous fluids, as A is fixed and the effective mass at very low densities is mostly constant; instead the measured slope is much smaller than expected. He argued that this reduction can be explained by a phase separation, in which we have a condensed phase, with the formation of puddles and a very diluted homogeneous phase. The condensation has the effect of lowering the surface available to the fluid, effectively decreasing the slope of the heat capacity. This effect was eventually shown to be due to the substrate, and it is not a property of the ^{3}He film [43].

Chan et al. studied the superfluidity of ^{4}He in presence of a ^{3}He film [44]; it is observed that the presence of the fermionic isotope suppresses the superfluidity of ^{4}He. This suppression is thought to be due to the condensation of ^{3}He in a 2D liquid, as in proximity of puddles of liquid ^{3}He in fact ^{4}He forms halos of normal liquid. As the density of ^{3}He increases the superfluidity suppression gets weaker; it is suggested that ^{4}He atoms are released by the condensation of the Fermi gas in patches of self bound liquid, as such a condensation would reduce the contact between the two isotopic species. It is also noted that the density at which this patches appear is independent on the ^{4}He density.

More recently Sato et al. [38] made heat capacity measurements for ^{3}He adsorbed on graphite preplated with ^{4}He; the density of the ^{3}He atoms is higher than the density of the commensurate 4/7 phase (6.8 nm^{-2}). For densities up to 8.1 nm^{-2} the commensurate phase is stable, and adding more atoms leads to promotion to a new layer. The promoted atoms seem to form a self bound Fermi liquid with a density of 0.1 nm^{-2}. The evidence for the formation of this liquid comes from the observation that the values of the slope of the specific heat as a function of the temperature γ is smaller than the value expected for an ideal Fermi gas spread over all the surface of the sample. Moreover γ increases linearly with the density until the value of the ideal fluid is reached. It was concluded that the reduction of γ is due to the fact that puddles of a self bound liquid form; the formation of puddles leads to a decrease of the area A available to the homogeneous fluid, thus leading to a reduction of γ. Further increases in density lead to a behaviour that is in line with the prediction of the Landau Fermi liquid theory for an homogeneous fluid.

Further measurements were performed by Fukuyama et al. [39]; they measured the heat capacity of different monolayer systems: the first, second and third layers of ^{3}He adsorbed on graphite; the measurement on the first layer were made to determine the effect of the substrate defects on the measured quantities; using a preplating of ^{4}He reduced the substrate effects in the other measurements. Remarkably the formation

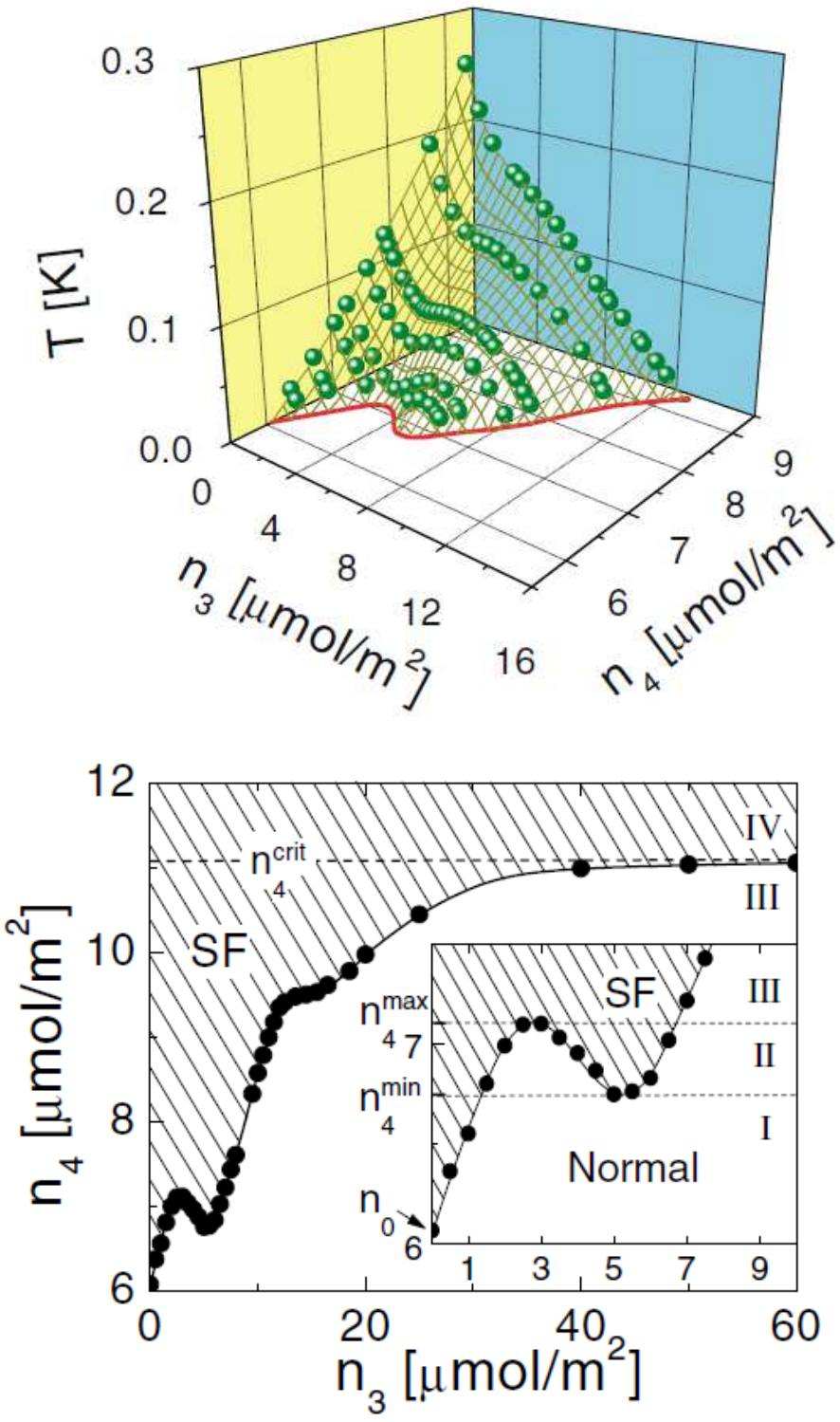

Figure 1.9: Phase diagram for a ^{3}He-^{4}He adsorbed on H_2[44]; on the upper panel the dotted surface separates the superfluid phase (below) and the insulating phase (above); the non monotonic behaviour of the separation curve on the bottom panel (magnified in the inset) may be the signature of condensation of ^{3}He.

of puddles was observed in all the three systems, suggesting that this effect is not due to the substrate, and it is argued that the homogeneous quantum gas phase is not the ground state of ^{3}He even in a strictly two dimensional environment, in contradiction with theoretical computations [13, 22].

In particular in the first monolayer the heat capacity can be written as a sum of three contributions

$$C(T, \rho) = \gamma T - \alpha T^2 + \beta C_{amor}(T); \tag{1.4}$$

the linear an quadratic terms are characteristic of a degenerate two dimensional Fermi liquid with spin fluctuations, while the last term is associated to inhomogeneities of the system for example due to defects. Increasing the density at first the contribution due to inhomogeneities is dominant, and the parameter β increases linearly in ρ until it saturates. Then the value of γ starts to grow linearly, until a kink is reached at $\rho = 1.4$ nm^{-2}, where $\gamma \simeq \gamma_0$, the slope of the heat capacity of an ideal two dimensional Fermi gas (figure 1.10, top). The explanation suggested for this behaviour is the formation of puddles of degenerate Fermi liquid, with an almost constant density $\rho_l = 0.8$ nm^{-2}. In heat capacities of the second and third layers the term due to defects disappears; the ^{4}He preplating has effectively eliminated all the contributions due to the graphite substrate. In the second layer the behaviour of the linear term of the heat capacity is the same as in the first level: at low density γ grows linearly, then there is a kink where the usual behaviour of a homogeneous Fermi liquid begins (figure 1.10, bottom). The density of the puddles in the second layer is about 0.6 nm^{-2}, and the value of γ at the kink is about the same as in the first monolayer. In the third layer the slope of the heat capacity has several kinks. There are two low density regions in which γ grows linearly with ρ, and then two regions in which it grows as in a homogeneous fluid. This behaviour is attributed to structural changes in the second layer, due to compression or to the formation of a commensurate/incommensurate solid (figure 1.11, top). In the third layer the density of the puddles is of the order of 0.9 nm^{-2}.

The differences in the environment of the three layers along with the similar densities of the puddles suggest that the condensation does not depend on substrate effects, and it is argued that it should not even depend on the quasi two dimensionality of the system, in stark contrast with theoretical computations [13, 14, 22]. Finally a low density phase diagram is suggested (figure 1.11, bottom), with a region (in white, with the inset) in which puddles form surrounded by a region in which the system is a homogeneous fluid.

In conclusion we can say that ^{3}He films have a very rich phase diagram, in which the first two layers start as Fermi liquid and then solidify, at first in commensurate and incommensurate phases; increasing the density cause the promotion of helium atoms in new layer, that eventually never solidify. The effect of the substrates becomes significantly less important as the number of layers increases, and after the first two layers the layers become more and more overlapping. By varying the temperature we can observe a strongly correlated degenerate Fermi liquid, that behaves according to Landau Fermi liquid theory, and then a non degenerate quantum gas, whose behaviour is similar to bulk ^{3}He.

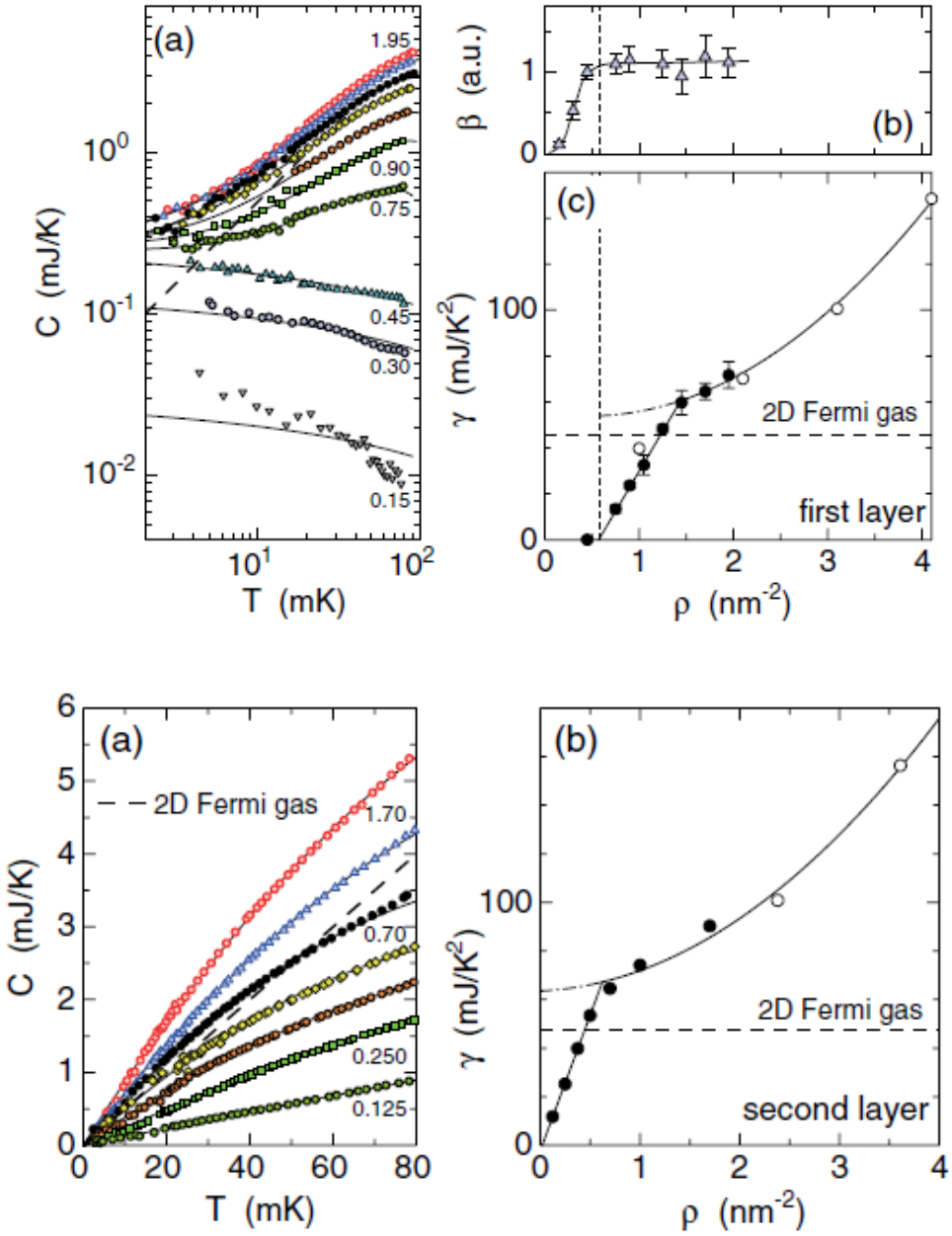

Figure 1.10: Above: Heat capacity of the first layer of ^{3}He adsorbed on Grafoil (a), density dependence of the amorphous term β (b) and density dependence of the slope of the term linear γ (c) in equation 1.4. Densities are expressed in nm^{-2}. Below: Heat capacity of the second layer of ^{3}He adsorbed on Grafoil preplated with ^{4}He (a) and density dependence of the γ (b) [39].

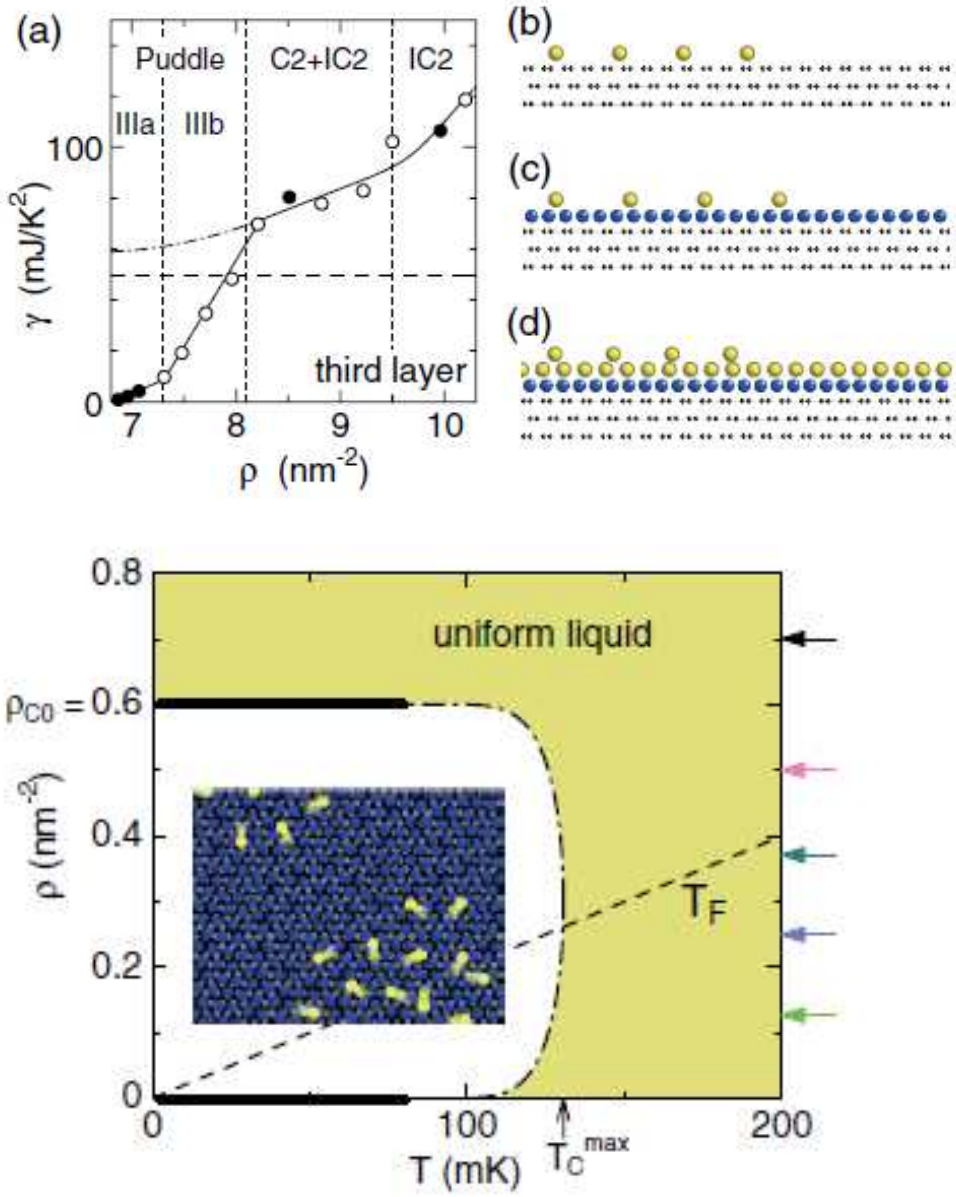

Figure 1.11: Above: γ parameter of the heat capacity of the third layer of ^{3}He adsorbed on Grafoil preplated with ^{4}He (a) and schematic cross sectional views of the first (b), second (b) and third (c) layer puddles of helium; the yellow dots are ^{3}He atoms, the blue ones are the ^{4}He preplating. Only the top three graphite layers are shown. Below: Low density phase diagram of monolayer ^{3}He on graphite. The thick solid lines are the transition lines, the dash-dotted line is estimated. The inset is a schematic top view of the separated liquid puddles [39]. The arrows refer to the densities at which the heat capacity measurements were performed for the second layer.

The low temperature behaviour of two dimensional ^{3}He at very low density isn't clear: while simulations and theoretical works in general do not seem to support the existence of a self bound liquid recent measurements suggest that a such a phase is indeed present. It is very well possible that some element is missing in simulations; we aim to clarify this situation, at least for infinite systems in absence of defects, trying to give a description as realistic as possible of this system.

Chapter 2

Quantum Monte Carlo simulations

Strong interactions and large number of degrees of freedom essentially forbid analytical computations in comndensed matter physics. In order to be able to study physical systems one has to resort on numerical computations. Quantum Monte Carlo simulations are one of these techniques.

Quantum Monte Carlo (QMC) methods are a number of stochastic algorithms that are used to solve a wide array of quantum many body problems. The main feature of all these methods is that they are all stochastic, i.e. are based on random numbers. QMC simulations allow to obtain remarkably accurate result for a large quantity of physical systems of interest, sometimes even allowing to obtain the exact evaluation of physical quantities.

In this chapter we describe the theoretical background of Quantum Monte Carlo simulations for systems in the ground state, focusing on the techniques that we used in this thesis (Variational and Diffusion Monte Carlo) and their application to the study of quantum fluids. We also introduce the trial wave function we used and technical information about the computation of the local energy and finite size corrections.

2.1 Monte Carlo techniques

The term Monte Carlo in general refers to numerical techniques that are used to compute integrals using random numbers. The advantage of these techniques is that they can be used to compute integrals in a large number dimensions, where other numerical techniques (such as quadrature methods) fail. This makes Monte Carlo computations especially useful in the field of statistical and condensed matter physics, as they allow to evaluate statistical averages or expectation values of quantum operators. We now briefly introduce Monte Carlo techniques; for a more in depth discussion a large literature is available (see for example [45]).

To introduce Monte Carlo simulation we start with an example; let us assume that we want to compute the quantity

$$F = \frac{1}{b-a}\int_a^b dx f(x), \tag{2.1}$$

where $f(x)$ is some generic function. Using the integral mean value theorem we have

$$F = \frac{1}{b-a}\int_a^b dx f(x) = \langle f \rangle \tag{2.2}$$

where $\langle f \rangle$ is the average value of the function $f(x)$ over the interval $[a, b]$; we can see here that we have reduced the problem of the computation an integral of a function to the evaluation of the average value in the interval $[a, b]$ of the function itself. This average can be estimated by randomly selecting N points $x_1, \ldots, x_N$ in the interval $[a, b]$ and taking the average value of $f(x_i)$

$$\langle f \rangle \simeq \frac{1}{N}\sum_{i=1}^{N} f(x_i). \tag{2.3}$$

Since we are using random numbers we are introducing a statistical error in the estimate

$$F = \langle f \rangle \pm \varepsilon; \tag{2.4}$$

if we use N independently chosen x_i points the error on the estimate of F is

$$\varepsilon = \sqrt{\frac{\sigma_f^2}{N}} \tag{2.5}$$

where σ_f^2 is the variance

$$\sigma_f^2 = \langle f^2 \rangle - \langle f \rangle^2. \tag{2.6}$$

This simple procedure can be straightforwardly generalized to deal with integration in multiple dimension: the only change that has to be introduced is that in the evaluation of the function $f(\mathbf{x})$ the whole vector $\mathbf{x}_i$, the configuration, has to be randomly generated.

We note that while in 2.2 for simplicity's sake the configurations are uniformly distributed, i.e. the probability of every configuration is equal, Monte Carlo techniques can be used to perform averages with any given probability density

$$\int_a^b dx f(x)\rho(x) = \frac{1}{N}\sum_{i=1}^{N} f(x_i) \tag{2.7}$$

where x_i are distributed according to the normalized distribution $\rho(x)$; this is crucial, as it allows to use Monte Carlo integration using any probability distribution, such as the Boltzmann distribution for a classical system or the modulus square of a wave function in quantum mechanics, to compute thermal averages or quantum mechanical expectation values. All is needed is a way to generate a random walk of configurations that allows to obtain the desired distribution $\rho(x)$.

Such random walk can be generated using a Markov chain

$$x_1 \to x_2 \to x_3 \to \cdots \to x_n \to x_{n+1} \to \ldots \tag{2.8}$$

Using a Markov chain each configuration depends only on the immediately previous configuration. Using suitable moves one can generate a new random configuration starting from a existing one, obtaining a random walk in configuration space. It is possible to define moves so that any given probability distribution ρ can be reached. A way to obtain the required probability distribution is by enforcing the detailed balance condition

$$P(x \to x')\rho(x) = P(x' \to x)\rho(x'), \tag{2.9}$$

where $P(x \to x')$ is the probability to move to the configuration x' starting from x. If the detailed balance condition holds after some equilibration moves the Markov chain will be stationary and the generated configurations will be distributed according to $\rho(x)$.

The problem now is to define moves in such a way that the detailed balance condition holds. While different schemes can be employed, the most widely used is a very simple algorithm: the Metropolis-Hastings algorithm.

According to the Metropolis algorithm [46, 47] starting from an initial configuration we can enforce the detailed balance principle introducing the possibility of rejecting the moves; in particular according to the Metropolis-Hastings algorithm if the probability of accepting a move $\mathbf{x} \to \mathbf{x}'$ is

$$A(x \to x') = \min\left(1, \frac{M(x' \to x)\rho(x')}{M(x \to x')\rho(x)}\right); \tag{2.10}$$

where $M(x \to x')$ is the probability of attempting a a move from to the configuration x' starting from x; with this definition the probability of actually moving from the configuration x to x' is given by the product

$$P(x \to x') = M(x \to x')A(x \to x'), \tag{2.11}$$

that satisfies the detailed balance condition 2.9. Since such detailed balance condition holds if we use this algorithm and the system is ergodic after a number of moves (the equilibration) we eventually generate configurations distributed according to the stationary distribution $\rho(\mathbf{x})$.

Using the generalized Metropolis algorithm the configurations that are generated are not uncorrelated; using 2.5 would lead to an underestimation of the statistical error. In order to give a correct evaluation of the errors we can use data blocking.

Data blocking consists in dividing a simulation of N steps in M blocks with $n = M/N$ steps each. For each block we can define a block average

$$f_m = \frac{1}{n}\sum_{i \in m} f(x_i) \quad \text{for} \quad m = 1, \ldots, M; \tag{2.12}$$

using data blocking the mean value of f is given by

$$\langle f \rangle = \frac{1}{M}\sum_{m} f_m \tag{2.13}$$

while the variance is

$$\sigma_f^2 = \frac{1}{M}\sum_m (f_m - \langle f \rangle)^2. \tag{2.14}$$

If the data blocks are large enough the block averages can be considered independent random variables; if this is the case 2.5 can be used to safely estimate the statistical error using the variance 2.14. To estimate the minimum size for the block averages to be independent it is useful to compute the correlation time of the configurations. In order to estimate the correlation time we can compute the time correlation function for the quantity f

$$C(t) = \langle f(x_0) f(x_t) \rangle - \langle f(x_0) \rangle \langle f(x_t) \rangle; \tag{2.15}$$

at equilibrium the correlation functions exponentially decays as $C(t) \propto e^{-t/\tau}$, where τ is the correlation time. If the block size is much larger than the correlation time τ we can consider our data block independent.

Summing up Monte Carlo computations consist in the evaluation of integrals even in a large number of dimensions using the stochastic evolution of a starting configuration; this evolution is obtained generating new configurations using suitable moves. This procedure is iterated for a large number of times, called Monte Carlo steps. If thethe system is ergodic and the detailed balance principle holds after some equilibration steps the generated configurations will be distributed according to a desired distribution $\rho(\mathbf{x})$. This configurations can be used to compute quantities with an accuracy that increases as the number of steps increase. The statistical error on the estimate can be estimated with the data blocking, and decreases as $1/\sqrt{N}$, N being the number of blocks.

Quantum Monte Carlo techniques are a class of Monte Carlo techniques specifically designed to study quantum systems. Several Quantum Monte Carlo techniques exist, to deal with quantum systems in the ground state and or to evaluate thermal averages. In the rest of this chapter we are going to discuss in detail the methods that we used in our computations, Variational Monte Carlo and Diffusion Monte Carlo. Both methods are designed to study quantum systems in the ground state.

2.2 Variational Monte Carlo

The simplest Quantum Monte Carlo technique is Variational Monte Carlo (VMC) [10]. This technique, is based on the variational principle.

For any trial wave function $\Psi_T(\mathbf{R})$ it is possible to evaluate the energy or any other physical quantity using Monte Carlo simulations. The expectation value of an operator A can be written as

$$\begin{aligned}\langle A \rangle =& \frac{\langle \Psi_T | A | \Psi_T \rangle}{\langle \Psi_T | \Psi_T \rangle} = \frac{\int d\mathbf{R} \Psi_T(\mathbf{R}) A \Psi_T(\mathbf{R})}{\int d\mathbf{R} \Psi_T^2(\mathbf{R})} = \frac{\int d\mathbf{R} \Psi_T^2(\mathbf{R}) \frac{A\Psi_T(\mathbf{R})}{\Psi_T(\mathbf{R})}}{\int d\mathbf{R} \Psi_T^2(\mathbf{R})} = \\ =& \frac{\int d\mathbf{R} \Psi_T^2(\mathbf{R}) A_{LOC}(\mathbf{R})}{\int d\mathbf{R} \Psi_T^2(\mathbf{R})}\end{aligned} \tag{2.16}$$

so that we can estimate the expectation value of an operator as the average value of the local estimator $A_{LOC} = \frac{A\Psi(\mathbf{R})}{\Psi(\mathbf{R})}$ over the probability distribution

$$\rho(\mathbf{R}) = \frac{\Psi_T^2(\mathbf{R})}{\int d\mathbf{R}\Psi_T^2(\mathbf{R})}; \tag{2.17}$$

here we made for simplicity the assumption that the trial wave function is real; in the case it is complex the complex conjugate and the square modulus of the trial wave function have to be used. An especially important estimator is the local energy

$$E_{LOC}(\mathbf{R}) = \frac{H\Psi_T(\mathbf{R})}{\Psi_T(\mathbf{R})} \tag{2.18}$$

whose average over the distribution $\rho(\mathbf{R})$ is the energy of the system.

Integrations like 2.16 can be performed using Monte Carlo simulations. In this case a configuration is given by the the vector $\mathbf{R} = \{\mathbf{r}_i\}$ containing the positions of all the atoms in the system, while a Monte Carlo move consists in moving each atom by a random displacement sampled from a Gaussian distribution with mean value 0 and variance Δr; the probability of accepting a move according to the generalized Metropolis algorithm is

$$A(\mathbf{R} \to \mathbf{R}') = \min\left(1, \frac{|\Psi_T^2(\mathbf{R}')|}{|\Psi_T^2(\mathbf{R})|}\right). \tag{2.19}$$

Using these simulation we can estimate the ground state properties of a quantum system, thanks to the variational principle. The variational principle in quantum mechanics states that the in a quantum state the energy of any trial state is larger or equal to the exact ground state energy

$$\frac{\langle\Psi|H|\Psi\rangle}{\langle\Psi|\Psi\rangle} \geq E_{GS}, \tag{2.20}$$

and states with low energy can be used to approximate the exact ground state. In Variational Monte Carlo we define a trial wave function that depends on a set of variational parameters; we optimize this wave function changing the parameters, minimizing the energy; the optimal wave function will be an approximation of the exact ground state, that can finally be used to compute the physical quantities of interest. The accuracy of this approximation depends on the functional form of the trial wave function $\Psi(\mathbf{R})$, that has to take into account the symmetries of the studied system.

When performing the optimization we can also take advantage of the zero variance principle: the variance of the local energy on an energy eigenstate is strictly zero. It is often useful to take advantage of this minimizing the energy variance along with the energy [75, 48].

The energy minimization can be performed with several numerical techniques. In principle the simplest method is changing by hand the variational parameters in the wave function and then evaluate the energy of the new wave function in a new Monte Carlo simulation, until a minimum is found. This method is of course extremely inefficient, and much more efficient and accurate techniques were designed. We now describe two optimization schemes that we used in our computations, and that allow to optimize a wave function performing just one Variational Monte Carlo simulation.

2.2.1 Correlated sampling

Correlated sampling [49] is a technique that allows to minimize a trial wave function performing only a small number of Variational Monte Carlo simulation. Given a trial wave function depending on the set of variational parameters $\mathbf{a}$ in a variational simulation we can obtain an estimate for the local energy generating M configurations $\mathbf{R}_i$ and computing the quantity

$$\langle E \rangle_{\mathbf{a}} = \frac{1}{M} \sum_{i=1}^{M} \frac{H\Psi(\mathbf{R}_i, \mathbf{a})}{\Psi(\mathbf{R}_i, \mathbf{a})}, \tag{2.21}$$

where we used the notation $\langle \quad \rangle_{\mathbf{a}}$ to emphasize the fact that the average is performed using a wave function with the set of variational parameters $\mathbf{a}$. On the other end if we use a slightly different set of parameters $\mathbf{a}'$ we have

$$\langle E \rangle_{\mathbf{a}'} = \frac{\int d\mathbf{R} \Psi^2(\mathbf{R}, \mathbf{a}') \frac{H\Psi(\mathbf{R}, \mathbf{a}')}{\Psi(\mathbf{R}, \mathbf{a}')}}{\int d\mathbf{R} \Psi^2(\mathbf{R}, \mathbf{a}')}; \tag{2.22}$$

if we multiply and divide by $\Psi^2(\mathbf{R}, \mathbf{a})$ we obtain

$$\langle E \rangle_{\mathbf{a}'} = \frac{\int d\mathbf{R} \Psi^2(\mathbf{R}, \mathbf{a}) \frac{\Psi^2(\mathbf{R}, \mathbf{a}')}{\Psi^2(\mathbf{R}, \mathbf{a})} \frac{H\Psi(\mathbf{R}, \mathbf{a}')}{\Psi(\mathbf{R}, \mathbf{a}')}}{\int d\mathbf{R} \Psi^2(\mathbf{R}, \mathbf{a}) \frac{\Psi^2(\mathbf{R}, \mathbf{a}')}{\Psi^2(\mathbf{R}, \mathbf{a})}} \tag{2.23}$$

if we define the weights $w_i(\mathbf{a}, \mathbf{a}') = \frac{\Psi^2(\mathbf{R}_i, \mathbf{a}')}{\Psi^2(\mathbf{R}_i, \mathbf{a})}$ we can estimate 2.23 as

$$\langle E \rangle_{\mathbf{a}'} = \frac{\sum_{i=1}^{M} w_i(\mathbf{a}, \mathbf{a}') \frac{H\Psi(\mathbf{R}_i, \mathbf{a})}{\Psi(\mathbf{R}_i, \mathbf{a})}}{\sum_i w_i(\mathbf{a}, \mathbf{a}')}; \tag{2.24}$$

this means that we can evaluate the expectation value of the energy for the wave function with the new parameters reweighting the configurations generated with the old wave function. We can thus perform a Variational simulation with a set of parameters saving several configuration, and then using these configurations to evaluate the energy of wave functions with different variational parameters. We can then numerically optimize the parameters without having to perform a large number of Variational Monte Carlo simulations. During this optimization we minimize the quantity

$$Q = E + \alpha\sigma^2 \tag{2.25}$$

where α is a tunable parameter and σ^2 is the variance of the energy, to take into account the zero variance principle. Changing the value of α has the effect of shifting the weights that mean value and variance of the energy have in the minimization.

Correlated sampling gives reliable results only if there are enough uncorrelated configuration and if all the weights have the same order of magnitude; if some weights are significantly larger than the average probably the overlap between $\Psi(\mathbf{R}, \mathbf{a})$ and

$\Psi(\mathbf{R}, \mathbf{a}')$ is too small for the procedure to be successful. If the parameters change too much the effective number of points defined as

$$N_{eff} = \sum_{i=1}^{M} w_i(\mathbf{a}, \mathbf{a}') \tag{2.26}$$

becomes much smaller than the number of the initial configurations and the estimates are not reliable any more: in this case it is necessary to perform a new Variational simulation with the new optimal parameters to generate new configurations.

2.2.2 Linear optimization procedure

Another way to optimize the wave function is the linear optimization procedure [50, 51, 52, 53]. Using this method the variation to existing variational parameters is evaluated diagonalizing a non symmetric estimator of the Hamiltonian matrix in the space spanned by the wave function and its derivative with respect to the variational parameters, taking advantage of the zero variance principle.

We begin the discussion of this procedure with a few definitions. Given a trial wave function $|\Psi(\mathbf{a})\rangle$, where the components of the vector $\mathbf{a}$ are the N variational parameters, we define normalized wave functions as

$$|\overline{\Psi}(\mathbf{a})\rangle = \frac{|\Psi(\mathbf{a})\rangle}{\sqrt{\langle\Psi(\mathbf{a})|\Psi(\mathbf{a})\rangle}}; \tag{2.27}$$

given a starting parameter set $\mathbf{a}_0$ we define

$$|\Psi_0\rangle = |\overline{\Psi}(\mathbf{a}_0)\rangle = |\overline{\Psi}_0\rangle \tag{2.28}$$

then we have the derivative of the wave function with respect to the variational parameters, evaluated in $\{a_i^0\}$

$$|\Psi_i\rangle = \left(\frac{\partial}{\partial a_i}|\Psi(\mathbf{a})\rangle\right)_{\mathbf{a}=\mathbf{a}_0}; \tag{2.29}$$

we also need the matrix S_{ij} with $i, j = 0, \ldots, N$

$$S_{ij} = \langle\Psi_i|\Psi_j\rangle \tag{2.30}$$

i.e. the overlap matrix for the wave function and its derivative with respect to the variational parameters.

Finally we have

$$|\overline{\Psi}_i\rangle = |\Psi_i\rangle - S_{0i}|\Psi_0\rangle, \tag{2.31}$$

the derivatives of the trial wave functions projected on the space orthogonal to $|\Psi\rangle$.

Let us consider an initial parameter set $\mathbf{a}_0$; we can expand a normalized wave function around this set

$$|\overline{\Psi}_{lin}(\mathbf{a})\rangle = |\Psi_0\rangle + \sum_{i=1}^{N} \delta a_i |\overline{\Psi}_i\rangle; \tag{2.32}$$

we want to evaluate E_0, the minimum energy for these wave functions

$$E_0 = \min_{\mathbf{a}} E(\mathbf{a}) = \min_{\mathbf{a}} \frac{\langle \overline{\Psi}_{lin}(\mathbf{a}) | H | \overline{\Psi}_{lin}(\mathbf{a}) \rangle}{\langle \overline{\Psi}_{lin}(\mathbf{a}) | \overline{\Psi}_{lin}(\mathbf{a}) \rangle}. \tag{2.33}$$

This minimization has to be performed with the constraint of the normalization of the wave function, leading to the stationary condition for Lagrange function

$$\nabla_{\mathbf{a}} \left[\langle \overline{\Psi}_{lin}(\mathbf{a}) | H | \overline{\Psi}_{lin}(\mathbf{a}) \rangle - E_0 \langle \overline{\Psi}_{lin}(\mathbf{a}) | \overline{\Psi}_{lin}(\mathbf{a}) \rangle \right] = 0 \tag{2.34}$$

where E_0 acts as a Lagrange multiplier. This equation leads to a generalized eigenvalue problem

$$\overline{\mathbf{H}} \cdot \delta\mathbf{a} = E_0 \overline{S} \cdot \delta\mathbf{a} \tag{2.35}$$

where for $i, j = 0, \ldots, N$

$$\overline{H}_{ij} = \langle \overline{\Psi}_i | H | \overline{\Psi}_j \rangle \tag{2.36}$$

and

$$\overline{S}_{ij} = \langle \overline{\Psi}_i | \overline{\Psi}_j \rangle \tag{2.37}$$

(we note that from 2.28 and 2.31 we have $\overline{S}_{00} = 1$ and $\overline{S}_{i0} = \overline{S}_{0i} = 0$). The linear method then consists in solving the equation 2.35 for the lowest energy eigenvalue: the associated eigenvector will contain the optimal variations to apply to the initial variational parameters.

The overlap and Hamiltonian matrices can be evaluated during a Variational Monte Carlo simulation using suitable estimators. For the overlap matrix by definition we have

$$\overline{S}_{00} = 1 \tag{2.38}$$

and

$$\overline{S}_{i0} = \overline{S}_{0i} = 0; \tag{2.39}$$

moreover

$$\overline{S}_{ij} = \left\langle \frac{\Psi_i(\mathbf{R})}{\Psi(\mathbf{R})} \frac{\Psi_j(\mathbf{R})}{\Psi(\mathbf{R})} \right\rangle - \left\langle \frac{\Psi_i(\mathbf{R})}{\Psi(\mathbf{R})} \right\rangle \left\langle \frac{\Psi_j(\mathbf{R})}{\Psi(\mathbf{R})} \right\rangle. \tag{2.40}$$

Then using the usual definition of local energy

$$E_{LOC}(\mathbf{R}) = \frac{H\Psi(\mathbf{R})}{\Psi(\mathbf{R})} \tag{2.41}$$

and defining

$$E^i_{LOC} = \frac{H\Psi_i(\mathbf{R})}{\Psi_0(\mathbf{R})} - \frac{\Psi_i(\mathbf{R})}{\Psi_0(\mathbf{R})} E_{LOC}(\mathbf{R}) \tag{2.42}$$

for the Hamiltonian matrix we have

$$\overline{H}_{00} = \langle E_{LOC}(\mathbf{R}) \rangle \tag{2.43}$$

then for $i, j > 0$

$$\overline{H}_{i0} = \left\langle \frac{\Psi_i(\mathbf{R})}{\Psi(\mathbf{R})} E_{LOC}(\mathbf{R}) \right\rangle - \left\langle \frac{\Psi_i(\mathbf{R})}{\Psi(\mathbf{R})} \right\rangle \langle E_{LOC}(\mathbf{R}) \rangle \tag{2.44}$$

$$\overline{H}_{0j} = \left\langle \frac{\Psi_j(\mathbf{R})}{\Psi(\mathbf{R})} E_{LOC}(\mathbf{R}) \right\rangle - \left\langle \frac{\Psi_j(\mathbf{R})}{\Psi(\mathbf{R})} \right\rangle \langle E_{LOC}(\mathbf{R}) \rangle - \langle E^j_{LOC}(\mathbf{R}) \rangle \tag{2.45}$$

and finally

$$\begin{aligned} \overline{H}_{ij} = & \left[\left\langle \frac{\Psi_i(\mathbf{R})}{\Psi(\mathbf{R})} \frac{\Psi_j(\mathbf{R})}{\Psi(\mathbf{R})} E_{LOC} \right\rangle - \left\langle \frac{\Psi_i(\mathbf{R})}{\Psi(\mathbf{R})} \right\rangle \left\langle \frac{\Psi_j(\mathbf{R})}{\Psi(\mathbf{R})} E_{LOC} \right\rangle + \right. \\ & - \left\langle \frac{\Psi_j(\mathbf{R})}{\Psi(\mathbf{R})} \right\rangle \left\langle \frac{\Psi_i(\mathbf{R})}{\Psi(\mathbf{R})} E_{LOC} \right\rangle + \left\langle \frac{\Psi_i(\mathbf{R})}{\Psi(\mathbf{R})} \right\rangle \left\langle \frac{\Psi_j(\mathbf{R})}{\Psi(\mathbf{R})} \right\rangle \langle E_{LOC} \rangle \Big] + \\ & + \left[\left\langle \frac{\Psi_i(\mathbf{R})}{\Psi(\mathbf{R})} E^j_{LOC} \right\rangle - \left\langle \frac{\Psi_i(\mathbf{R})}{\Psi(\mathbf{R})} \right\rangle \langle E^j_{LOC}(\mathbf{R}) \rangle \right]. \end{aligned} \tag{2.46}$$

We do not use the Hermiticity of the Hamiltonian to symmetrize $\overline{\mathbf{H}}$ as it was shown by Nightingale and Melik-Alaverdian [51] that using this non symmetric form leads to a stronger reduction of the variance of the local energy. Even if nonsymmetric matrices can have complex eigenvalue in practice if we have a wave function with good overlap with the exact ground state the lowest energy eigenvalues will be real [50]. We also note that the lowest eigenvalue of $\overline{\mathbf{H}}$ is an estimate of the energy of the wave function with the new parameters.

When using this method we introduce a stabilization, i.e. we add a positive constant α to the diagonal element of $\overline{H}_{ii}$ with $i > 0$

$$\overline{H}_{ij} \to \overline{H}_{ij} + \delta_{ij}(1 - \delta_{0i})\alpha; \tag{2.47}$$

in order to use the optimal value of α we perform three minimizations with different αs, we interpolate the lowest eigenvalue of each $\overline{\mathbf{H}}$ with a parabola and then we take the α corresponding to the minimum of the parabola. Proceeding in this manner we have the quickest descent towards the minimum.

When using this procedure we perform a Variational Monte Carlo simulation, and then we diagonalize the Hamiltonian matrix to obtain the optimal parameters; then we repeat this procedure with the new trial wave function; in a few iterations we reach a stable solution which is a good approximation for the exact ground state. We note that even if the computation of all the matrix elements can be quite demanding when we have a lot of variational parameters this procedure can be more efficient than correlated sampling.

2.3 Projector Monte Carlo

Variational Monte Carlo is the simplest Quantum Monte Carlo technique, and it allows to obtain results that are approximate for virtually any non trivial system. On the other hand during the years new more complex methods were devised, methods that in principle allow exact estimates for the ground state properties of quantum systems.

These are the projection techniques, based on the imaginary time evolution of a trial wave function. The core idea of projection techniques is that we can rewrite the Schrödinger equation in imaginary time using the transformation $\tau = \frac{it}{\hbar}$

$$i\frac{d\Psi}{dt}(\mathbf{R},t) = (H - E_T)\Psi(\mathbf{R},t) \quad \rightarrow \quad -\frac{d\Psi}{d\tau}(\mathbf{R},\tau) = (H - E_T)\Psi(\mathbf{R},\tau) \tag{2.48}$$

where we set $\lambda = \frac{\hbar^2}{2m}$ and introduced the energy shift E_T for reason that will be explained below. With the initial condition $\Psi(\mathbf{R},\tau=0) = \Psi_T(\mathbf{R})$ the general solution for equation 2.48 is of the form

$$\Psi(\mathbf{R},\tau) = e^{-(H-E_T)\tau}\Psi_T(\mathbf{R}); \tag{2.49}$$

this solution can then be decomposed on an energy eigenstates basis $\{\Phi_i\}$ as

$$\Psi(\mathbf{R},\tau) = \sum_i c_i e^{-(E_i-E_T)\tau}\Phi_i(\mathbf{R}); \tag{2.50}$$

where $H|\Phi_i\rangle = E_i|\Phi_i\rangle$ and $c_i = \langle\Phi_i|\Psi_0\rangle$. We can see that all the energy eigenstates components exponentially decay as the imaginary time increases. We can adjust the energy shift E_T to make the exponential term $\exp(-(E_0 - E_T)\tau)$ constant, so that for long imaginary times only the ground state contribution survives.

$$\Psi(\mathbf{R},\tau) = \sum_i c_i e^{-(E_i-E_T)\tau}\Phi_i(\mathbf{R}) \simeq c_0 e^{-(E_0-E_T)\tau}\Phi_0(\mathbf{R}). \tag{2.51}$$

We can thus define a trial wave function, evolve it for a long enough imaginary time and then we obtain the exact ground state, that can be sampled to compute exact ground state quantities. One just has to be careful not to choose a trial wave function that is orthogonal to the exact ground state. The difference between the several projection techniques (Green's function Monte Carlo [54, 55], Path Integral Ground State Monte Carlo [56, 57, 58] and Diffusion Monte Carlo [11, 60, 61, 63]) is in how the imaginary time evolution is treated.

2.4 Diffusion Monte Carlo

Diffusion Monte Carlo (DMC) [59, 11, 60, 61, 63] is based on the observation that equation 2.48 is essentially a diffusion equation with a branching term. Equation 2.48 can be written as

$$\frac{\partial\Psi(\mathbf{R},\tau)}{\partial\tau} = \lambda\Delta\Psi(\mathbf{R},\tau) - (V(\mathbf{R}) - E_T)\Psi(\mathbf{R},\tau). \tag{2.52}$$

If we neglect the potential and the energy shift in 2.52 we obtain

$$\frac{\partial\Psi(\mathbf{R},\tau)}{\partial\tau} = \lambda\Delta\Psi(\mathbf{R},\tau) \tag{2.53}$$

which is a diffusion equation, whose Green's function for this equation is

$$G(\mathbf{R}', \mathbf{R}, \delta\tau) = \frac{1}{(4\pi\lambda\tau)^{dN/2}} e^{-\frac{(\mathbf{R}'-\mathbf{R})^2}{4\lambda\delta\tau}} \tag{2.54}$$

We can see that there is a correspondence between the wave function $\Psi(\mathbf{R}, \tau)$ and a population of Brownian particles; this means that we can represent the evolution of the wave function $\Psi(\mathbf{R}, \tau)$ with the a population of random walkers that diffuse according to the propagator 2.54. Now let us consider the full Hamiltonian. In general we do not know the Green's function for a generic Hamiltonian, and we have to introduce some approximation. We can for example use the Trotter-Suzuki formula to factorize the Green's function

$$G(\mathbf{R}', \mathbf{R}, \delta\tau) = \langle \mathbf{R}' | e^{H\delta\tau} | \mathbf{R} \rangle \simeq \frac{1}{(4\pi\lambda\tau)^{dN/2}} e^{-\frac{(\mathbf{R}'-\mathbf{R})^2}{4\lambda\delta\tau}} e^{-\delta\tau(V(\mathbf{R})-E_T)}; \tag{2.55}$$

the factor $\exp(-\delta\tau(V(\mathbf{R})-E_T))$ introduces a time dependent renormalization (reweighting) for the Green's function. This reweighting can be included in the diffusive process by assigning a statistical weight to each random walker or using a branching algorithm, that allows to duplicate or kill the random walkers depending on the reweighting factor. The latter approach is more efficient [59]. The propagator 2.55 is accurate only for short time steps; in order to sample the wave functions we iteratively apply the short time propagator, each diffusing the random walkers and applying the branching. This realization of the Diffusion Monte Carlo has a problem: if we deal with an unbounded potential, such as the Lennard-Jones potential, the branching term in the propagator varies wildly at each iteration, and so do the population of the walkers. This means that the estimates suffer from an extremely high variance. In order to avoid this problem importance sampling is introduced [61].

Importance sampling consists in defining a guiding function ψ_G and and using the random walk to sample not the wave function $\Psi(\mathbf{R}, \tau)$, but instead the distribution $f(\mathbf{R}, \tau) = \psi_G(\mathbf{R})\Psi(\mathbf{R}, \tau)$; the guiding function should be a reasonable approximation of the ground state. If Ψ satisfies the Schrödinger equation the distribution f can be shown to be a solution of the equation

$$-\frac{\partial f(\mathbf{R}, \tau)}{\partial \tau} = -\lambda\Delta f(\mathbf{R}, \tau) + \nabla \cdot (\mathbf{F}(\mathbf{R}) f(\mathbf{R}, \tau)) + (E_{LOC}(\mathbf{R}) - E_T) f(\mathbf{R}, \tau) \tag{2.56}$$

where the velocity $\mathbf{F}(\mathbf{R})$ is defined as

$$\mathbf{F}(\mathbf{R}) = \frac{\nabla\Psi_G(\mathbf{R})}{\Psi_G(\mathbf{R})} \tag{2.57}$$

end $E_{LOC}(\mathbf{R})$ is the local energy defined as in 2.18, using the guiding function $\Psi_G(\mathbf{R})$. In practice the guiding function is an optimal wave function obtained with a Variational Monte Carlo procedure, and when dealing with Diffusion Monte Carlo we will use the terms trial wave function and guiding function interchangeably.

The Green's function for equation 2.56 for small imaginary times is

$$G(\mathbf{R}', \mathbf{R}, \delta\tau) = \\ = \frac{1}{(4\pi\lambda\delta\tau)^N} \int d\mathbf{R}'' e^{-\frac{(\mathbf{R}'-\mathbf{R}'')^2}{4\lambda\delta\tau}} \delta(\mathbf{R}'' - \mathbf{R} - \mathbf{F}(\mathbf{R})\delta\tau) e^{-\delta\tau(V(\mathbf{R})-E_T)}. \tag{2.58}$$

In this propagator along with the diffusion and branching terms there is a drifting term: when evolving the walkers now we first apply the drift, moving the atoms along the gradient of the guiding function, and only then we diffuse them and apply the branching. This allows us to include in the sampling the knowledge that we have on the approximate variational wave function that we had from our Variational Monte Carlo runs, and this vastly improves the efficiency of the algorithm.

In the DMC algorithm there are two sources of bias: a time step error and a population control bias. The time step error is due to the factorization of the propagator 2.55; time step error becomes more important when the trial wave function has nodes. Near nodes the local energy and the drift velocity both diverge, and the factorized Green's function is a poor approximation for the exact propagator; this leads to the presence of a finite number of walkers in the proximity of the nodes. This problem can be reduced introducing a generalized Metropolis check [11]; each time a move is attempted is accepted with a probability

$$P(\mathbf{R} \to \mathbf{R}') = \text{Min}\left\{1, \frac{|\Psi_G(\mathbf{R}')|^2 G(\mathbf{R}, \mathbf{R}', \delta\tau)}{|\Psi_G(\mathbf{R})|^2 G(\mathbf{R}', \mathbf{R}, \delta\tau)}\right\}. \tag{2.59}$$

The population control bias [62] on the other hand is due to the fact that during a DMC simulation we have to adjust the energy shift E_T to reduce the fluctuations of the walker population. This introduces a bias in the estimates.

As a final remark we observe that when using importance sampling we are averaging the mixed estimators

$$A_{Mix} = \langle \Psi_G | A | \phi_0 \rangle; \tag{2.60}$$

the average values that we obtain are the exact estimates only if A commutes with the Hamiltonian, otherwise we have a bias in the estimate. This bias can be dealt with using the variational estimates to obtain the extrapolated estimates

$$A_{Ext} = 2\langle \Psi_G | A | \phi_0 \rangle - \langle \Psi_G | A | \Psi_G \rangle \tag{2.61}$$

2.5 The fixed node approximation

While in principle Diffusion Monte Carlo (and projector methods in general) allows to sample the exact ground state of quantum systems, in practice the sampling is possible only for Bose systems. This is due to the fact that Bose system have wave functions that are symmetric under particle exchange, and so they have nodeless ground states. If the wave function has nodes, as in the case of Fermi systems, or even excited states of Bose systems, the statistical weights of the walkers are not positive defined: whenever a walker crosses a node of the guiding function in fact the weight changes sign; this means

that when accumulating averages we are summing terms with positive and negative statistical weights, and this results in large variances, that in turn leads to the estimates being drown in the statistical noise. This is the sign problem [64].

We note that Variational Monte Carlo does not have sign problem, as in this case we are sampling the square modulus of the wave functions, that is always positive. In Diffusion Monte Carlo (and projector methods in general) the sign problem is present: even if in the limit $\delta\tau \to 0$ the number of walkers crossing the nodal surface vanishes (the drift term tends to drive the walkers away from the nodes, with a velocity that diverges at the nodes, and small time steps severely limit the possibility that the diffusion leads to a crossing), for any finite $\delta\tau$ some crossing is unavoidable. Thus to avoid the sign problem we have to restrict our random walk: we have to introduce the fixed node approximation (FN)[65]. Other techniques were implemented to deal with the sign problem, but these techniques usually have huge computational cost and can thus be applied only to the study of very small systems [19, 20, 66, 67, 68, 69]; the fixed node technique is thus the most used technique to deal with the sign problem in Quantum Monte Carlo simulations of a wide range of systems, from electron in atoms and molecules [12, 63, 65, 49, 70] to ^{3}He [13, 72, 73, 74, 75, 76] to the electron gas [18, 77, 78, 79].

This restriction can be implemented simply by killing all the walkers that cross a nodal surface of $\Psi_G(\mathbf{R})$ and the duplicating the surviving ones according to their weights, to preserve the total number of walkers, but such a procedure leads to a large time step error. A more efficient way to deal with the nodes is to include the restriction in the Metropolis check 2.59: if during a move a walker crosses a nodal surface the move will be always rejected [11].

Introducing the fixed node approximation we are not performing exact ground state estimates: instead our estimates are again variational; their accuracy increase as the nodal surface of the guiding function becomes closer to the nodal surface of the exact ground state. This makes especially important to optimize the nodal surfaces when dealing with Fermi systems. We note that using a guiding function with the same nodal surface of the exact ground state means that f is a well defined probability distribution, there is no sign problem and the estimates are exact; using such a guiding function however is in practice impossible, as designing such a function requires the knowledge of the exact nodal surface, which is an extremely complicated $dN - 1$ dimensional hypersurface (where d is the dimensionality of the system and N the number of atoms).

2.6 Trial wave functions

When using Variational and Diffusion Monte Carlo we have to use a trial (guiding) wave function. Designing good wave functions is an extremely important task if we want to obtain accurate results with the simulations. Typically good wave functions should take into account physical features of the system under study, such as symmetries of the Hamiltonian, the presence of external fields or interparticle correlations. In this section we describe the trial wave function that we used in our simulations.

A typical wave function for a quantum fluid has the form [18]

$$\Psi(\mathbf{R}) = J(\mathbf{R}) \cdot \chi(\mathbf{R}) = e^{-U(\mathbf{R})} \cdot \chi(\mathbf{R}). \tag{2.62}$$

The first term in this 2.62 - the Jastrow term - describes interparticle correlations. It has the form of an exponential of some suitable pseudopotential; this pseudopotential has at least a two body term and usually a three body term

$$U(\mathbf{R}) = U_2(\mathbf{R}) + U_3(\mathbf{R}). \tag{2.63}$$

The two body term is given by the sum of an effective two body interaction over all the particle pairs

$$U_2(\mathbf{R}) = \sum_{i<j} u(r_{ij}) \tag{2.64}$$

while the three body term has the form

$$U_3(\mathbf{R}) = \sum_i \mathbf{G}_i(\mathbf{R}) \cdot \mathbf{G}_i(\mathbf{R}) \quad \text{where} \quad \mathbf{G}_i(\mathbf{R}) = \sum_j (\mathbf{r}_i - \mathbf{r}_j)\xi(r_{ij}). \tag{2.65}$$

The pseudopotentials $u(r)$ and $\xi(r)$ here are functions that have to be optimized via the Variational Monte Carlo procedure.

The Jastrow term so defined is purely symmetric; to take into account particle statistic we introduce the second term in 2.62. When dealing with a Bose system $\chi(\mathbf{R})$ has to be symmetric, and is typically just a constant, while if we are dealing with a Fermi system it must be antisymmetric. In order to guarantee antisymmetry $\chi(\mathbf{R})$ is defined as a Slater determinant, or a product of Slater determinants if we have more fermionic species, such as population of atom with spin up and down

$$\chi(\mathbf{R}) = \begin{cases} 1 & \text{(Bose)} \\ \det_\uparrow(\phi_i(\mathbf{r}_j)) \det_\downarrow(\phi_i(\mathbf{r}_j)) & \text{(Fermi)} \end{cases}. \tag{2.66}$$

The states $\{\phi_i\}$ in the Slater determinants in 2.66 depend on the physical system in analysis; for example if we are dealing with electrons in an atom or a molecule they can be (linear combinations of) atomic orbitals, while for bulk liquids they usually are plane waves.

Using simple plane waves in simulations of Fermi liquids at high density gives inaccurate results; to improve the wave functions backflow transformations are used [18, 73]. Introducing backflow means that instead of using the bare atomic coordinates in $\chi(\mathbf{R})$ another set of auxiliary coordinates is used. These backflow coordinates $\mathbf{x}_i$ are defined as

$$\mathbf{x}_i = \mathbf{r}_i + \sum_{j \neq i} (\mathbf{r}_i - \mathbf{r}_j)\eta(r_{ij}) \tag{2.67}$$

where $\eta(r)$ is a suitable pseudopotential. Backflow transformations modify the atomic coordinates used in the backflow, introducing correlations between particles, as each atom is effectively pulled or pushed by the others via the pseudopotential $\eta(r)$. We are

going to also refer to backflow coordinates as the coordinates of (auxiliary) backflow particles . Optimizing the pseudopotential in the backflow transformations is especially important when using the fixed node approximation, as the nodal surface of the trial wave function is fully determined by the backflow coordinates. More detailed information about backflow transformation will be provided in chapter 4.

All the pseudopotential u, ξ, η we used in our computations have the form

$$f(r) = \begin{cases} (r_C - r)^3 \left[\sum_{n=1}^{5} a_n r^{n-1} + a_6/r^{a_7}\right] & \text{if } r < r_C \\ 0 & \text{if } r \geq r_C \end{cases}. \tag{2.68}$$

For the two-body pseudopotential we chose a cutoff value r_C close to half the side of the simulation box; for the backflow and three-body pseudopotentials we dropped the McMillan term ($a_6 = 0$) and we used a shorter cutoff as these terms have a short range [72].

2.7 Local energy

In order to compute the energy for a system we have to compute the average value of the local energy 2.18

$$E_{LOC}(\mathbf{R}) = \frac{H\Psi(\mathbf{R})}{\Psi(\mathbf{R})} = -\lambda \frac{\Delta\Psi(\mathbf{R})}{\Psi(\mathbf{R})} + V(\mathbf{R}). \tag{2.69}$$

The potential energy is evaluated by simply computing the value of the potential $V(\mathbf{R})$ for each configuration of the simulation and then performing the average; we note that in the evaluation of the potential energy we don't even need to know the trial wave function, but just the configuration.

The kinetic energy is more involved, and requires the computation of derivatives of the trial wave function. We note that since we are dealing with ratios between derivatives of the wave functions and the wave functions themselves we can work with derivatives of the logarithm of the wave functions

$$\frac{\Delta\Psi(\mathbf{R})}{\Psi(\mathbf{R})} = \Delta \log \Psi(\mathbf{R}) + \left[\nabla \log \Psi(\mathbf{R})\right]^2; \tag{2.70}$$

this suggests that we compute in our simulations the logarithms of the trial wave functions instead of the wave functions themselves; this also mean that we have to just sum the logarithm of the factors composing the wave function, simplifying and speeding up the computations. It is natural then to write the Jastrow part of the wave function in exponential form as in 2.62 and to work directly with the pseudopotentials. For the computations of the derivatives we need to use the relations

$$\begin{aligned} \frac{\partial r_j^\beta}{\partial r_i^\alpha} &= \delta_{ij}^{\alpha\beta} \\ \frac{\partial r_{jk}}{\partial r_i^\alpha} &= \frac{r_{jk}^\alpha}{r_{jk}} \left(\delta_{ij} - \delta_{ik}\right), \end{aligned} \tag{2.71}$$

where the indexes i, j, k label the atoms and α and β refer to Cartesian components,and applying the chain rule.

Computing the kinetic energy of the two body potential in the wave function is straightforward, while the computation of the gradient and the Laplacian of three body term and of the Slater determinant in presence of backflow are more involved. We will follow [77] in the following discussion. We start considering the Slater determinant. To compute the derivatives of the backflow coordinates 2.67 we define the matrices

$$\begin{aligned} A_{ij}^{\alpha\beta} &= \frac{\partial x_j^\beta}{\partial r_i^\alpha} \\ B_{ij}^\beta &= \sum_\alpha \frac{\partial^2 x_j^\beta}{\partial r_i^\alpha \partial r_i^\alpha} = \sum_\alpha \frac{\partial A_{ij}^{\alpha\beta}}{\partial r_i^\alpha} \end{aligned} \tag{2.72}$$

for the matrix A we have

$$A_{ij}^{\alpha\beta} = \delta_{ij}^{\alpha\beta} + \sum_{k\neq j} (\delta_{ij} - \delta_{ik}) \left[\delta^{\alpha\beta}\eta(r_{jk}) + r_{jk}^\alpha r_{jk}^\beta \frac{\eta'(r_{jk})}{r_{jk}} \right] \tag{2.73}$$

while for B we have

$$\begin{aligned} B_{ij}^\beta = \sum_\alpha \sum_{k\neq j} (\delta_{ij} - \delta_{ik})^2 \Bigg[& \delta^{\alpha\beta} \frac{\eta'(r_{jk})}{r_{jk}} r_{jk}^\alpha + r_{jk}^\beta \frac{\eta'(r_{jk})}{r_{jk}} + \delta^{\alpha\beta} r_{jk}^\alpha \frac{\eta'(r_{jk})}{r_{jk}} + \\ & - \left(r_{jk}^\alpha\right)^2 r_{jk}^\beta \frac{\eta'(r_{jk})}{r_{jk}^3} + \left(r_{jk}^\alpha\right)^2 r_{jk}^\beta \frac{\eta''(r_{jk})}{r_{jk}^2} \Bigg]. \end{aligned} \tag{2.74}$$

Since

$$\sum_\alpha \left(r_{jk}^\alpha\right)^2 = r_{jk}^2 \tag{2.75}$$

if d is the dimensionality of the system we finally have

$$B_{ij}^\beta = \sum_{k\neq j} (\delta_{ij} + \delta_{ik}) \left[(d+1) \frac{\eta'(r_{jk})}{r_{jk}} + \eta''(r_{jk}) \right] r_{jk}^\beta. \tag{2.76}$$

Now in order to compute the derivatives of the Slater determinant we need firstly to evaluate the matrices

$$\begin{aligned} \phi_{ki} &= e^{i(\mathbf{k}\cdot\mathbf{x}_i)} \\ \phi_{ki}^\alpha &= \frac{\partial \phi_{ik}}{\partial x_i^\alpha} \\ \phi_{ki}^{\alpha\beta} &= \frac{\partial^2 \phi_{ik}}{\partial x_i^\alpha \partial x_i^\beta}; \end{aligned} \tag{2.77}$$

then we need to compute V_{jk}, the inverse of ϕ_{ki}, since from linear algebra we have

$$\frac{\partial \log(\det(\phi))}{\partial \phi_{ki}} = \frac{1}{\det(\phi)} \frac{\partial \det(\phi)}{\partial \phi_{ki}} = V_{ik} \quad \text{with} \quad \sum_k V_{jk}\phi_{ki} = \delta_{ij}; \tag{2.78}$$

then using the chain rule we obtain the first derivatives of the logarithm of the Slater determinant

$$\nabla_i^\alpha \log(\det(\phi)) = \sum_\beta \sum_{jk} V_{jk}\phi_{kj}^\beta A_{ij}^{\alpha\beta} = \sum_\beta \sum_j F_{jj}^\beta A_{ij}^{\alpha\beta} \tag{2.79}$$

where we defined

$$F_{ij}^\beta = \sum_k V_{ik}\phi_{kj}^\beta. \tag{2.80}$$

For the Laplace operator instead we use the property

$$\frac{1}{\det(\phi)}\frac{\partial^2 \det(\phi)}{\partial\phi_{kn}\partial\phi_{jm}} = V_{nk}V_{mj} - V_{mk}V_{nj} \tag{2.81}$$

so that in the end we have

$$\Delta \log(\det(\phi)) = \sum_{\alpha ij} B_{ij}^\alpha F_{jj}^\alpha - \sum_{\alpha\beta\gamma}\sum_{ijk} A_{ij}^{\alpha\beta}A_{ik}^{\alpha\gamma} \cdot \left(F_{kj}^\beta F_{jk}^\gamma - \delta_{jk}\sum_m V_{jm}\phi_{mj}^{\beta\gamma} \right). \tag{2.82}$$

The computational cost of evaluating these terms scales as N^3 [77]. For the three body pseudopotential we observe that the function $\mathbf{G}_i(\mathbf{R})$ in 2.65 are basically the same as the backflow transformations 2.67. We can thus use the analogue of the matrices $A_{ij}^{\alpha\beta}$ and B_{ij}^β and the rule of the derivative of a product to obtain the gradient and Laplacian of the three body term. Once we have computed these derivatives we can simply add the contributions of all particles to the kinetic energy of the Jastrow part.

2.8 Finite size corrections

In simulations it is of course impossible to simulate a system in the thermodynamic limit. In numerical computation we actually deal with a finite system, i.e. we consider a finite number of atoms in a simulation box with periodic boundary conditions. Simulating a finite system introduces some bias in the energy estimates.

In periodic boundary conditions we need that the interaction potential between particles is zero at distances longer than $L/2$, where L is the side of the simulation box, to enforce the minimum image convention (one atom must interact with at most one image of the other atoms). In order to obtain such a potential we use an effective potential obtained truncating the potential at $L/2$ and then subtracting $V(L/2)$.

In order to recover the actual potential energy we must reverse this truncation and this shift, adding two corrections, an "outer" correction V_{out} and an "inner" correction V_{in}.The correction V_{out} is introduced to reverse the truncation of the potential; it is given by

$$V_{out} = \int_{L/2}^{+\infty} dr V(r)g(r) \tag{2.83}$$

where $g(r)$ is the pair correlation function; in a fluid system $g(r) \to 1$ for large r, and when computing this correction we can just approximate it to 1

$$V_{out} \simeq \int_{L/2}^{+\infty} dr V(r). \tag{2.84}$$

V_{in} instead is a correction introduced to deal with the energy shift; this correction is given by

$$V_{in} = V(L/2) \int_0^{L/2} dr g(r); \tag{2.85}$$

this term can be easily computed during the simulation, adding a constant term $V(L/2)$ for each particle pair each time the energy is computed or it can be computed after the simulation is performed, integrating the pair correlation function $g(r)$.

When dealing with Fermi system we have another size correction to add, this time involving the kinetic energy; having a finite simulation box means in fact that we have a discrete set of momenta inside the Fermi surface, inducing a deformation of the isotropic Fermi sphere that is present at the thermodynamic limit. In order to correct this deviation we have to analytically compute the energy of an ideal Fermi system in the thermodynamic limit at a given density and the energy of a non interacting finite system at the same density; the difference between these two energies is the correction to be added to the kinetic energy.

Chapter 3

^{3}He on substrates

The low density behaviour of two dimensional ^{3}He is not clear. The general consensus is that ^{3}He in the ground state is a homogeneous liquid, but some experimental data offer a different picture . Recent experiments on helium atoms adsorbed adsorbed on graphite substrate in fact suggest that ^{3}He at very low density can form puddles of a self bound liquid [38, 39]. This is in stark contrast with available theoretical studies: most numerical computations exclude the presence of a liquid phase for two dimensional ^{3}He [22, 13]. Numerical computations however tend to focus on ideal, strictly two dimensional systems. This means that effects due to the motion of helium atoms in the z direction or to the presence of a corrugated substrate are completely ignored. These effects may very well contribute to the stabilization of a liquid phase. The zero point motion in the transverse direction in fact has the effect of effectively smoothing the hard core repulsion of the helium-helium interaction of the strictly two dimensional case. Moreover corrugation leads to an effective increase of the band mass of the helium atoms [28].

We study the behaviour of quasi two dimensional ^{3}He at very low density via Quantum Monte Carlo simulations. We simulate a strictly two dimensional system, focusing on the low density range that is usually not much considered in simulations, and then systems adsorbed on substrates. We use weakly interacting alkali substrates to understand the stabilizing effect of a large transverse zero point motion; to understand the experimental results by Fukuyama we simulate a ^{3}He adsorbed on graphite, both in the first and in the second layer.

3.1 Two dimensional helium

In the simulations of the strictly two dimensional system we studied three different species of helium, the bosonic ^{4}He, fermionic ^{3}He and a hypothetical mass 3 boson. We decided to simulate the mass 3 boson in order to study the different behaviour the helium isotopes is due to their different mass of if the different statistic has some important effect. We reproduce results already known in literature, and we add new data for very low densities.

The Hamiltonian of our system is

$$H = \frac{\hbar^2}{2m} \sum_i p_i^2 + \sum_{i \neq j} V(r_{ij}). \tag{3.1}$$

We used the SAPT2 pair potential [31] to model the helium-helium interaction $V(r)$. This is potential, obtained with quantum chemistry computation, gives an extremely accurate description of the energy of a helium dimer.

We also included an energy correction due to a three body potential [80]; the three body potential is less well known than the two body one, but at the low densities we are studying they can be approximated with good accuracy by an Axilrod-Teller potential [81]; the three body potential was not explicitly included in the propagator in the Diffusion Monte Carlo simulations, but was included as a correction to the total potential energy perturbatively, after the simulations were done.

As trial wave functions we used Jastrow wave functions for the bosons, with two and three body correlations, and a Jastrow-Sater wave function for the fermions, using in the determinants plane waves with backflow transformations, as discussed in section 2.6.

We optimized the wave functions with a Variational Monte Carlo procedure, using the correlated sampling technique; the optimal wave functions were then used in Diffusion Monte Carlo simulation, using the Fixed Node approximation for the Fermi system. We simulated a system with $N = 18$ atoms in a two dimensional simulation box with periodic boundary conditions. The Diffusion Monte Carlo simulation were performed with an imaginary time step $\delta\tau = 10^{-3}$ K^{-1} using 6400 walkers. We verified that using these parameter the time step error and the population control bias have negligible effects on the equation of state.

Performing these computations we carefully studied possible sources of bias due to the finite size of our system that can affect our results, especially when dealing with the Fermi system; in this case we have to include corrections the potential energy, due to the truncation of the interaction potential, and also the correction to the kinetic energy, due to the discretization of the Fermi sphere. We show in figure 3.1 the finite size corrections for ^{3}He as a function of the system size. If we take into account only corrections to the potential energy the magnitude of the correction wildly oscillates when the system size changes. Including the correction to the kinetic energy leads to a much more stable behaviour. We conclude that it is always important to include the kinetic term in the energy corrections for Fermi systems, otherwise finite size effects can be a source of bias in the determination of an equation of state, especially if the small energy fluctuations can severely affect the predicted physical behaviour. We fitted the corrections to energy for a $N = 18$ system as a function of the density, with a function of the form $f(\rho) = a\,\rho^b$.

Another source of bias for fermions comes from the error of the nodal surface of the trial wave function; we estimated this error comparing the fixed node energy obtained with our wave function with an exact result obtained with the Transient Estimate technique [20]; this correction was computed for a system at freezing ($\rho = 0.060$ Å^{-2}), and we assumed that the nodal correction has a quadratic dependence on the density.

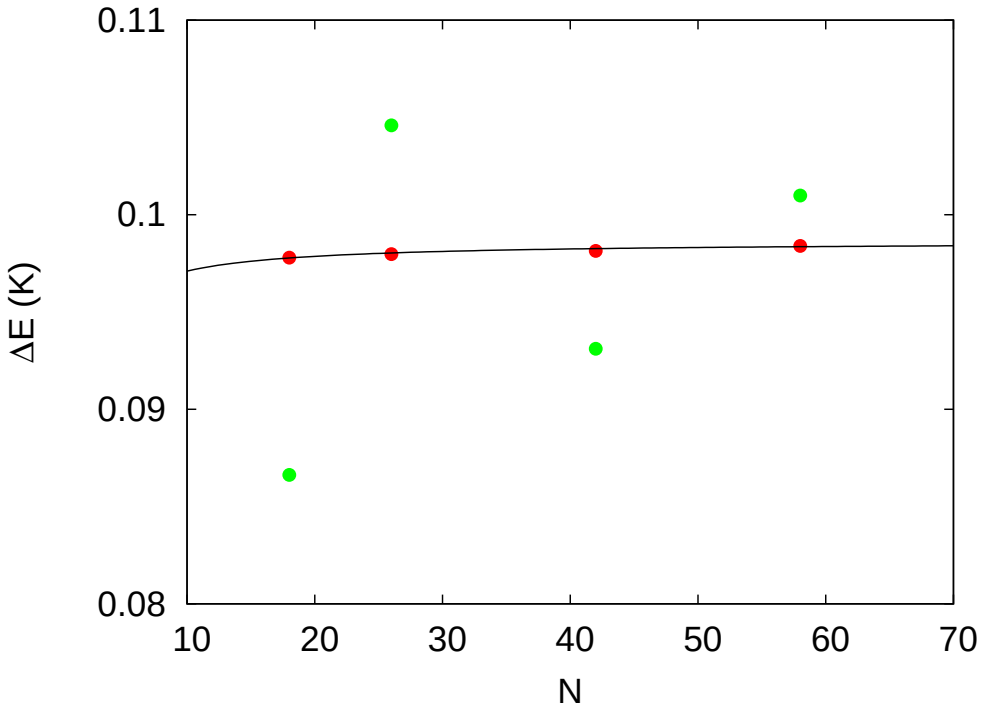

Figure 3.1: Finite size correction for a two dimensional system ^{3}He at $\rho = 0.009$ Å^{-2} as a function of the number of atoms in the system; the green data set takes into account only corrections due to the truncation of the potential, in the red set the correction of the kinetic energy is included; the black line is a fit of the total finite size effect.

This assumption was made observing the energy difference between the fixed node estimates and the exact Transient Estimate date in [20].

We show the DMC equations of state of the different helium species figure 3.2. We can clearly see the differences between the three systems here. The energy of ^{4}He has a well defined minimum, and the energy does not vanish for $\rho \to 0$, as it should do for a homogeneous fluid, but instead it goes to a constant, which is the energy per particle of a two dimensional puddle of $N = 18$ atoms [14]; the formation of a cluster is also evident from the shape of the pair correlation function $g(r)$ (figure 3.3, left). The formation of two dimensional ^{4}He clusters was already predicted [14], but we note that in our computations, even in the variational estimates, we can observe the formations of puddles even if we work in periodic boundary conditions and without imposing any form factor to our trial wave function.

A minimum in the energy is seen also in the equation of states of the mass 3 boson. In this case the formation of puddles is not clear; previous works [14] predicted a very weakly self bound liquid for bosonic ^{3}He, but it is not clear if 18 atoms are enough to form a puddle. We can see some hints of the formation of a puddle in the $g(r)$ (figure 3.3, right), where after the maximum a slow decay can be observed; the situation could be clarified simulating two dimensional clusters in larger simulation boxes or using

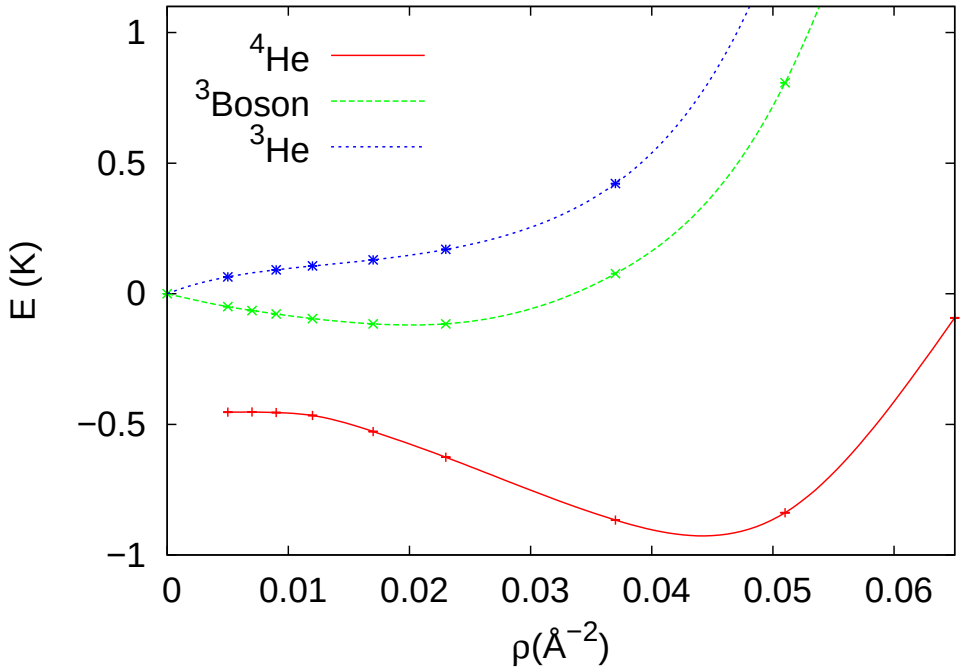

Figure 3.2: Equation of state for two dimensional helium; we plot the energy per atom for ^{4}He, a hypothetical mass 3 boson and ^{3}He. Error bars are smaller than the size of the symbols.

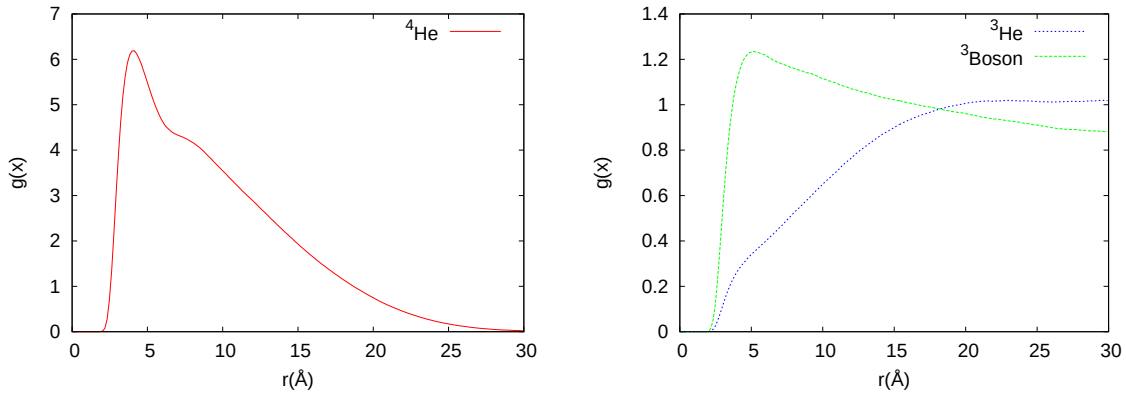

Figure 3.3: Radial correlation functions for two dimensional helium; we plot results for ^{4}He (left) and for a hypothetical mass 3 boson and ^{3}He (right). Error bars are smaller than the size of the symbols.

open boundary conditions.

The situation is very different for fermionic ^{3}He: here the energy grows monotonically, and we can exclude the formations of a liquid; the $g(r)$ in this case has no peak, reflecting only the hard core repulsion. The pair correlation function that we compute for low density ^{3}He bears a strong resemblance to the wave functions used to describe a weakly bound ^{3}He dimer [82].

Our data confirm the existing results even at very low density: in two dimensions the isotopes of helium behave in a vastly different way; ^{4}He form clusters [14], while ^{3}He is a homogeneous fluid up to $\rho = 0$ [13]. Studying the equation of state of bosonic ^{3}He we observe that the different behaviour of the two real isotopes of helium is not due just to the different masses but also to the different statistics.

While we do not observe any local minimum at finite densities in the equation of state of fermionic ^{3}He this is not enough to rule out the possibility of the coexistence of different fluid phases, or the presence of some instability regime. In order to study assess this we evaluate the derivative of the chemical potential μ with respect to the density ρ. In order to do so we obtain the μ from the equation of state $E(\rho)$; being U, S, V the internal energy, entropy and volume of the system and E the energy per atom we have

$$\mu = \left(\frac{\partial U}{\partial N}\right)_{S,V} = \frac{\partial(N \cdot E)}{\partial N} = E + N\frac{\partial E}{\partial \rho}\frac{\partial \rho}{\partial N} = E + \rho\frac{\partial E}{\partial \rho} \tag{3.2}$$

and then

$$\frac{\partial \mu}{\partial \rho} = 2\frac{\partial E}{\partial \rho} + \rho\frac{\partial^2 E}{\partial \rho^2}. \tag{3.3}$$

If this quantity is always positive no phase transition or phase coexistence is possible; on the other hand if it is negative we have a density range in which the system is not thermodynamically stable, as $\partial\mu/\partial\rho$ is proportional to the inverse compressibility of

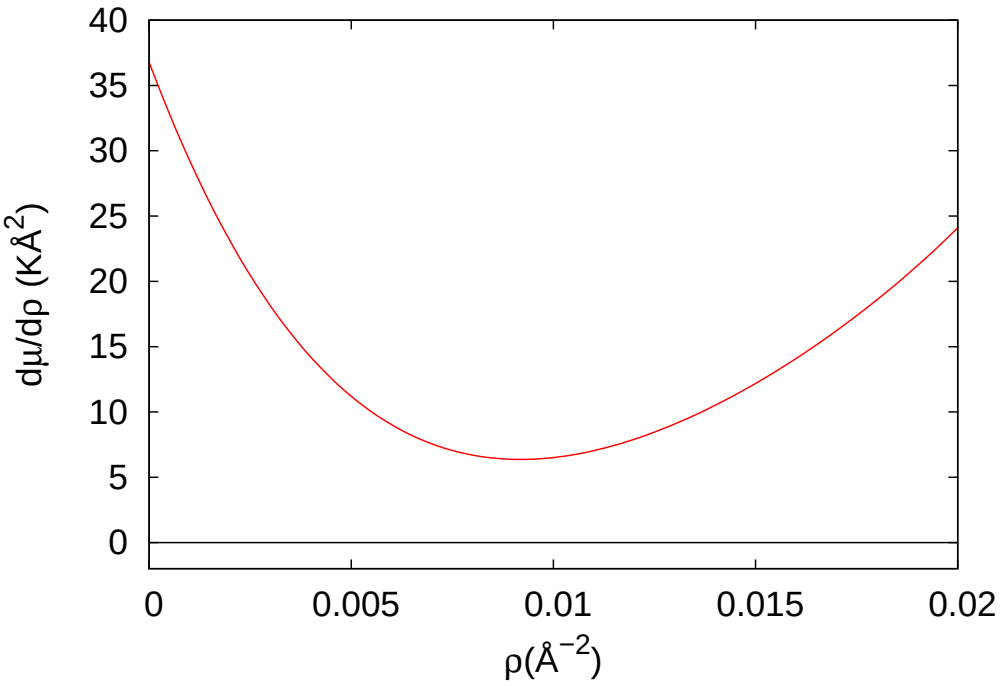

Figure 3.4: Derivative of the chemical potential as a function of the density for a two dimensional ^{3}He system, interacting with the SAPT2 potential. This quantity is always positive.

the system. In this case phase coexistence is possible, in a density range that can be determined with a Maxwell construction.

In the case of the two dimensional system this quantity is always positive, and well above zero, beyond any uncertainty on the model Hamiltonian and the accuracy of the variational simulations; this completely excludes the presence of another fluid phase. This will not be the case in presence of a substrate.

3.2 He on alkali and Mg

Even in the light of the results for the strictly two dimensional case the possibility that a ^{3}He system adsorbed on a substrate displays a condensed fluid phase can't be ruled out. In a quasi two dimensional environment in fact the presence of the zero point motion in the transverse direction has the effect of effectively softening the short distance hard core repulsion of helium atoms, in turn allowing a liquid phase to exist. When the zero point motion is larger the stabilizing effects should be larger, and so we can expect that weakly interacting substrates can better stabilize liquid ^{3}He.

We considered six weakly attractive substrates, Mg, Li, Na, K, Rb and Cs (in order of decreasing attractiveness) and determined with DMC simulations the equation of state of ^{3}He adsorbed on them. We found out that ^{3}He forms a liquid on the weakest

substrates. In particular we observe a liquid phase on the alkali substrates, with the possible exception of Li, at a density of about 0.3 Å^{-2} on Cs, Rb and K and 0.2 Å^{-2} for Na; no liquid is observed on Mg.

We simulated $N = 26$ ^{3}He atoms, with 13 atoms of either spin component, moving in three dimensions in the presence of an infinite, smooth planar substrate. The substrate is represented by an effective potential along the z axis. We used periodic boundary conditions, and the side of the simulation box along z is long enough to make the boundary conditions in that direction irrelevant.

Our Hamiltonian is

$$H = -\frac{\hbar^2}{2m}\sum_{i=1}^{N} p_i^2 + \sum_{i<j} V(r_{ij}) + \sum_{i=1}^{N} U(z_i), \tag{3.4}$$

where $V(r)$ is the interaction between helium atoms and $U(z)$ is the potential describing the interaction of the helium atoms with the substrates. To describe the helium-helium interaction we used the Aziz potential [29] while for the substrate we use the potentials proposed by Chizmeshya, Cole and Zaremba [83]. We used smooth potentials, on account of the weakness of the substrates.

We used wave functions of the form

$$\Psi(\mathbf{R}) = \Phi(\mathbf{R})J(\mathbf{R}) \cdot D(\mathbf{R}); \tag{3.5}$$

here $J(\mathbf{R})$ is a symmetric Jastrow factor to describe correlations between helium atoms, $D(\mathbf{R})$ is the product of two Slater determinants (one for each spin component) of plane waves with momenta $\mathbf{k}$ in the two dimensional Fermi disk and including backflow transformations, as described in section 2.6. The term

$$\Phi(\mathbf{R}) = \prod_{i=1}^{N} \exp(-v(z_i)), \tag{3.6}$$

where $v(z)$ is a pseudopotential of the form

$$v(z) = a_1\, z + a_2\, z^{a3}, \tag{3.7}$$

is included to localize the helium atoms in the z direction, around the minimum of $U(z)$.

We optimized the wave functions using the correlated sampling technique and evaluated the equations of state with DMC simulations; in the DMC runs we used 2000 walkers and a time step $\delta\tau = 10^{-3}$ K^{-1}. We will discuss systematic errors in our simulations at the end of this section.

The equations of state for the ideal two dimensional system and for ^{3}He adsorbed on Mg, Li, Na and K are shown in figure 3.5. The presence of a progressively weaker substrate has the effect of bending downwards the curve $E(\rho)$. On a Mg substrate, the strongest we considered, the equation of state is still monotonically increasing, and thus no stable liquid forms. We note that this means that on even more attractive substrates,

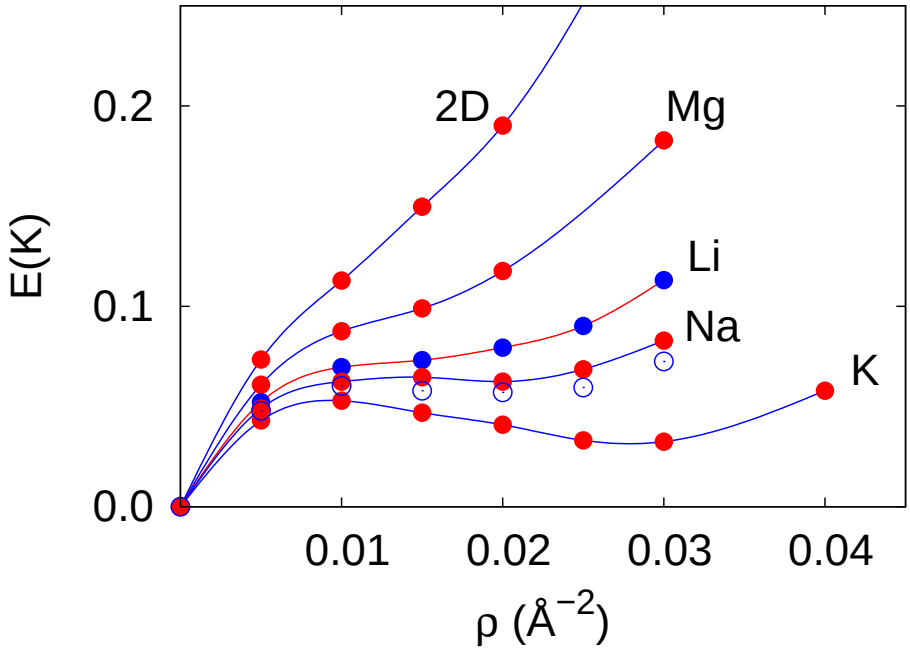

Figure 3.5: Energy as a function of the density for a system of $N = 26$ ^{3}He atoms in two dimensions and adsorbed on several weak substrates; energies were obtained with Diffusion Monte Carlo simulations using the Fixed Node approximation. The open circle set refers to an alternative data set for Li, applying corrections for system size, time step, number of walkers and nodal surface.The energy reference is the binding energy of a single atom in presence of the substrate.

such as graphite, the formation of a liquid should not be possible, in disagreement with the predictions of [24] and the interpretation of the experimental data in [38]. The downward bending of the equation of state becomes more evident as the substrate becomes weaker. On K and Na we can observe a minimum $\rho \simeq 0.03$ Å^{-2} and $\rho \simeq 0.02$ Å^{-2}, respectively, while for Li the situation is less clear. While the DMC equation of state does not displays a local minimum, we will discuss below this is a borderline case and we can't rule out the formation of a liquid at $\rho \simeq 0.015$ Å^{-2}.

In order to understand if there is some instability region in presence of substrates we computed $\frac{\partial \mu}{\partial \rho}$; we show in figure 3.6 our results. We can see that the when a weak substrate is present $\frac{\partial \mu}{\partial \rho}$ can become negative, signalling the presence of an instability region. By performing Maxwell's construction on the equations of state we can also predict phase coexistence. The phase coexistence region is between 0.0015 and 0.027 Å^{-2} for a K substrate, and it shrinks as the substrate becomes more attractive.

In order to gain insight on the properties of the adsorbed films we computed structural properties, using DMC extrapolated estimators.

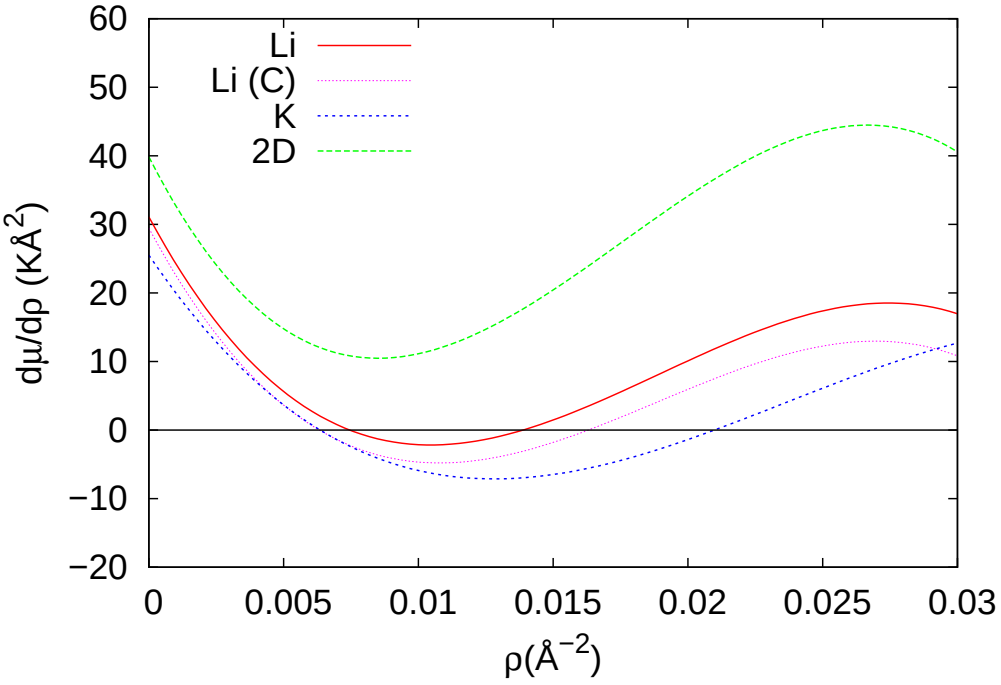

Figure 3.6: $\frac{\partial \mu}{\partial \rho}$ as a function of the density for ^{3}He adsorbed on a Li and K substrates and in two dimensions. The data set for Li with the label (C) takes into account all size corrections (see text).

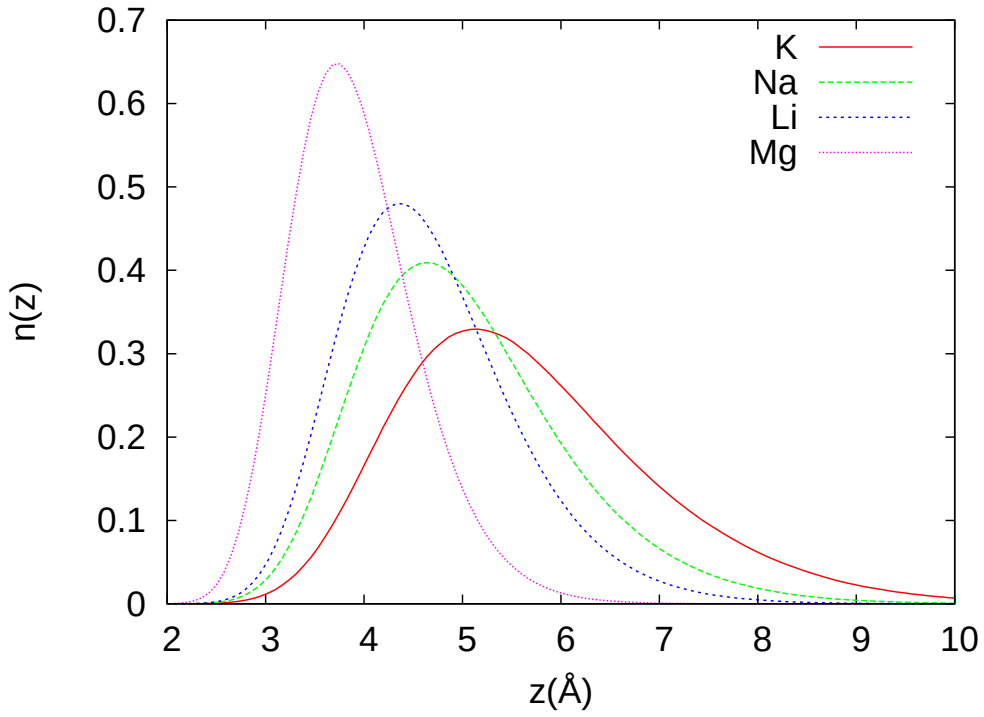

Figure 3.7: Density profiles in the z direction for ^{3}He atoms adsorbed on substrates with different interaction strengths for $\rho = 0.030$ Å^{-2} (arbitrary units). Weaker substrates lead lower and broader peaks.

We show in figure 3.7 the integrated helium density profile $n(z)$

$$n(z) = \int dxdy\rho(x, y, z), \tag{3.8}$$

where $\rho(x, y, z)$ is the three dimensional helium density, on K, Na, Li and Mg substrates. We show in figure 3.7 the results for $\rho = 0.030$ Å^{-2}; we can observe the shape of the density peaks increases with the attractiveness of the substrate, and the presence of stronger substrates leads to sharper peaks which are closer to the substrate surface. In figure 3.8 we compare the density profiles for a weak (K) and strong (Mg) substrates at different densities; we see that the shape of the peak is basically density independent on the stronger substrate, while on the weak substrate at higher coverage we see a slightly broader, less localized $n(z)$.

If broad peaks are present in $n(z)$ one might argue that a two dimensional characterization is not appropriate in the description of such a system. To investigate this possibility we measured the angularly averaged reduced pair correlation function $g(r)$, with $r = \sqrt{x^2 + y^2}$ and

$$g(x, y) = \frac{1}{A\rho} \int dx'dy'\rho(x + x', y + y')\rho(x', y') \tag{3.9}$$

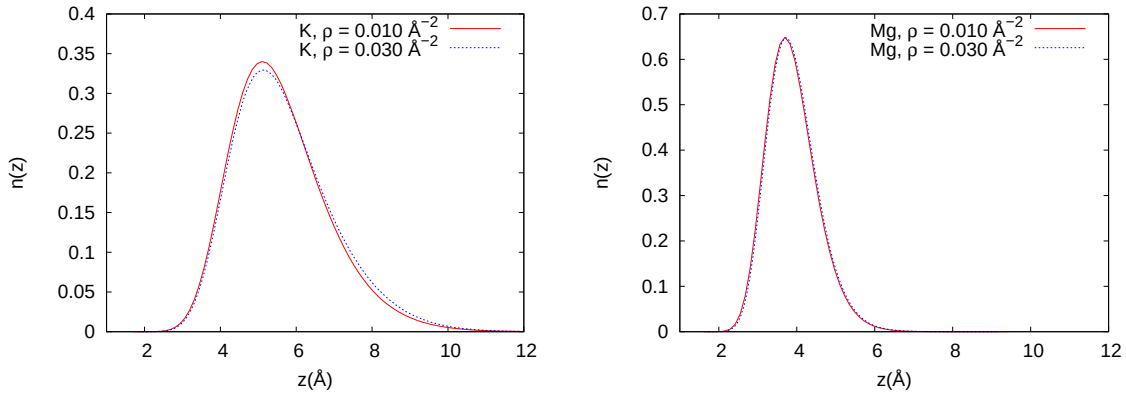

Figure 3.8: Density profiles in the z direction for ^{3}He atoms adsorbed on K (left) and Mg (right) at different densities.

with $\rho(x,y) = \int dz \rho(x,y,z)$. The more similar the $g(r)$ is to the two dimensional pair correlation function the more the two dimensional description is accurate for the adsorbed film. We show in figure 3.9 the pair correlation functions of a strictly two dimensional ^{3}He system and systems adsorbed on Mg, Li, Na and K, at coverage $\rho = 0.030$ Å^{-2}. The pair correlation functions of the strictly two dimensional case and the film adsorbed on Mg are very similar, the only difference being the height of the main peak, and the helium atoms being able to come to slightly closer r due to zero point motion in the transverse direction. A film adsorbed on a Mg substrate can be considered a close approximation of an ideal two dimensional system.

On the other hand on weaker substrates, we can observe a finite $g(r)$ at $r = 0$; this is a consequence of the large zero point motion of the atoms in the z direction, that has the effect of allowing configurations in which helium atoms can sit on top of each other; in this case we have a quasi two dimensional system. The physical result of large zero point excursions is that the hard core repulsion at short distance between adsorbed atoms becomes softer [85], less repulsive, so that the presence of a weak substrate helps the formation of a liquid. This confirms a prediction of Carraro and Cole [84], that predicted that ^{3}He can wet substrates, such as Cs, that are not wetted by ^{4}He. On the other hand more attractive substrates such as Mg or graphite display a physics closer to the two dimensional limit, in which no liquid is expected to exist.

We now consider the possible sources of bias in our estimates to assess their effect on our conclusions. For the energy these are the finite size of the system, the time step error and the population control bias in the DMC simulations and the use of the fixed node approximation. In general all this systematic errors lead to an overestimate of the energy, and their effect is stronger as the density of the system increases. As for finite size corrections we simulated systems with 26, 42 and 58 atoms, and we always found results consistent with the ones reported here. The leading finite size effect is given by the kinetic energy correction for Fermi systems, which is proportional to the density ρ and leads to a decrease of the energy; population control bias and fixed node errors also vanish in the limit $\rho \to 0$. We can conclude that the biases in our

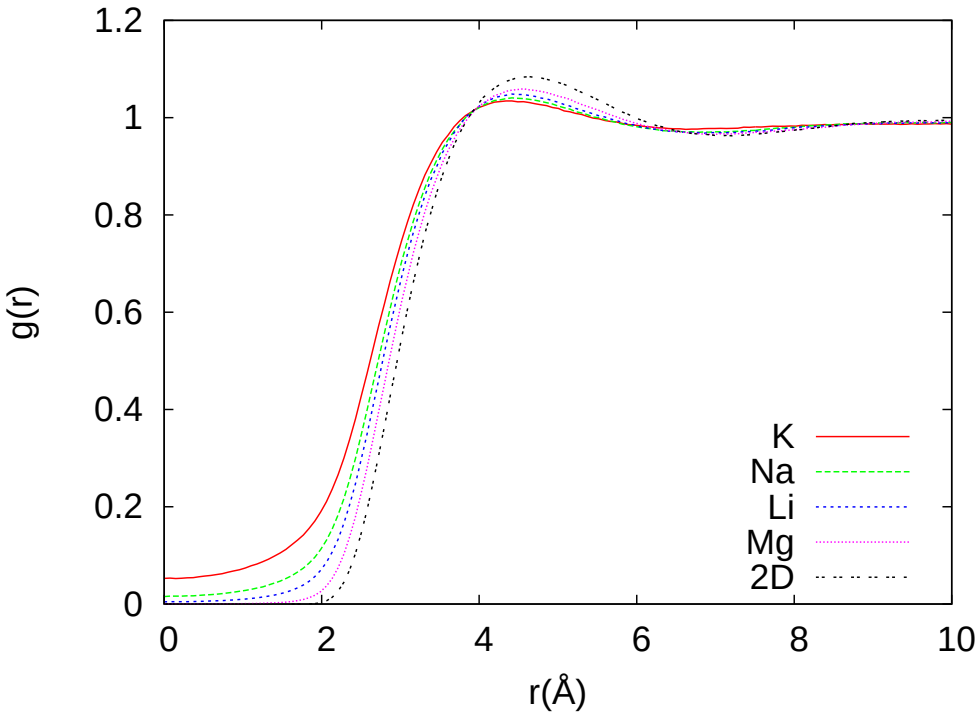

Figure 3.9: Pair correlation functions of a strictly two dimensional ^{3}He system and systems adsorbed on several substrates, at coverage $\rho = 0.030$ Å^{-2}.

estimates do not affect the conclusion that a minimum in the equation of state of ^{3}He is possible in the presence a weakly attractive substrate. On the other hand we can expect that a minimum indeed exists in the case of the Li substrate; this is suggested by the additional data set for Li in figures 3.5 and 3.6. In this additional data sets we added corrections obtained estimating all the systematic errors; in particular the magnitued of the bias in the fixed node approximation is estimated comparing the fixed node energy for a two dimensional ^{3}He system with a transient estimate [20]. The inclusion of these corrections lead to the conclusion that ^{3}He can form a liquid on a Li substrate, too, at a density of about 0.015 Å^{-2}. Performing Maxwell construction on the equation of state obtained taking into account all the mentioned sources of bias the coexistence region on Li widens, from the density range 0.005-0.016 Å^{-2} to the range 0.003-0.021 Å^{-2}. In presence of other substrates the situation is much more defined, and the inclusion of the finite size corrections does not affect the behaviour of the system.

3.3 He on graphite

In order to better understand the experimental results by Fukuyama [38, 39] we simulate ^{3}He adsorbed on a graphite substrate. The experimental data for the first and second layers are remarkably similar, so we simulate both and compare the results.

3.3.1 First layer

Graphite is a much more attractive substrate than alkali metals or Mg, so the results we obtained in the last section seem to exclude the formation of a liquid. We note that in presence of a strongly interacting substrate neglecting the corrugation may significantly affect the results of the computations. We thus include corrugation in the potential we use to describe the graphite substrate.

The Hamiltonian we use is

$$H = -\frac{\hbar^2}{2m}\sum_{i=1}^{N} p_i^2 + \sum_{i<j} V(r_{ij}) + \sum_{i=1}^{N} U(\mathbf{r}_i); \tag{3.10}$$

the helium-helium interaction $V(r)$ is modelled using the SAPT2 potential [31]; $U(\mathbf{r})$ is the helium-graphite potential developed by Carlos and Cole from beam scattering and thermodynamic experiments [27]. This potential has the form

$$U(\mathbf{r}) = U_0(z) + \sum_{\mathbf{G}} U_{\mathbf{G}}(z)\exp(i\mathbf{G}\cdot\mathbf{q}), \tag{3.11}$$

where $U_0(z)$ is a smooth potential and the second term introduces the corrugation; $\mathbf{q} = (x, y)$ is the projection of the atomic position $\mathbf{r}$ on the surface plane and $\mathbf{G}$ are reciprocal lattice vectors appropriate to the substrate. This term introduces in the potential a corrugation that is periodic, with the honeycomb lattice of the real graphite.

We modified the trial wave functions in order to take into account the corrugation. We defined a honeycomb lattice with the same spacing of the substrate and we included in the trial wave functions a new pseudopotential, to introduce correlations between the ^{3}He atoms and the sites of this lattice; this pseudopotential is a two body potential of the form 2.68

$$U_S(\mathbf{R}) = \sum_{ij} u_S(|\mathbf{r}_i - \mathbf{s}_j|), \tag{3.12}$$

where $\{\mathbf{s}_i\}$ are the coordinates of the lattice sites. These sites do not lie on the graphite surface ($z = 0$), but at $z = 2$ Å; this height was variationally determined.

We simulated an unpolarized system with $N = 18$ atoms, in periodic boundary conditions, in a surface density range from 0.005 Å^{-2} to 0.043 Å^{-2}; as in the previous computations the side of the box in the z direction is taken much longer than the other sides. As in the strictly two dimensional case (section 3.1) we included in the computation of the energy a three body Axilrod-Teller term and finite size and nodal corrections.

We show in figure 3.10 the density profile of ^{3}He on the graphite substrate, compared with two of the substrate we considered on the previous section. We can see that in presence of the more attractive graphite substrate the ^{3}He atoms are even more localized and are closer to the substrate than in the case of Mg. This is expected as the graphite substrate is more attractive than the other considered. The corrugation of the substrate does not change the expected behaviour of $n(z)$.

The effect of the corrugation is instead evident in the pair correlation function $g(r)$, shown in figure 3.11. In this case the modulation imposed by the substrate can be observed, both at low and high density.

We show in figure 3.12 the equation of state of the corrugated system, compared with the strictly two dimensional case and the smooth Cole potential obtained neglecting the second term in 3.11. The effect of the corrugation is evident. In presence of a strongly attractive substrate the equation of state is be qualitatively close to the equation of the two dimensional system, as can be seen from the equation of state of the smooth system. The corrugation has the effect of lowering the equation of state, as if the substrate were weaker. Comparing figure 3.12 with figure 3.5 we see that even if graphite is a much stronger substrate than Mg the equation of state in presence of corrugation is slightly above the equation for the weaker Na substrate. Even if there is no local minimum in the energy computing $\frac{\partial \mu}{\partial \rho}$ we can see that there is a narrow instability region (figure 3.13), and there phase coexistence region obtained with Maxwell's construction is between 0.009 Å^{-2} and 0.013 Å^{-2}.

We note that $\frac{\partial \mu}{\partial \rho}$ is only barely negative and the coexistence region we obtain is quite narrow; these results could depend on the potentials used to model the system in the simulations. to check the stability of our results we repeat our computation using different potentials, both for the substrate and for the He-He interaction, and compare the results.

To represent the graphite substrate we used the potential in [24] (which we refer to as the BJL potential) and the smooth Cole potential. A first observation is that we can't reproduce the equation of state shown in [24] (figure 1.3): as we show in figure

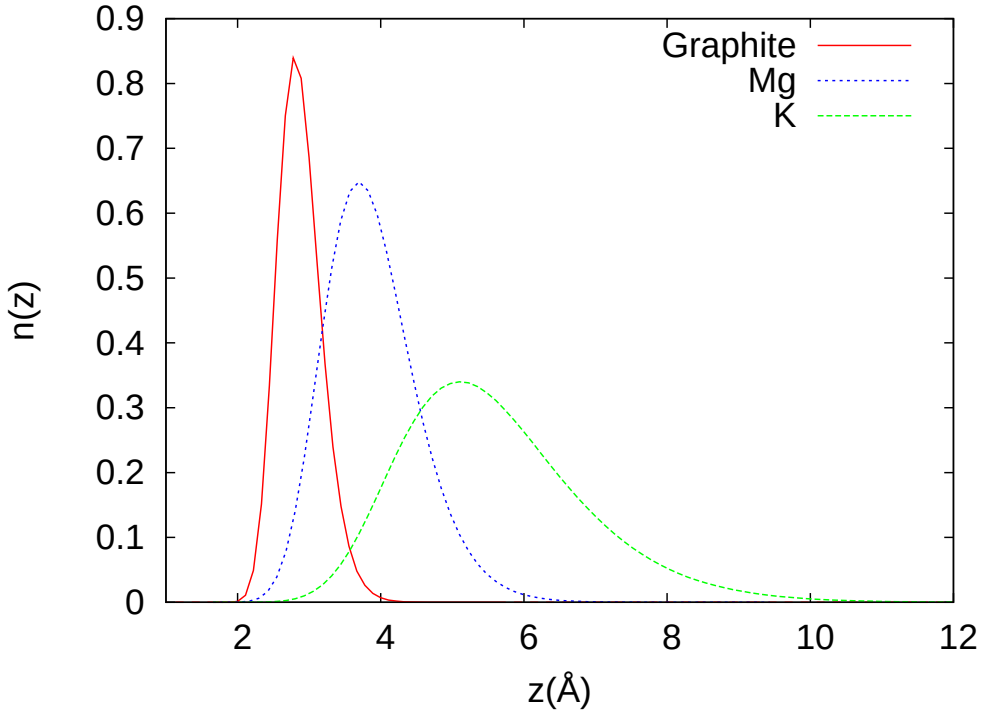

Figure 3.10: Density profiles for ^{3}He atoms adsorbed on graphite, Mg and K, at a density on 0.010 Å^{-2}.

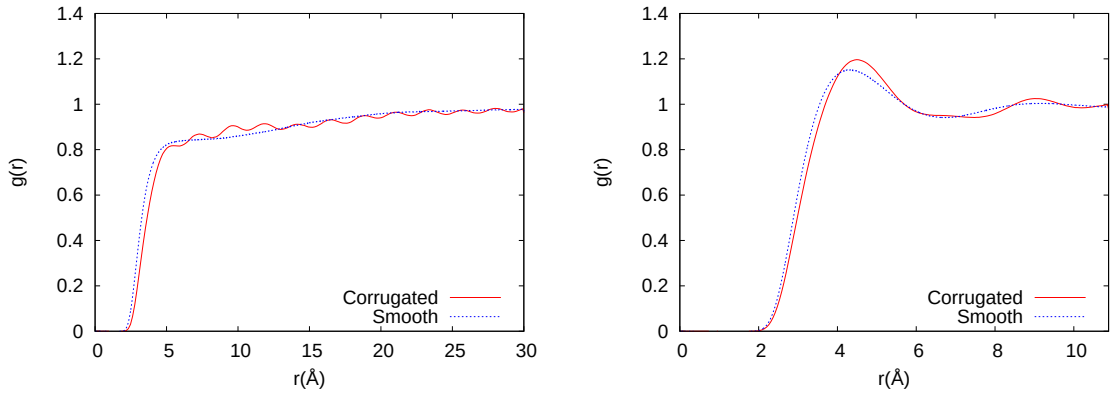

Figure 3.11: Radial correlation functions for a system with a corrugated substrate and a system with a smooth substrate and effective mass $m_B = 1.03\,m$, for $\rho = 0.005$ Å^{-2} and $\rho = 0.038$ Å^{-2} and

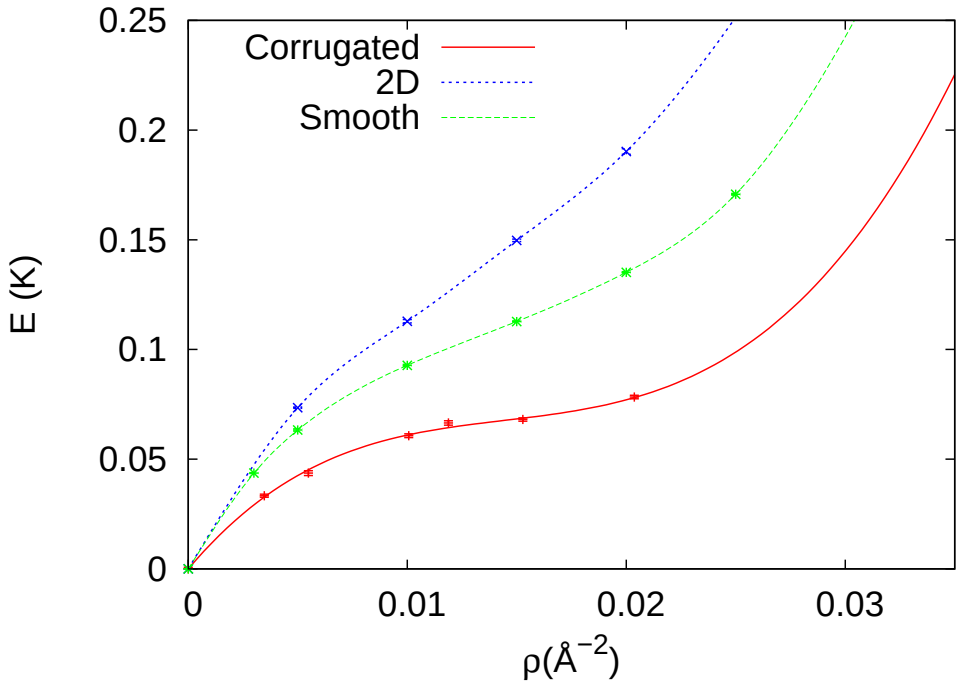

Figure 3.12: Equations of state for a system of ^{3}He atoms adsorbed on a corrugated graphite substrate, on a smooth graphite substrate and in two dimensions.

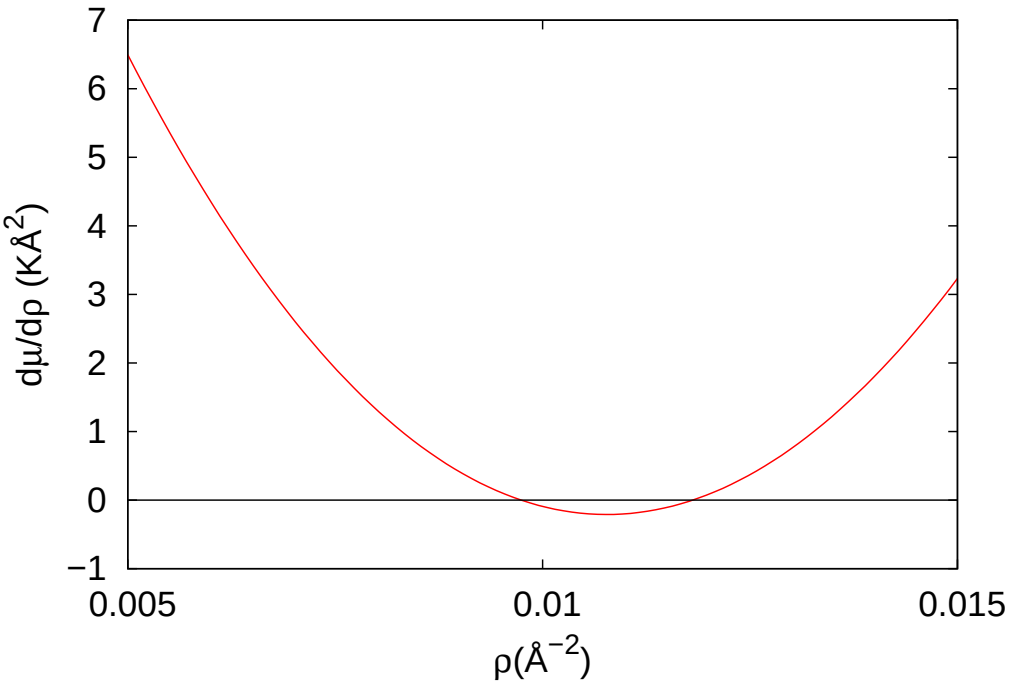

Figure 3.13: $\frac{\partial \mu}{\partial \rho}$ for ^{3}He adsorbed on graphite.

3.14 the equation of state we obtain is monotonically increasing, and no sign of a self bound liquid can be found. It is on the other hand very similar to the equation of state obtained with the smooth Cole potential, especially at low density.

Since ignoring the corrugation is a poor approximation in the modellization of a strongly interacting substrate like graphite we improved our description using a band mass for the ^{3}He atoms. With the Cole potential 3.11 the band mass was computed to be $m_B = 1.03\, m$ [28]. We show in figure 3.15 equations of state obtained with the BJL and smooth Cole potential, using the effective mass, compared with the equation of the corrugated system. The BJL equation of state in this case displays a minimum, signalling the presence of a liquid.

The equations of state obtained with the corrugated and smooth Cole potentials in this case have a good agreement. The instability regions (figure 3.16) are also quite similar, with the instability region being slightly wider with the smooth substrate. In this case the coexistence region is between 0.007 and 0.013 Å^{-2}. We show in figure 3.11 the pair correlation functions obtained with the two substrates; we can see that even if using the smooth substrate the modulation of the corrugated substrate is missing the general behaviour of the $g(x)$ is the same, both at low and high density.

We also changed the potential used to describe the helium-helium interaction. We show in figure 3.17 the equations of state obtained using the SAPT2 two body potential and the more phenomenological Aziz effective potential. The equations of state that we obtained are qualitatively similar, and none has a local minimum at a finite density;

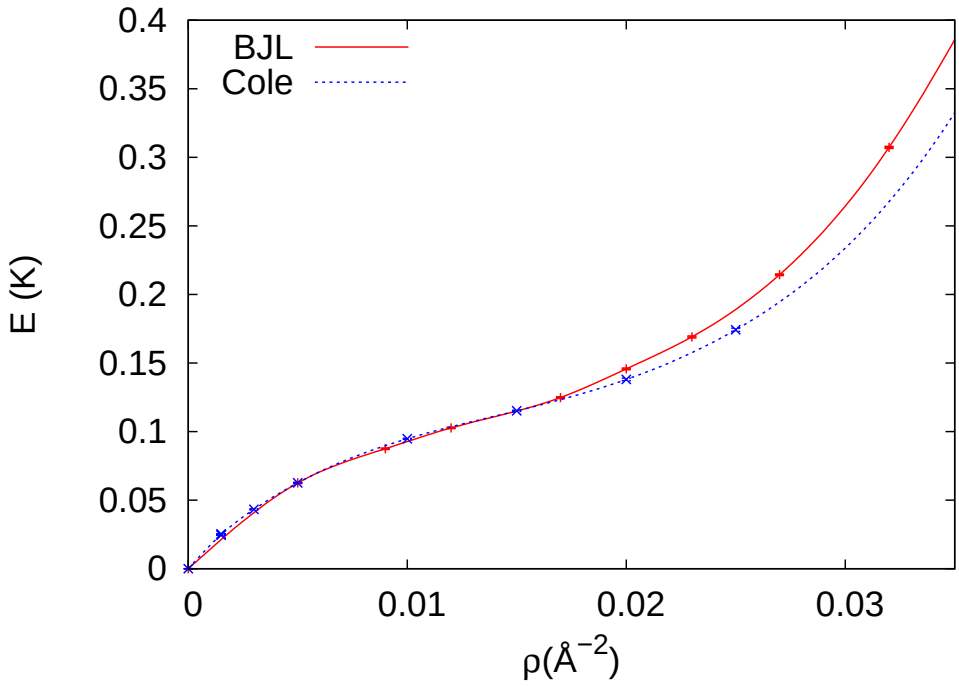

Figure 3.14: Equations of state for ^{3}He adsorbed on graphite, using smooth substrates; the BJL equation of state is very different from the result shown in [24] (figure 1.3, right panel).

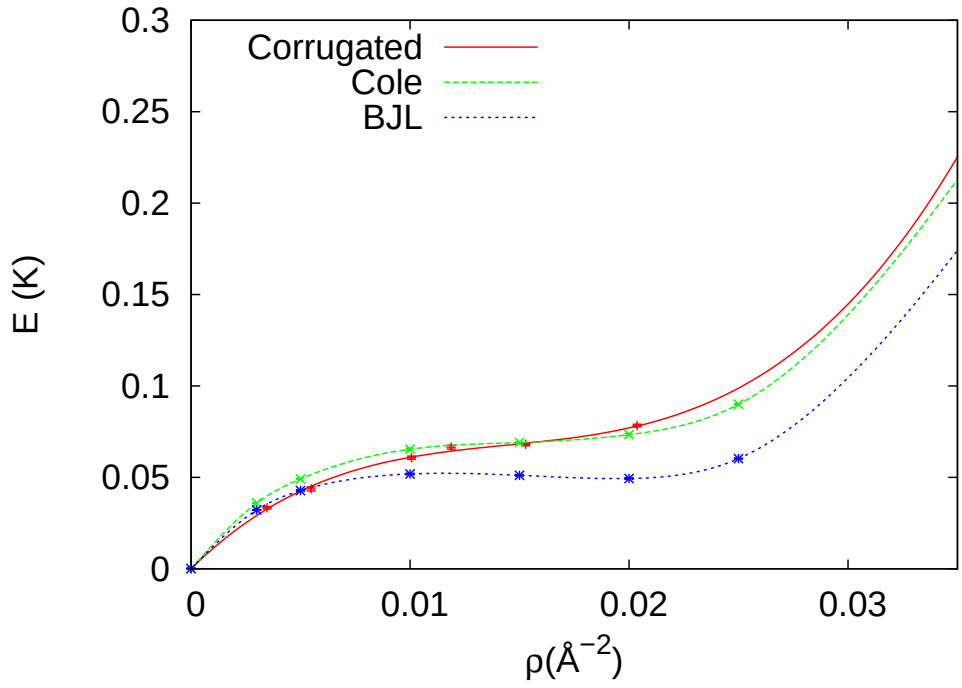

Figure 3.15: Equations of state for a system of ^{3}He atoms adsorbed on a graphite substrate in two dimensions. The substrate is described by the corrugated Cole potential, the smooth Cole potential and the BJL potential. In systems with smooth substrates the band mass $m_B = 1.03m$ is used.

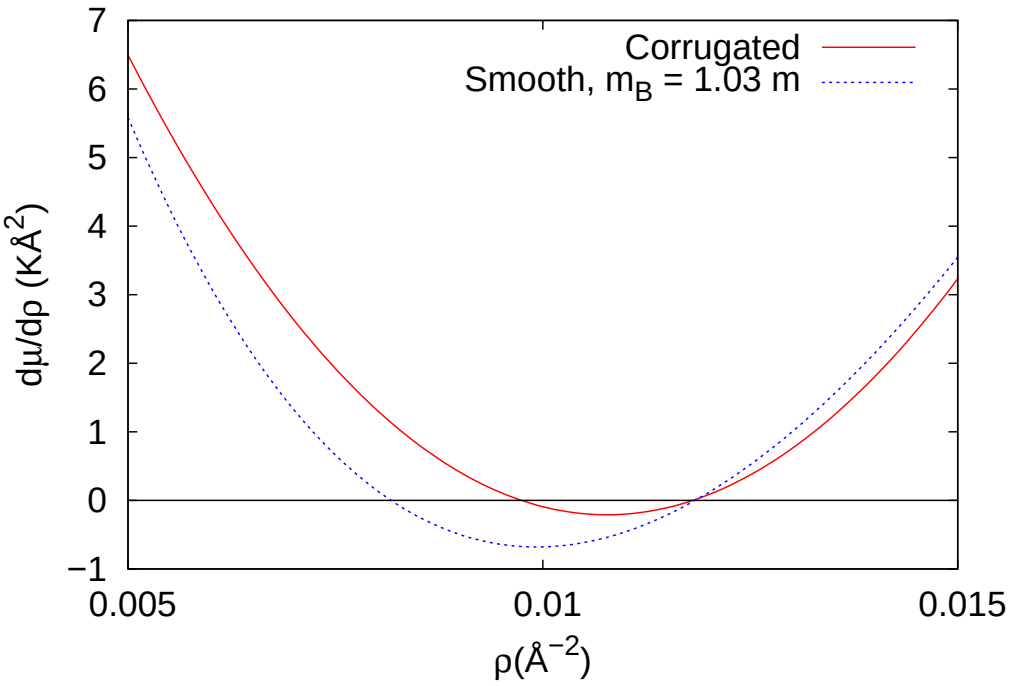

Figure 3.16: $\frac{\partial \mu}{\partial \rho}$ for ^{3}He adsorbed on graphite; the graphite is modelled using the corrugated and smooth Cole potential. With the smooth potential a band mass m_B was used.

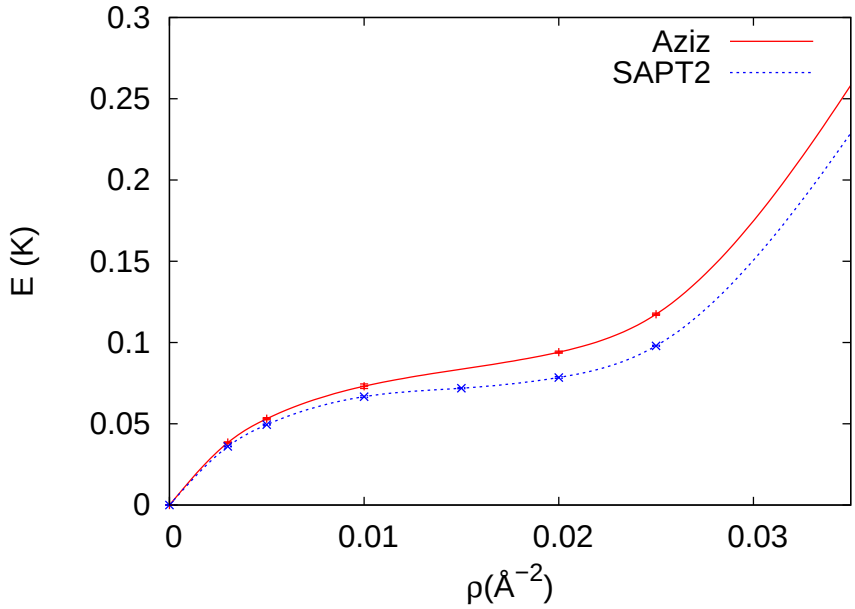

Figure 3.17: Equations of state for ^{3}He atoms on graphite; a smooth Cole potential and an effective mass are used to describe the substrate, the SAPT2 and Aziz potential are used for the helium-helium interaction.

some discrepancies growing with the density can be seen. Using the Aziz potential however we can see in figure 3.18 that the instability and coexistence regions disappear.

We conclude that in presence of corrugation we can observe phase coexistence between different fluid phases even in presence of a very strongly interacting substrate. This can be seen both describing the corrugation with an explicit dependence on the planar coordinates of the substrate potential or using a smooth substrate with an effective mass.

The results we obtain are however quite delicate, in the sense that variations in the potential we use to describe the interactions can lead to qualitatively different pictures. We observe nonetheless that the agreement between a system with the corrugated Cole potential and the smooth Cole potential with an effective mass is very good, both for the equation of state and for structural properties of the system.

3.3.2 Second layer

To study the behaviour of the second layer of ^{3}He adsorbed on substrate we include in our simulation a layer of ^{4}He. The ^{4}He have an areal density of 0.114 Å^{-2}, and form a triangular lattice that is incommensurate with the graphite substrate. We note that the large different in densities of the two helium species means that we have to simulate a large quantity of ^{4}He atoms just to simulate a few ^{3}He; this is the reason we simulated just 18 atoms on graphite, instead of the 26 on the alkali substrates; we have anyway extensively studied finite size effects to our estimate and applied suitable

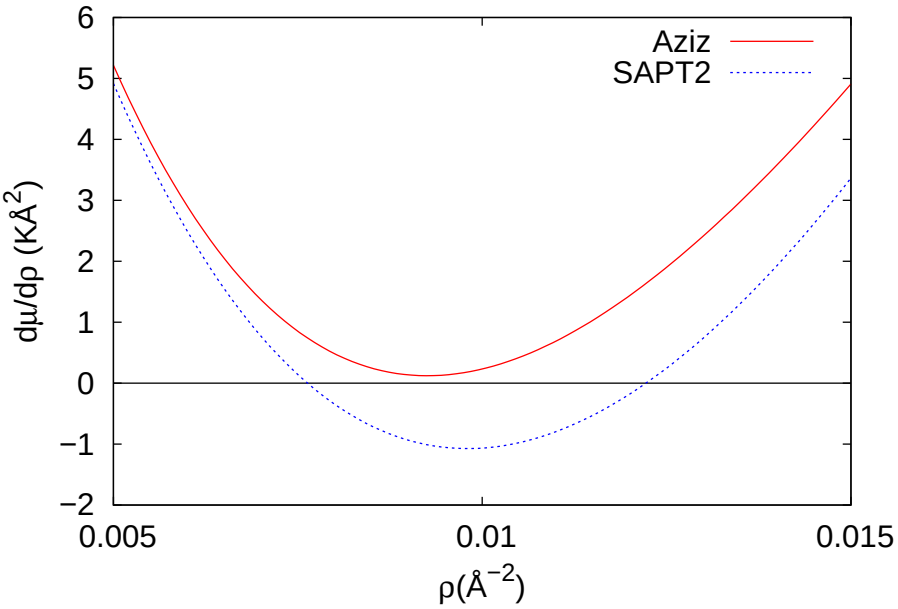

Figure 3.18: $\frac{\partial \mu}{\partial \rho}$ for ^{3}He adsorbed on graphite with helium atoms interacting via the Aziz and SAPT2 potentials; the substrate potential is the smooth Cole potential with $m_B = 1.03\, m$.

size corrections to keep possible errors under control.

In this case in our Hamiltonian we are using the smooth Cole potential, as we expect that the layer of solid ^{4}He should strongly suppress the effect of corrugation.

Our trial wave function in this case are of the form

$$\Psi(\mathbf{R}) = J(\mathbf{R})N(\mathbf{R})D(\mathbf{R}); \tag{3.13}$$

the terms $J(\mathbf{R})$ introduce interparticle correlations; in this case we have two and three body correlations for ^{3}He atoms and only two body terms for correlations between ^{4}He atoms and pairs of ^{3}He and ^{4}He atoms

$$J(\mathbf{R}) = \exp\left[-\left(U_2^{(33)}(\mathbf{R}) + U_2^{(44)}(\mathbf{R}) + U_2^{(34)}(\mathbf{R}) + U_3^{(33)}(\mathbf{R})\right)\right]; \tag{3.14}$$

the term $N(\mathbf{R})$ is a Nosanow wave function [86], to localize the ^{4}He atoms at the triangular lattice sites; $D(\mathbf{R})$ is the product of Salter determinants for the ^{3}He atoms, using two dimensional $\mathbf{k}$ vectors and backflow transformations.

We optimized the wave functions with the correlated sampling technique and then performed Diffusion Monte Carlo simulations, using a time step $\delta\tau = 5 \cdot 10^{-4}$ K^{-1}, and 6400 walkers.

In order to assess the corrugation of the first layer we computed the pair correlation function $g(x, y)$ (figure 3.19) and the radial pair correlation function $g(r)$ (3.25) and we compared with the correlation functions on the first layer; from both correlation

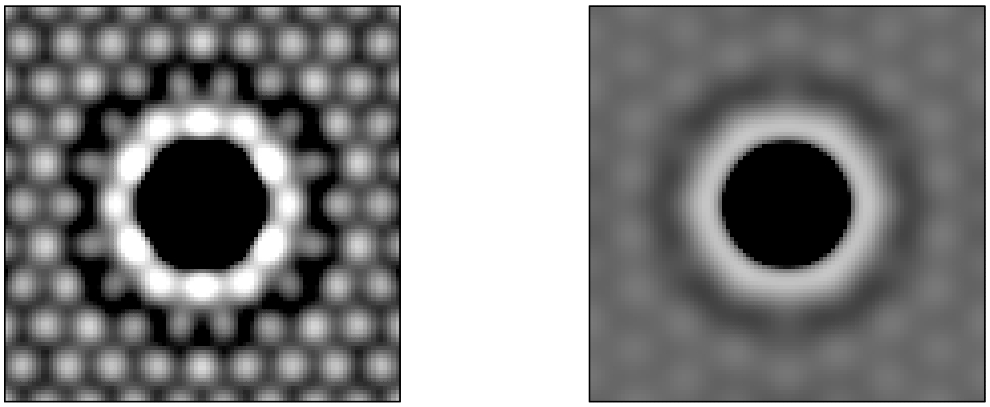

Figure 3.19: Pair correlation function $g(x, y)$ for ^{3}He atoms adsorbed on a graphite substrate on the first layer (left) and on the second layer. The black region is the excluded volume region due to hard core repulsion.

functions we can clearly see that in the second layer the corrugation is much less important than in the first; the modulations in $g(x, y)$ are much smoother, and we can see that while the $g(r)$ have the same general behaviour in the second layer there is no trace of modulation. The smaller modulation effects can be explained looking the $n(z)$ of our system. We can see in figure 3.20 that $n(z)$ has two peaks, corresponding to the first and second layers that are well separated. The second layer is very distant from the graphite substrate, and thus it is reasonable to assume that corrugation effects here will not be important. The corrugation on the first layer is not expected to have much effect on the second due to the weak interactions between helium atoms.

In presence of a first layer of ^{4}He atoms we could not obtain a reliable equation of state for ^{3}He. We show our data in figure 3.21. We observe large oscillations in the energy as a function of the density. This is due to the fact that we are interested only in the energy of the ^{3}He atoms; this energy has to be computed in DMC simulations using an extrapolated estimate. The accuracy of an extrapolated estimate depends on the quality of the trial wave function, which is in time optimized at every density. The result of the optimizations has a statistical uncertainty that is difficult to assess and influences the estimates; this leads to a bias on the energy that depends unpredictably on the density of the system. On the very small energy scale in which we are interested these fluctuations prevent the determination of an equation of state.

We note however that we can simplify our computations introducing an effective potential to describe both the graphite substrate and the layer of ^{4}He. We can safely use a smooth potential, as we have seen that in the first layer the equations of state obtained with a smooth (with effective mass) and corrugated substrates were in good agreement, and moreover we have seen that the effect of corrugation on the second

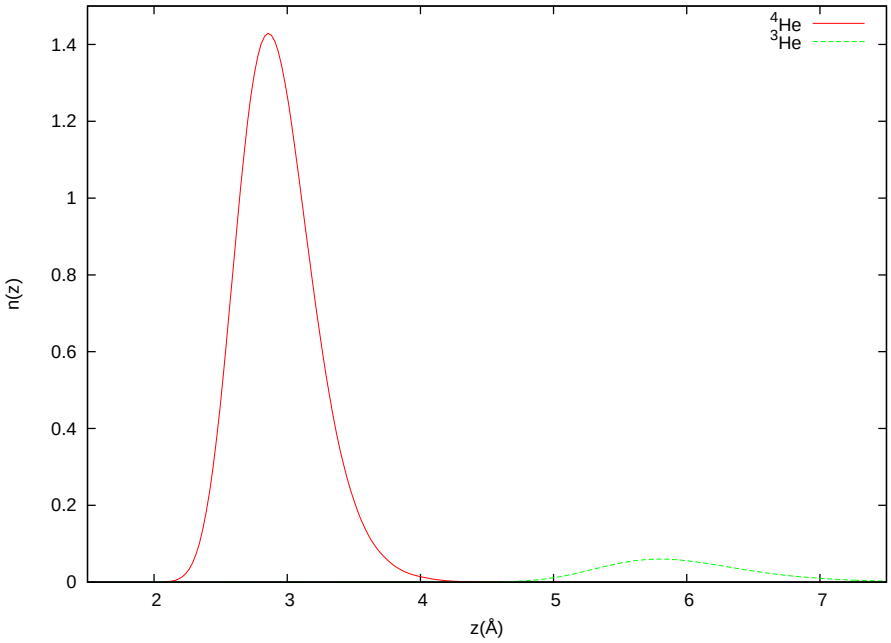

Figure 3.20: Density profile along z of two layers of He atoms adsorbed on graphite.

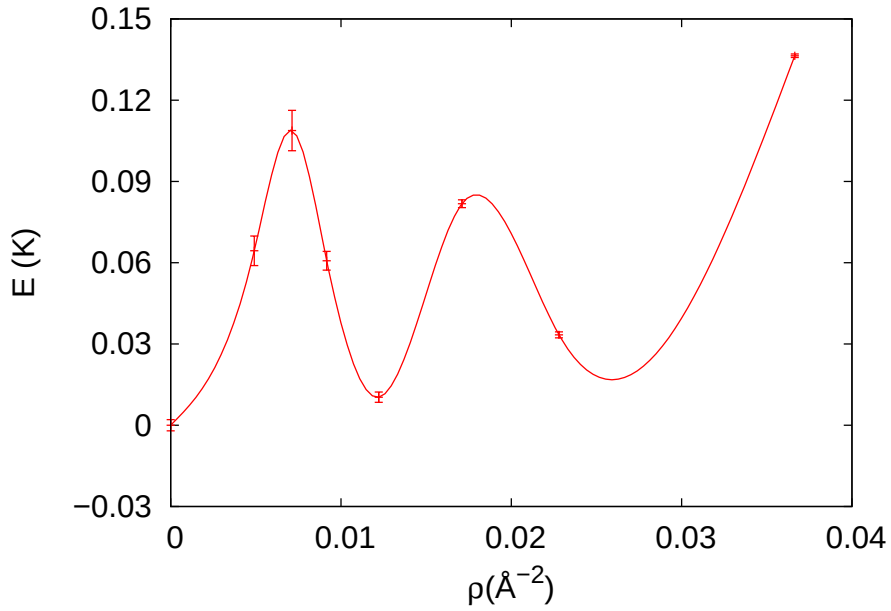

Figure 3.21: Equation of state for the second layer of ^{3}He adsorbed on a graphite substrate, obtained simulating the ^{4}He atoms in the first layer; the line is a spline interpolation.

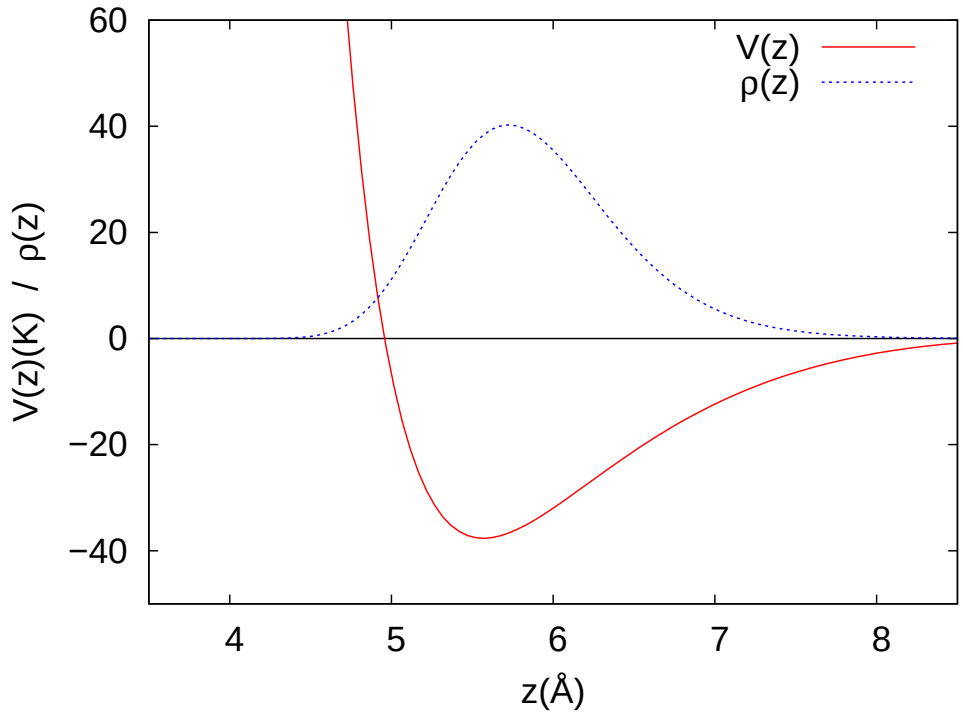

Figure 3.22: Atomic density along the z axis and the effective potential obtained from it.

layer is much smaller. We can determine a suitable potential from the evaluation of $n(z)$. From $n(z)$ in fact it is possible to evaluate an effective potential inverting Schrödinger equation; if we define an effective wave function $\psi(z) = \sqrt{\rho(z)}$ so that we have ($\lambda = \frac{\hbar^2}{2m}$)

$$-\lambda \frac{\partial^2 \psi}{\partial z^2}(z) + V(z)\psi(z) = E\psi(z) \tag{3.15}$$

the potential $V(z)$ is

$$V(z) = \lambda \frac{1}{\psi(z)} \frac{\partial^2 \psi}{\partial z^2}(z) + E, \tag{3.16}$$

where the constant E can be adjusted in order to have $V(z) \to 0$ for $z \to \infty$. The Hamiltonian containing the obtained potential has by definition as an eigenfunction the effective wave function $\psi(z)$ and so the original density $\rho(z)$ can reproduced. We show the effective potential we obtained, along with the atomic density $\rho(z)$ used to generate it, in figure 3.22.

We tested this procedure with the system on graphite without ^{4}He atoms, and using the potential we obtained from the inversion 3.16 we could compute an equation of state that is virtually identical to the one obtained with the smooth Cole potential. We can thus conclude that since our system is practically smooth we can use this effective potential to capture the behaviour of the physical system. Since the first helium layer is only weakly corrugated we do not need to adjust the effective mass of ^{3}He. We

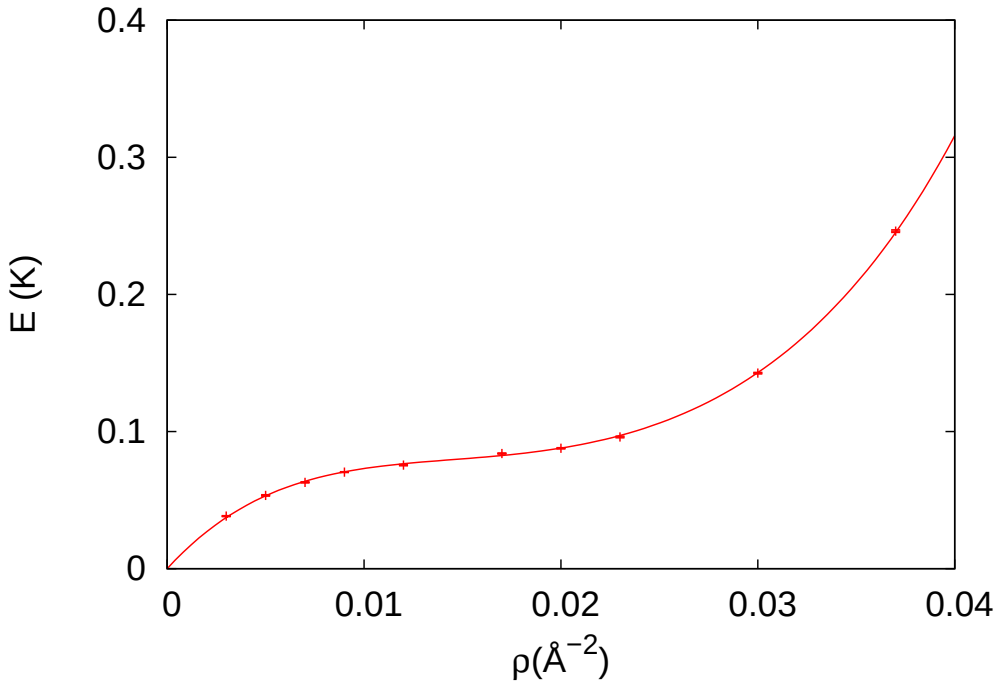

Figure 3.23: Equation of state for ^{3}He in presence of a smooth effective potential describing a graphite substrate and one layer of ^{4}He atoms.

show in figure 3.23 the equation of state we obtain using the effective potential. That the equation of state that we obtained is qualitatively similar to the equation of the first layer, without ^{4}He atoms, and a local minimum at finite density is still missing. We computed the derivative of the chemical potential, that we show in figure 3.24. We can see again an instability region, and using Maxwell's construction we obtain a coexistence region between 0.007 and 0.014 Å^{-2}. We remark that both the instability region and the zone of coexistence are close to the results for the first layer.

In order to further assess if our choice of using the effective potential is justified we computed the pair correlation functions for both the system with the smooth effective potential and the system with the ^{4}He layer. The comparison of the correlation functions are shown in figure 3.25. The pair correlation function for both systems are quite similar; in particular we note that even if we simulate a system with ^{4}He atoms the radial correlation function does not present any particular modulation: we can thus affirm that the graphite substrate and the first helium monolayer can be safely approximated by a smooth substrate.

3.4 Summary

We can confirm the existent result that two dimensional ^{3}He does not have a liquid phase: in two dimension ^{3}He is a homogeneous liquid from very low density to freezing;

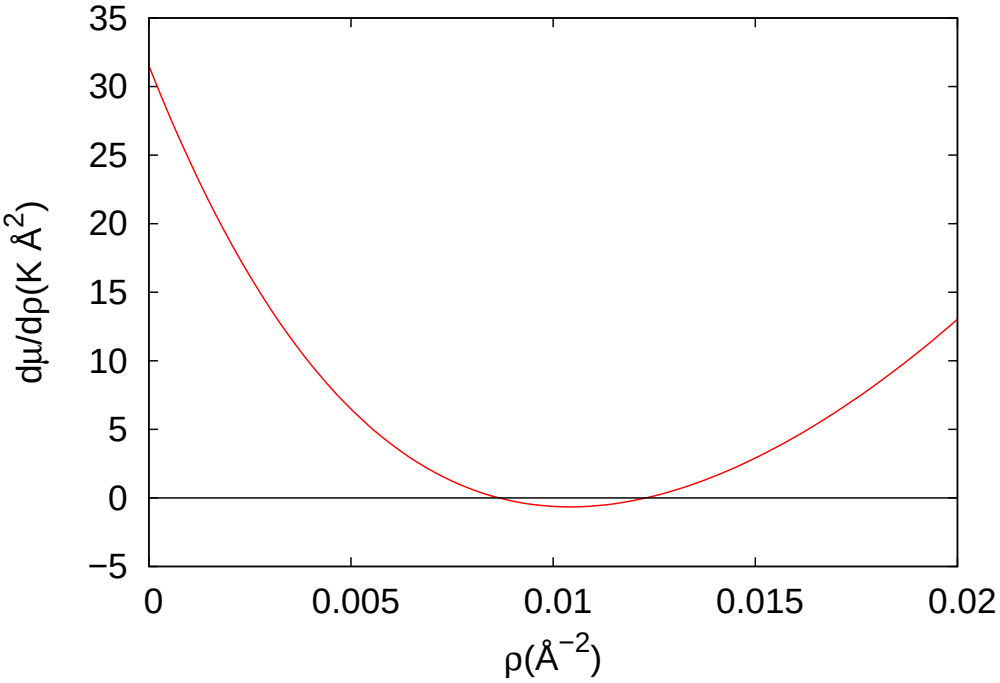

Figure 3.24: Derivative of the chemical potential for a system of $N = 18$ ^{3}He atoms with the effective potential for graphite and ^{4}He.

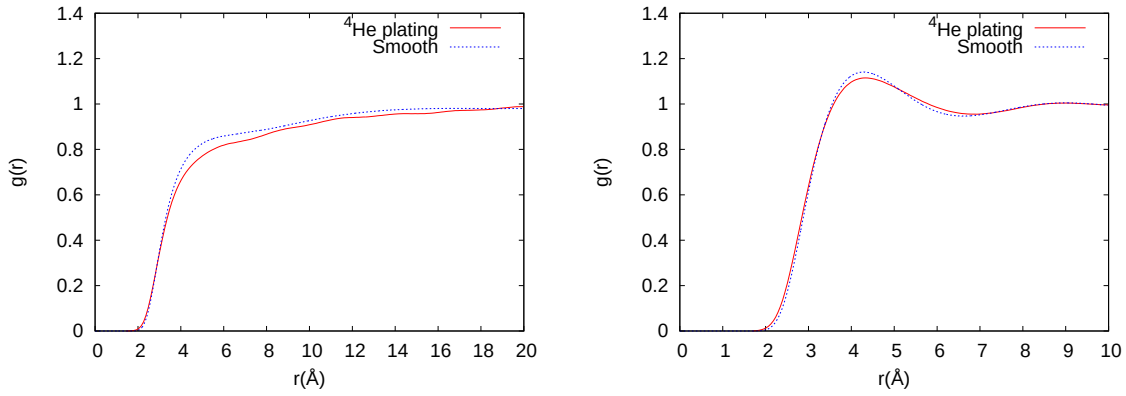

Figure 3.25: Radial correlation function $g(r)$ for ^{3}He atoms adsorbed on a graphite substrate with a layer of ^{4}He atoms (red) and with an effective potential (blue), at density 0.009 Å^{-2} and 0.038 Å^{-2}.

on the other hand computations performed in presence of substrate show another picture: zero point motion in the z direction and the presence of corrugations may lead to the stabilization of a liquid phase.

If ^{3}He is adsorbed on a weak substrate, as an alkali metal, the system shows a phase coexistence between a low density fluid and a higher density one, and the possible presence of a finite density minimum in the equation of state is the signal of a liquid phase. This is due to the fact that in presence of a weak substrate the ^{3}He atoms have a large zero point motion along z, that has the effect of effectively softening the atomic hard core repulsion.

The situation is less clear in system adsorbed on graphite; even if graphite is a very strong substrate, that should prevent the formation of a liquid phase we have seen that including the corrugation (either explicitly in the substrate potential of effectively through an effective mas for ^{3}He atoms) the coexistence of different fluid phases is possible. The results we obtained are however somewhat delicate: small changes in the potentials used to model the system may lead to qualitative changes of the observed behaviour, leading to the formation of a liquid or to the disappearance of the coexistence region.

Explicitly introducing a layer of ^{4}He in the simulation up to now has not given any satisfactory results, but the introduction of an effective potential to describe the ensemble (graphite substrate + ^{4}He plating) has made possible the determination of an equation of state. We can observe phase coexistence in the second layer too. We compare in figure 3.26 the equations of state obtained for the first and second layers. They are qualitatively similar and performing Maxwell's construction we find very similar coexistence regions on both layers. This is in line with the observations by Fukuyama [38, 39]. We argue however that this features are characteristic of ^{3}He adsorbed on graphite, and not of quasi two dimensional helium in general, as in our computations ^{3}He in two dimensions or adsorbed on alkali had significantly different behaviour.

We conclude observing that when dealing with strongly interacting substrates the situation is not very clear: in our simulations we noted that many significant factors have to be taken into account, such as the corrugation, or the presence of multiple layers, and small differences for example in the choice of the interaction potentials may lead to significant differences. We emphasize this fact as while the helium-helium interaction is described with a reasonable accuracy by the SAPT2 or Aziz potentials, the interaction between a helium atom and a carbon substrate is described with much lower precision, and this may lead to some bias in computations. Another source of error may also the modification of the interaction between helium atoms due to the presence of the substrate, an effect that to our knowledge has never been included in simulations but may have significant effects [71].

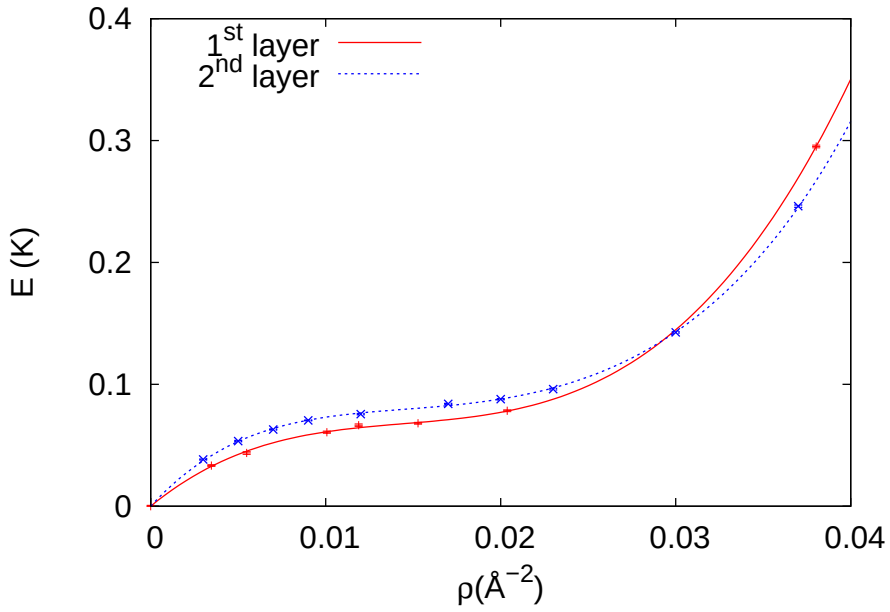

Figure 3.26: Equations of state for the first and second layer of ^{3}He adsorbed on graphite.

Chapter 4

Iterative backflow procedure for quantum fluids

Several techniques have been developed to overcome the sign problem in the study of Fermi system with projector Quantum Monte Carlo simulations; most of them however can only be used to study small systems, as their computational costs scale exponentially with the system size [19, 20, 66, 67, 68, 69]. The fixed node technique on the other hand is cheaper, as it has a polynomial scaling, and so in practice is the only available technique to obtain accurate results for large Fermi systems.

Using the Fixed Node approximation however leads to a problem: the results it allows to achieve are variational, in the sense that only an upper bound to the exact ground state energy can be estimated. In order to obtain accurate results one has to use a trial wave function, whose nodes are as close as possible to the nodes of the exact ground state. It is well known for example that using a Jastrow-Slater wave function with a Slater determinant of plane waves can give inaccurate results for strongly correlated Fermi liquids [72]. Plane waves here fail in giving a good description of the system because they completely ignore the role of correlations.

The inclusion of backflow transformations improve the simulation results for Fermi systems, but sometimes the results that are obtained fail to reproduce experimental results. Improvements and generalizations of backflow transformations can dramatically improve the Quantum Monte Carlo results [18, 2].

We designed a new class of wave functions with an improved nodal surface and more accurate nodal surfaces with the inclusion of iterative backflow transformations [2]. In this new wave functions we include pseudopotentials to include correlations between backflow coordinates and we use a Slater determinant of iteratively transformed coordinates to ensure antisymmetry. These wave functions have a modular structure that can be used to obtain a strict upper and lower bound for the exact energy, that allow to estimate the exact ground state energy of Fermi liquids.

In this chapter we review backflow coordinates and their applications in numerical simulations, then we describe our new wave functions. We show that these wave function give good results in the description of two dimensional ^{3}He at freezing, a strongly correlated Fermi system and we show they are very effective in the description

of three dimensional ^{4}He too; the success of the iterative backflow procedure in the description of a Bose system suggests that they can be useful on a scope wider than the strongly correlated Fermi systems.

4.1 Backflow coordinates

Backflow transformations were firstly introduced by Feynman and Cohen [87] for the description of excited states of liquid ^{4}He. The wave functions of the excited states of ^{4}He can be written [88] as

$$\Psi(\mathbf{R}) = \Phi(\mathbf{R}) \cdot \sum_i f(\mathbf{r}_i) \tag{4.1}$$

where $\Psi(\mathbf{R})$ is an excited state wave function, $\Phi(\mathbf{R})$ the ground state wave function, $\mathbf{r}_i$ the coordinates of the $i-$th atom and $\mathbf{R}$ the vector of the coordinates of all the atoms. $|\Psi\rangle$ is a momentum eigenstate only if $f(\mathbf{r}_i)$ are plane waves. Now we consider two examples.

Let us consider an excitation which is localized by the formation of a wave packet; the wave function thus becomes

$$\Psi(\mathbf{R}) = \Phi(\mathbf{R}) \cdot \sum_i \exp(i\mathbf{k} \cdot \mathbf{r}_i) h(\mathbf{r}_i) \tag{4.2}$$

where $h(\mathbf{r}_i)$ is a suitable function, e.g. a Gaussian. Such a wave function has a problem: it represents a wave packet that translates but that also broadens in time, an thus is unsuitable to describe a stationary state. A way to solve this problem is to include a backflow term. Backflow is taken into account by multiplying the wave function by $\exp\left[i \sum_i g(\mathbf{r}_i)\right]$, where the function $g(\mathbf{r})$ is chosen in a way that the continuity equation for the current holds and so that $g(\mathbf{r}) \to 0$ as $r \to \infty$; this is obtained generating a backflow of the helium atoms to preserve the total current. The wave function can then be written as

$$\Psi(\mathbf{R}) = \Phi(\mathbf{R}) \cdot \exp\left[i \sum_i g(\mathbf{r}_i)\right] \sum_i \exp(i\mathbf{k} \cdot \mathbf{r}_i) h(\mathbf{r}_i). \tag{4.3}$$

Let us now consider the problem of an impurity moving through liquid ^{4}He; this impurity is equal for all respects to the ^{4}He atoms, but it is not subject to Bose statistic, and has a momentum $\hbar\mathbf{k}$. A wave function that can be used to describe this situation is

$$\Psi(\mathbf{R}) = \Phi(\mathbf{R}) \exp(i\mathbf{k} \cdot \mathbf{r}_A) \tag{4.4}$$

where $\mathbf{r}_A$ is the position of the impurity. The energy of the impurity in this case is $E = \hbar^2 k^2 / 2m$. It is possible however to decrease the energy by allowing the helium atoms around the impurity to move in order to make room for it as it passes through, and then filling in the hole it leaves. This leads to a pattern flow can be defined in such a way that it involves many atoms, minimizing density fluctuations that lead to

an increase of kinetic energy. This leads to a conserved, divergence free current. Such a pattern, the backflow, can be described introducing a wave function

$$\Psi(\mathbf{R}) = \Phi(\mathbf{R}) \exp(i\mathbf{k} \cdot \mathbf{r}_A) \exp\left[i \sum_i g(\mathbf{r}_i - \mathbf{r}_A) \right]; \tag{4.5}$$

we can define an excitation such as a phonon or a roton for liquid ^{4}He dropping the impurity and symmetrizing the previous wave function, obtaining a backflow pattern around each helium atom

$$\Psi(\mathbf{R}) = \Phi(\mathbf{R}) \sum_i \exp(i\mathbf{k} \cdot \mathbf{r}_i) \exp\left[i \sum_{j \neq i} g(\mathbf{r}_i - \mathbf{r}_j); \right] \tag{4.6}$$

since the function $g(\mathbf{r})$ describing the pattern is proportional to the wave vector $\mathbf{k}$ [87] the wave function can be written as

$$\Psi(\mathbf{R}) = \Phi(\mathbf{R}) \sum_i \exp(i\mathbf{k} \cdot \mathbf{x}_i); \tag{4.7}$$

where $\mathbf{x}_i$ are the transformed backflow coordinates

$$\mathbf{x}_i = \mathbf{r}_i + \sum_j (\mathbf{r}_i - \mathbf{r}_j) \eta(r_{ij}) \tag{4.8}$$

and $\eta(r)$ is a suitable function, variationally determined.

In both examples we see that backflow is a collective flow of the atoms in a quantum fluid, than is introduced to describe excitations. It has the effect of preserving the total current in presence of a moving wave packet and of reducing the total energy of the system when a particle is moving through the fluid.

While backflow transformations were introduced to study excitations of Bose systems they found a lot of applications in the study of ground states of Fermi systems [89]: backflow coordinates are in fact often used in trial wave functions of Variational or Diffusion Monte Carlo simulations. In particular they are used in the Slater determinant part of fermionic wave functions. These wave functions were used to study systems such as ^{3}He [13, 72, 73, 74, 75, 76, 89] or the electron gas [77, 78, 79]. Failing to include backflow transformations leads to somewhat inaccurate results at high density: the inclusion of backflow transformations in fact significantly improves the description of interparticle correlations and provide a much more accurate nodal surfaces; this is especially important when using the Fixed Node approximation.

It should be noted however that there is still room for improvement: using simple backflow transformations as 2.67 can results in important differences between simulations and experiments. As an example a three-body (and possibly more-body) term has to be included to stabilize the unpolarized ground state of ^{3}He against spin polarization [18]. Other generalizations and improvements can of course be designed.

4.2 Iterative backflow procedure

We have designed a class of new trial wave functions based on iterative backflow transformations: instead of using just one set of backflow coordinates we use an iterative procedure to generate several orders of backflow coordinates, and then include interparticle correlation among these auxiliary coordinates.

Let us consider a Fermi system. Such a system can be described by a wave function of the form

$$\Psi^{(1)}(\mathbf{R}) = J(\mathbf{R}) \cdot \chi(\mathbf{X}^{(1)}) \tag{4.9}$$

where $\mathbf{R}$ is a vector containing all the atomic coordinates, $\mathbf{X}^{(1)}$ is a vector containing the transformed backflow coordinates 4.8, $J(\mathbf{R})$ is a Jastrow function taking into account interparticle correlations and $\chi(\mathbf{X})$ is a product of Slater determinants of plane waves, including backflow transformations. Once the Jastrow and backflow pseudopotentials have been determined it is possible to approximate the excited states of the systems using different occupation numbers for the orbital in the Slater determinant, effectively creating particles and holes, in analogy with Landau's Fermi liquid theory. Let us now consider an effective Hamiltonian, as in the correlated basis function approach [90, 91], within this non orthogonal basis set; for a Fermi liquid the off diagonal matrix elements of the effective Hamiltonian will be strongly suppressed with respect the off diagonal elements of bare plane waves. The idea is that instead of diagonalizing the effective Hamiltonian we instead redefine a new trial wave function, to approximate the ground state of the effective Hamiltonian. Assuming a smoothly varying effective interaction we can define the new trial wave function introducing new backflow transformations, using instead of the bare coordinates the backflow coordinates 2.67

$$\mathbf{x}_i^{(2)} = \mathbf{x}_i^{(1)} + \sum_j (\mathbf{x}_i^{(1)} - \mathbf{x}_j^{(1)}) \eta^{(1)}(x_{ij}^{(1)}) \tag{4.10}$$

We also introduce correlation between backflow coordinates defining a new Jastrow term $J^{(1)}(\mathbf{X}^{(1)})$, so that the wave function becomes

$$\Psi^{(2)}(\mathbf{R}) = J(\mathbf{R}) \cdot J^{(1)}(\mathbf{X}^{(1)}) \cdot \chi(\mathbf{X}^{(2)}). \tag{4.11}$$

This procedure can then be iterated, to generate wave function of the type

$$\Psi^{(M)}(\mathbf{R}) = J(\mathbf{R}) \cdot \prod_{m=1}^{M-1} J^{(m)}(\mathbf{X}^{(m)}) \cdot \chi(\mathbf{X}^{(M)}) = \prod_{m=0}^{M-1} J^{(m)}(\mathbf{X}^{(m)}) \cdot \chi(\mathbf{X}^{(M)}) \tag{4.12}$$

using backflow transformations of the form

$$\mathbf{x}_i^{(m)} = \mathbf{x}_i^{(m-1)} + \sum_j (\mathbf{x}_i^{(m-1)} - \mathbf{x}_j^{(m-1)}) \eta^{(m-1)}(x_{ij}^{(m-1)}); \tag{4.13}$$

in this notation the superscript (0) refers to the original atomic coordinates or pseudopotentials, while the wave function $\Psi^{(0)}(\mathbf{R})$ is a Jastrow-Slater wave function without backflow transformations.

Our new wave functions give better variational energies not only because the increased number of Jastrow factors results in a more flexible description of interparticle interactions; each time we include a new backflow transformation in the wave function we are reducing the correlations between the coordinates used to compute the Slater determinant. We can describe their correlation introducing a new Jastrow factor and introduce a new set of auxiliary particles that are even less correlated, via a new backflow transformation. Every time we perform a backflow transformation we obtain new pseudo particles that are less correlated, and for which the nodes of a Slater determinants of plane waves become more accurate.

We note that in general the pseudopotentials describe two and three body correlations and the ones in the backflow transformations are not equal at each order, and they have to be separately optimized. Moreover each time we add an iteration all the pseudopotentials already present have to be reoptimized. This lead to a longer variational optimization procedure, each time with more and more variational parameters. On the other hand the computational cost of a single simulations does not significantly increase: with the procedure described below we have an algorithm whose complexity scales as N^3, where N is the number of atoms in the simulation, just as when we use a wave function with regular backflow; in the simulation of a system on $N = 26$ atoms with $M = 2, \ldots, 5$ backflow transformations we found that the CPU time necessary to perform the estimates was 5, 9, 13, 17 times longer than the time needed using one standard backflow transformation ($M = 1$). Simulating a system of 58 atoms took a time 12.5 longer than simulating a system with 26 atoms, using 5 transformation in both cases; this scaling is close to the N^3 scaling of conventional backflow wave functions.

4.3 Derivatives of the wave functions

In this section we generalize the procedure illustrated in subsection 2.7 to compute the local energy using a wave function with iterative backflow transformation. We shall focus on the kinetic part of the local energy, as again the potential part can be straightforwardly obtained from the atomic positions in the configurations.

To compute the kinetic part of the local energy of this part we need to compute the gradient and the Laplace operator of the logarithm of the wave functions 4.12.

We start from the simplest case, $\Psi^{(2)}(\mathbf{R})$. We first consider the two body correlation between the backflow particles whose coordinates are $\mathbf{X}^{(1)} = \mathbf{X}$. In this computations we are going to use the matrices $A_{ij}^{\alpha\beta}$ and B_{ij}^{β} defined in subsection 2.7

$$\begin{aligned} A_{ij}^{\alpha\beta} &= \frac{\partial x_j^\beta}{\partial r_i^\alpha} \\ B_{ij}^{\beta} &= \sum_\alpha \frac{\partial^2 x_j^\beta}{\partial r_i^\alpha \partial r_i^\alpha} = \sum_\alpha \frac{\partial A_{ij}^{\alpha\beta}}{\partial r_i^\alpha}. \end{aligned} \tag{4.14}$$

We start from the two body pseudopotential for the backflow coordinates. The

logarithm of this term is

$$U_2^{(1)}(\mathbf{X}) = \sum_{j<k} u^{(1)}(x_{jk}); \tag{4.15}$$

its gradient is computed using the chain rule

$$\begin{aligned} \nabla_i^\alpha U_2^{(1)}(\mathbf{X}) &= \sum_{j<k} \frac{\partial u^{(1)}}{\partial r_i^\alpha}(x_{jk}) = \sum_{j<k} \frac{\partial u^{(1)}}{\partial x_{jk}}(x_{jk}) \frac{\partial x_{jk}}{\partial r_i^\alpha} = \\ &= \sum_{j<k} \sum_{l\beta} u'^{(1)}(x_{jk}) \frac{\partial x_{jk}}{\partial x_l^\beta} \frac{\partial x_l^\beta}{\partial r_i^\alpha} = \sum_{l\beta} T_l^\beta A_{il}^{\alpha\beta} \end{aligned} \tag{4.16}$$

where

$$u'^{(1)}(x_{jk}) = \frac{\partial u^{(1)}}{\partial x_{jk}} \tag{4.17}$$

and we defined the matrix T_l^β as

$$T_l^\beta = \sum_{j\neq l} \frac{u'^{(1)}(x_{jl})}{x_{jl}} x_{jl}^\beta. \tag{4.18}$$

We now obtain the Laplacian

$$\begin{aligned} \Delta U_2^{(1)} &= \sum_{i,\alpha} \frac{\partial^2 U_2^{(1)}}{\partial r_i^\alpha \partial r_i^\alpha} = \sum_{i,\alpha} \frac{\partial}{\partial r_i^\alpha} \left(\sum_{l\beta} T_l^\beta A_{il}^{\alpha\beta} \right) = \\ &= \sum_{l\beta} \sum_{i\alpha} \frac{\partial A_{il}^{\alpha\beta}}{\partial r_i^\alpha} T_l^\beta + \sum_{l\beta} \sum_{i\alpha} \frac{\partial T_l^\beta}{\partial r_i^\alpha} A_{il}^{\alpha\beta} = \\ &= \sum_{il\beta} T_l^\beta B_{il}^\beta + \sum_{il\alpha\beta} \frac{\partial T_l^\beta}{\partial r_i^\alpha} A_{il}^{\alpha\beta}. \end{aligned} \tag{4.19}$$

We now consider the derivative $\frac{\partial T_l^\beta}{\partial r_i^\alpha}$; from the definition 4.18 we have

$$\begin{aligned} \frac{\partial T_l^\beta}{\partial r_i^\alpha} &= \frac{\partial}{\partial r_i^\alpha} \left(\sum_{j\neq l} x_{jl}^\beta \frac{u'^{(1)}(x_{jl})}{x_{jl}} \right) = \\ &= \sum_{j\neq l} \left(A_{ij}^{\alpha\beta} - A_{il}^{\alpha\beta} \right) \frac{u'^{(1)}(x_{jl})}{x_{jl}} + \sum_{m,\gamma} \left(u''^{(1)}(x_{jl}) - \frac{u'^{(1)}(x_{jl})}{x_{jl}} \right) \frac{x_{jl}^\beta x_{jl}^\gamma}{x_{jl}^2} \cdot \\ &\quad \cdot (\delta_{mj} - \delta_{ml}) A_{im}^{\alpha\gamma} = \\ &= \sum_{j\neq l,\gamma} \left[\delta^{\beta\gamma} \left(A_{ij}^{\alpha\gamma} - A_{il}^{\alpha\gamma} \right) \frac{u'^{(1)}(x_{jl})}{x_{jl}} + \left(u''^{(1)}(x_{jl}) - \frac{u'^{(1)}(x_{jl})}{x_{jl}} \right) \frac{x_{jl}^\beta x_{jl}^\gamma}{x_{jl}^2} \left(A_{ij}^{\alpha\gamma} - A_{il}^{\alpha\gamma} \right) \right] \end{aligned} \tag{4.20}$$

we can then define the quantity

$$W_{jl}^{\beta\gamma} = \left(u''^{(1)}(x_{jl}) - \frac{u'^{(1)}(x_{jl})}{x_{jl}} \right) \frac{x_{jl}^{\beta} x_{jl}^{\gamma}}{x_{jl}^2} + \delta^{\beta\gamma} \frac{u'^{(1)}(x_{jl})}{x_{jl}} \tag{4.21}$$

so that we obtain

$$\frac{\partial T_l^{\beta}}{\partial r_i^{\alpha}} = \sum_{j \neq l, \gamma} W_{jl}^{\beta\gamma} \left(A_{ij}^{\alpha\gamma} - A_{il}^{\alpha\gamma} \right); \tag{4.22}$$

moreover if we define the matrix

$$\overline{A}_{lm}^{\alpha\beta} = \sum_{i\gamma} A_{il}^{\gamma\alpha} A_{im}^{\gamma\beta}. \tag{4.23}$$

we can finally obtain

$$\Delta U_2^{(1)}(\mathbf{X}) = \sum_{il\beta} T_l^{\beta} B_{il}^{\beta} + \sum_{l \neq j} \sum_{\beta\gamma} W_{jl}^{\beta\gamma} \left(\overline{A}_{jl}^{\gamma\beta} - \overline{A}_{ll}^{\gamma\beta} \right). \tag{4.24}$$

We now construct new backflow coordinates $\mathbf{X}^{(2)} = \mathbf{Y}$, and compute the gradient and Laplacian of the Slater determinant obtained using these new coordinates (the three body correlations between the backflow coordinates $\mathbf{X}^{(1)}$ will be addressed later). We start from the definition of the new coordinates

$$y_i^{\alpha} = x_i^{\alpha} + \sum_{j \neq i} x_{ij}^{\alpha} \eta^{(1)}(x_{ij}) \tag{4.25}$$

where $\eta^{(2)}$ is the corresponding backflow pseudopotential. We need now to compute the derivatives

$$Y_{ij}^{\alpha\beta} = \frac{\partial y_j^{\beta}}{\partial r_i^{\alpha}}, \quad Z_{ij}^{\beta} = \sum_{\alpha} \frac{\partial^2 y_j^{\beta}}{\partial r_i^{\alpha} \partial r_i^{\alpha}} = \sum_{\alpha} \frac{\partial Y_{ij}^{\alpha\beta}}{\partial r_i^{\alpha}}. \tag{4.26}$$

Let us focus on $Y_{ij}^{\alpha\beta}$; using the chain rule an the definition of the matrix A we have

$$Y_{ij}^{\alpha\beta} = \frac{\partial y_j^{\beta}}{\partial r_i^{\alpha}} = \sum_{k\gamma} \frac{\partial y_j^{\beta}}{\partial x_k^{\gamma}} \frac{\partial x_k^{\gamma}}{\partial r_i^{\alpha}} = \sum_{k\gamma} \frac{\partial y_j^{\beta}}{\partial x_k^{\gamma}} A_{ik}^{\alpha\gamma}; \tag{4.27}$$

we now evaluate the derivative $\frac{\partial y_j^{\beta}}{\partial x_k^{\gamma}}$, using the backflow transformation 4.25 and the analogue for x of the derivatives 2.71

$$\begin{aligned} \frac{\partial y_j^{\beta}}{\partial x_k^{\gamma}} &= \frac{\partial}{\partial x_k^{\gamma}} \left(x_j^{\beta} + \sum_{l \neq j} x_{jl}^{\beta} \eta^{(1)}(x_{jl}) \right) = \\ &= \delta_{kj}^{\gamma\alpha} + \sum_{l \neq j} \delta^{\gamma\beta} (\delta_{jk} - \delta_{lk}) \eta^{(1)}(x_{jl}) + x_{jl}^{\beta} \frac{\partial \eta^{(1)}(x_{jl})}{\partial x_{jl}} \frac{x_{jl}^{\gamma}}{x_{jl}} (\delta_{jk} - \delta_{lk}) = \\ &= \delta_{kj}^{\gamma\alpha} + \sum_{l \neq j} (\delta_{jk} - \delta_{lk}) \left[\delta^{\gamma\beta} \eta^{(1)}(x_{jl}) + x_{jl}^{\beta} x_{jl}^{\gamma} \frac{\eta'^{(1)}(x_{jl})}{x_{jl}} \right] \end{aligned} \tag{4.28}$$

defining the quantity

$$\dot{h}_{jl}^{\gamma\beta} = \delta^{\gamma\beta}\eta^{(1)}(x_{jl}) + \frac{\eta'^{(1)}(x_{jl})}{x_{jl}} x_{jl}^{\gamma} x_{jl}^{\beta} \tag{4.29}$$

we finally obtain

$$\begin{aligned} Y_{ij}^{\alpha\beta} &= \sum_{k\gamma} \frac{\partial y_j^{\beta}}{\partial x_k^{\gamma}} A_{ik}^{\alpha\gamma} = \sum_{k\gamma} \left[\delta_{kj}^{\gamma\alpha} + \sum_{l\neq j} (\delta_{jk} - \delta_{lk}) \dot{h}_{jl}^{\gamma\beta} \right] A_{ik}^{\alpha\gamma} = \\ &= A_{ij}^{\alpha\beta} + \sum_{l\neq j,\gamma} \dot{h}_{jl}^{\gamma\beta} (A_{ij}^{\alpha\gamma} - A_{il}^{\alpha\gamma}) \end{aligned} \tag{4.30}$$

We now consider the matrix Z_{ij}^{β} with the second derivatives; we have

$$Z_{ij}^{\beta} = \sum_{\alpha} \frac{\partial Y_{ij}^{\alpha\beta}}{\partial r_i^{\alpha}} = \sum_{\alpha} \left[\frac{\partial A_{ij}^{\alpha\beta}}{\partial r_i^{\alpha}} + \sum_{l\neq j,\gamma} \left[\frac{\partial \dot{h}_{jl}^{\gamma\beta}}{\partial r_i^{\alpha}} (A_{ij}^{\alpha\gamma} - A_{il}^{\alpha\gamma}) + \dot{h}_{jl}^{\gamma\beta} \left(\frac{\partial A_{ij}^{\alpha\gamma}}{\partial r_i^{\alpha}} - \frac{\partial A_{il}^{\alpha\gamma}}{\partial r_i^{\alpha}} \right) \right] \right]. \tag{4.31}$$

Using the matrix B in 4.14 and the chain rule we have

$$Z_{ij}^{\beta} = B_{ij}^{\beta} + \sum_{\alpha} \sum_{l\neq j,\gamma} \frac{\partial \dot{h}_{jl}^{\gamma\beta}}{\partial r_i^{\alpha}} (A_{ij}^{\alpha\gamma} - A_{il}^{\alpha\gamma}) + \sum_{l\neq j,\gamma} \dot{h}_{jl}^{\gamma\beta} (B_{ij}^{\gamma} - B_{il}^{\gamma}); \tag{4.32}$$

we note that

$$\frac{\partial \dot{h}_{jl}^{\gamma\beta}}{\partial r_i^{\alpha}} = \sum_{k,\nu} \frac{\partial \dot{h}_{jl}^{\gamma\beta}}{\partial x_k^{\nu}} \frac{\partial x_k^{\nu}}{\partial r_i^{\alpha}} = \sum_{k,\nu} \frac{\partial \dot{h}_{jl}^{\gamma\beta}}{\partial x_k^{\nu}} A_{ik}^{\alpha\nu} \tag{4.33}$$

so we need to compute the derivative $\frac{\partial \dot{h}_{jl}^{\gamma\beta}}{\partial x_k^{\nu}}$

$$\begin{aligned} \frac{\partial \dot{h}_{jl}^{\gamma\beta}}{\partial x_k^{\nu}} &= \frac{\partial}{\partial x_k^{\nu}} \left[\delta^{\gamma\beta}\eta^{(1)}(x_{jl}) + \frac{\eta'^{(1)}(x_{jl})}{x_{jl}} x_{jl}^{\gamma} x_{jl}^{\beta} \right] = \\ &= (\delta_{jk} - \delta_{lk}) \left[\delta^{\gamma\beta} \frac{x_{jl}^{\nu}}{x_{jl}} \eta'^{(1)}(x_{jl}) + \delta^{\nu\beta} \frac{x_{jl}^{\gamma}}{x_{jl}} \eta'^{(1)}(x_{jl}) + \delta^{\nu\gamma} \frac{x_{jl}^{\beta}}{x_{jl}} \eta'^{(1)}(x_{jl}) + \right. \\ &\quad \left. + \frac{x_{jl}^{\beta} x_{jl}^{\gamma} x_{jl}^{\nu}}{x_{jl}^2} \eta''^{(1)}(x_{jl}) - \frac{x_{jl}^{\beta} x_{jl}^{\gamma} x_{jl}^{\nu}}{x_{jl}^3} \eta'^{(1)}(x_{jl}) \right] = \\ &= (\delta_{jk} - \delta_{lk}) \left[\frac{\eta'^{(1)}(x_{jl})}{x_{jl}} \left(\delta^{\gamma\beta} x_{jl}^{\nu} + \delta^{\nu\beta} x_{jl}^{\gamma} + \delta^{\nu\gamma} x_{jl}^{\beta} \right) + \frac{x_{jl}^{\beta} x_{jl}^{\gamma} x_{jl}^{\nu}}{x_{jl}^2} \left(\eta''^{(1)}(x_{jl}) - \frac{\eta'^{(1)}(x_{jl})}{x_{jl}} \right) \right] \end{aligned} \tag{4.34}$$

and defining the quantity

$$\ddot{h}_{jl}^{\alpha\gamma\beta} = \frac{\eta'^{(1)}(x_{jl})}{x_{jl}} \left(\delta^{\gamma\beta} x_{jl}^{\nu} + \delta^{\nu\beta} x_{jl}^{\gamma} + \delta^{\nu\gamma} x_{jl}^{\beta} \right) + \frac{x_{jl}^{\beta} x_{jl}^{\gamma} x_{jl}^{\nu}}{x_{jl}^2} \left(\eta''^{(1)}(x_{jl}) - \frac{\eta'^{(1)}(x_{jl})}{x_{jl}} \right) \tag{4.35}$$

we can write

$$\frac{\partial \dot{h}_{jl}^{\gamma\beta}}{\partial x_k^\nu} = (\delta_{jk} - \delta_{lk})\ddot{h}_{jl}^{\alpha\gamma\beta}. \tag{4.36}$$

Using 4.36 and 4.33 in 4.32 we have

$$\begin{aligned} Z_{ij}^\beta &= B_{ij}^\beta + \sum_\alpha \sum_{l\neq j,\gamma} \sum_{k,\nu} (\delta_{jk} - \delta_{lk})\ddot{h}_{jl}^{\alpha\gamma\beta} A_{ik}^{\alpha\nu}(A_{ij}^{\alpha\gamma} - A_{il}^{\alpha\gamma}) + \sum_{l\neq j,\gamma} \dot{h}_{jl}^{\gamma\beta}(B_{ij}^\gamma - B_{il}^\gamma) = \\ &= B_{ij}^\beta + \sum_\alpha \sum_{l\neq j,\gamma\nu} \ddot{h}_{jl}^{\alpha\gamma\beta} \left[A_{ij}^{\alpha\nu} A_{ij}^{\alpha\gamma} + A_{il}^{\alpha\nu} A_{il}^{\alpha\gamma} - A_{ij}^{\alpha\nu} A_{il}^{\alpha\gamma} - A_{il}^{\alpha\nu} A_{ij}^{\alpha\gamma}\right] + \sum_{l\neq j,\gamma} \dot{h}_{jl}^{\gamma\beta}(B_{ij}^\gamma - B_{il}^\gamma). \end{aligned} \tag{4.37}$$

We can then define the quantity

$$C_{ijk}^{\alpha\beta} = \sum_\gamma A_{ij}^{\gamma\alpha} A_{ik}^{\gamma\beta} \tag{4.38}$$

so that 4.37 becomes

$$Z_{ij}^\beta = B_{ij}^\beta + \sum_{l\neq j,\gamma\nu} \ddot{h}_{jl}^{\alpha\gamma\beta} \left[C_{ijj}^{\nu\gamma} + C_{ill}^{\nu\gamma} - C_{ijl}^{\nu\gamma} - C_{ilj}^{\nu\gamma}\right] + \sum_{l\neq j,\gamma} \dot{h}_{jl}^{\gamma\beta}(B_{ij}^\gamma - B_{il}^\gamma). \tag{4.39}$$

We can now compute the part of the kinetic energy due to the determinant simply using the matrices Y, Z instead of the matrices A, B in 2.79

$$\nabla_i^\alpha \log(\det(\phi)) = \sum_\beta \sum_{jk} V_{jk} \phi_{kj}^\beta Y_{ij}^{\alpha\beta} = \sum_\beta \sum_j F_{jj}^\beta Y_{ij}^{\alpha\beta} \tag{4.40}$$

and 2.82

$$\Delta \log(\det(\phi)) = \sum_{\alpha ij} Z_{ij}^\alpha F_{jj}^\alpha - \sum_{\alpha\beta\gamma} \sum_{ijk} Y_{ij}^{\alpha\beta} Y_{ik}^{\alpha\gamma} \cdot \left(F_{kj}^\beta F_{jk}^\gamma - \delta_{jk} \sum_m V_{jm} \phi_{mj}^{\beta\gamma}\right). \tag{4.41}$$

These operations can again be done in order of N^3 computations. We observe that by definition the three body correlation term is the scalar product of two terms with analogue form of the backflow transformation; we can then simply use the derivatives for the backflow terms along the usual chain rule and the rule of the derivative of a product.

We have thus written the derivatives that we need to compute the local energy of $\Psi^{(2)}(\mathbf{R})$. This procedure can be generalized to functions with further backflow iterations. One has just to compute derivatives for all the pseudopotentials at each iteration using the chain rule

$$\frac{\partial x_j^{(n)\beta}}{\partial r_i^\alpha} = \sum_{k\gamma} \frac{\partial x_j^{(n)\beta}}{\partial x_k^{(n-1)\gamma}} \frac{\partial x_k^{(n-1)\gamma}}{\partial r_i^\alpha} \tag{4.42}$$

4.4 Zero-variance energy extrapolations

The quality of a wave function can be estimated using two quantities: the average value and the variance of the local energy. Lower energies imply a better approximation of the ground state because of the variational principle, while lower variances of the local energy imply better wave functions for the zero variance property. These quantities can be combined to obtain stringent upper and lower bounds to the exact energy by extrapolation to the limit of zero variance.

Here we assume that we are using "good" wave functions as trial wave functions, which means that the variational energy $E_T = \langle \Psi_T | H | \Psi_T \rangle$ is closer to exact ground state of the Hamiltonian E_0 than to any other energy eigenvalue

$$|E_T - E_0| < |E_T - E_i| \quad \text{for any } i > 0. \tag{4.43}$$

From the definition of the energy variance we have

$$\begin{aligned} \sigma^2 &= \langle \Psi_T | (H - E_T)^2 | \Psi_T \rangle = \sum_i \langle \Psi_T | (H - E_T) | \Phi_i \rangle \langle \Phi_i | (H - E_T) | \Psi_T \rangle = \\ &= \sum_i |c_i|^2 (E_T - E_i)^2 > \sum_i |c_i|^2 (E_T - E_0)^2 > (E_T - E_0)^2 \end{aligned} \tag{4.44}$$

where we decomposed $|\Psi_T\rangle$ on an energy eigenstates basis $\{|\Phi_i\rangle\}$ with $H|\Phi_i\rangle = E_i|\Phi_i\rangle$ and $c_i = \langle \Psi_T | \Phi_i \rangle$ with $\sum_i |c_i|^2 = 1$.

From this relation we see that the energy variance can be used to obtain a strict lower bound to exact ground state energy [92]

$$\sqrt{\sigma^2} > E_T - E_0 \quad \rightarrow \quad E_T - \sqrt{\sigma^2} < E_0. \tag{4.45}$$

The condition 4.43 can be somewhat relaxed in such a way that the lower bound 4.45 remains valid. This can be seen writing the quantities

$$\begin{aligned} C_T &= \sum_{i>0} |c_i|^2 \\ \Delta_T &= \sum_{i>0} \frac{|c_i|^2}{C_T} (E_i - E_0) \\ \overline{\Delta_T^2} &= \sum_{i>0} \frac{|c_i|^2}{C_T} (E_i - E_0)^2 \geq \Delta_T^2 \end{aligned} \tag{4.46}$$

decomposing again the trial wave function on a basis of energy eigenstates; using these quantities we can write the energy and the variance as

$$\begin{aligned} E_T &= \sum_i |c_i|^2 E_i = E_0 + \sum_{i>0} |c_i|^2 (E_i - E_0) = E_0 + C_T \Delta_T \\ \sigma^2 &= \sum_i |c_i|^2 (E_i - E_T)^2 = \sum_i |c_i|^2 (E_i - E_0 - C_T \Delta_T)^2 = \\ &= \sum_i |c_i|^2 (E_i - E_0)^2 + (C_T \Delta_T)^2 + 2 E_0 C_T \Delta_T - 2 E_T C_T \Delta_T = \\ &= \overline{\Delta_T^2} C_T - (\Delta_T C_T)^2 ; \end{aligned} \tag{4.47}$$

using this relations we have

$$E_T - \sqrt{\sigma^2} = E_0 + \Delta_T C_T - \sqrt{\overline{\Delta_T^2} C_T - (\Delta_T C_T)^2} = \\ = E_0 - \Delta_T C_T \left[\sqrt{\frac{\overline{\Delta_T^2}}{\Delta_T^2 C_T} - 1} - 1 \right]. \tag{4.48}$$

The lower bound 4.45 holds if

$$\Delta_T C_T \left[\sqrt{\frac{\overline{\Delta_T^2}}{\Delta_T^2 C_T} - 1} - 1 \right] > 0, \tag{4.49}$$

i.e. if

$$C_T \leq \overline{\Delta^2}_T / 2\Delta_T^2 \tag{4.50}$$

or

$$E_T - E_0 \leq \overline{\Delta^2}_T / 2\Delta_T. \tag{4.51}$$

The condition 4.51 is more useful than the condition 4.43. On one hand it is less stringent, on the other it can easily checked (see below). The condition 4.43 can in fact only be checked evaluating the energy gap between the ground state and the first excited state in a separate computation using the Transient Estimate technique [20].

We can also extrapolate the exact energy without having to use the lower bound 4.45, using a simple fit. In order to do so we must introduce an assumption: the trial wave function we are using has large overlap with the ground state, while components on the excited states are broadly, evenly distributed. Moreover we assume that improving the trial wave function, has the effect of increasing the overlap with the ground state and decrease uniformly the excited state contributions. If this happens $C_T \to 0$ while Δ_T and $\overline{\Delta^2}_T$ are roughly constant. We can thus neglect terms of order C_T^2 and higher in the variance in 4.47, so that

$$\sigma^2 \simeq \overline{\Delta_T^2} C_T \tag{4.52}$$

and substituting in the trial energy in 4.47 we obtain

$$E_T = E_0 + A\,\sigma^2, \tag{4.53}$$

with $A = \Delta_T / \overline{\Delta^2}_T$. We can use a fit for the local energy as a function of its variance to obtain another estimate for the exact ground state energy. Moreover we can use the linear term in this fit to check the condition for the lower bound that from 4.51 as 4.51 now becomes $E_T - E_0 \leq 1/2A$.

Both these extrapolations can provide estimates for the ground state energy using data obtained with Variational Monte Carlo simulations. We would like however to be able to use this extrapolations also with data obtained using the Diffusion-Fixed Node technique. The problem here is that the variance in Diffusion Monte Carlo simulations is strictly zero, as we are projecting the trial wave function on an energy eigenstate

(at least inside nodal pockets). One way to estimate the quality of the wave function in Diffusion data is using the variance obtained with the same trial wave function in Variational Monte Carlo runs. Using this variance we can gauge the accuracy of the trial wave function and perform the extrapolation 4.53, but as it isn't the real variance of the Diffusion Monte Carlo estimate we can't use it in the estimate of the lower bound.

These extrapolations are especially useful when combined with our wave functions: the iterative backflow procedure in fact provides a way to systematically improve the quality of the wave, leading to lower variances and energies as more backflow transformations are added. We can thus easily obtain several energies along with their variances and this allows us to fit our data to 4.45 or 4.53 obtain ground state estimates.

We remark that these extrapolations can provide exact estimates for both Bose and Fermi systems. The only limit here is that the wave function has to be sufficiently close to the exact ground state wave function.

4.5 Two dimensional ^{3}He at freezing

The first system we studied with our new wave functions was a two dimensional ^{3}He system at freezing. We made the decision of studying this system because because ^{3}He is the archetypical system of strongly interacting, strongly correlated Fermi liquid there are a large number of numerical studies on it, so that we have several well known results to benchmark our results.

We choose to study the system at freezing because backflow transformations have larger effects at higher densities [18], and so we should be able to better evaluate the effectiveness of our iterative procedure when dealing with a system at freezing.

In these simulations we started using Jastrow-Slater wave functions with plane waves, with two and three body correlations in the Jastrow. Then we included a standard backflow transformation and then we add more transformations, introducing two and three body correlations between particles at each order.

We studied an unpolarized system with $N = 26$ and $N = 58$ atoms, and a fully polarized system with $N = 29$ atoms, in a simulation box with periodic boundary conditions.

Tha Hamiltonian of this system is

$$H = \sum_i \frac{p_i^2}{2m_i} + \sum_{i<j} V(r_{ij}). \tag{4.54}$$

The interatomic interaction $V(r)$ is the Aziz potential [29] routinely used in simulations of helium.

We used Jastrow-Slater wave functions with iterated backflow transformations

$$\Psi^{(M)} = J^{(0)}(\mathbf{R}) \prod_{n=1}^{M-1} J^{(n)}(\mathbf{X}^{(n)}) D(\mathbf{X}^{(M)}). \tag{4.55}$$

The Jastrow factors have the form

$$J^{(n)}(\mathbf{X}^{(n)}) = \exp(-U^{(n)}(\mathbf{X}^{(n)})) = \exp(-U_2^{(n)}(\mathbf{X}^{(n)}) - U_3^{(n)}(\mathbf{X}^{(n)})) \tag{4.56}$$

with

$$U_2^{(n)}(\mathbf{X}^{(n)}) = \sum_{i \neq j} u^{(n)}(\mathbf{x}_{ij}^{(n)}), \tag{4.57}$$

$$U_3^{(n)}(\mathbf{X}^{(n)}) = \sum_i \mathbf{G}_i^{(n)}(\mathbf{X}^{(n)}) \cdot \mathbf{G}_i^{(n)}(\mathbf{X}^{(n)}) \tag{4.58}$$

where

$$\mathbf{G}_i^{(n)}(\mathbf{X}^{(n)}) = \sum_j (\mathbf{x}_i^{(n)} - \mathbf{x}_j^{(n)}) \xi^{(n)}(x_{ij}^{(n)}) \tag{4.59}$$

and

$$\mathbf{x}_i^{(n)} = \mathbf{x}_i^{(n-1)} + \sum_j (\mathbf{x}_i^{(n-1)} - \mathbf{x}_j^{(n-1)}) \eta^{(n-1)}(x_{ij}^{(n-1)}). \tag{4.60}$$

$D(\mathbf{X}^{(M)})$ is a product of Slater determinants, one for each spin specie, computed using the highest order backflow coordinates. The pseudopotentials $u^{(n)}$, $\xi^{(n)}$ and $\eta^{(n)}$ are optimized in a Variational Monte Carlo procedure. All the pseudopotentials used have the functional form described in 2.6.

Every time we add a backflow iteration we optimize the pseudopotentials using the correlated sampling technique. With each iteration the optimization procedure becomes more involved, as we have 17 variational parameters for each iteration. The computational cost of a single simulation scales as N^3, and even if adding iterations slows down the computation the scaling does not get worse.

We remark that each time an iteration is added all the pseudopotentials have to be reoptimized starting from the wave functions of the previous iteration; even the pseudopotential already present at former computations have to optimized, as we observed that the pseudopotentials at the same order can change in presence of an increased number of iterations. We show as an example the pseudopotentials depending on the real atomic coordinates in wave functions with different number of backflow iterations in figure 4.1.

We show in figure 4.2 the pseudopotentials in an optimized wave function with 4 backflow iterations. We can see that in the same wave functions pseudopotentials referring to different backflow coordinates are somewhat different. While the three body and backflow pseudupotential display mostly the same qualitative behaviour the two body pseudopotentials have significant differences; we observe that these pseudopotentials for the transformed coordinates can surprisingly become attractive. This iterative procedure anyway introduces correlations at all orders, and thus it is difficult to give a direct physical interpretation of the pseudopotentials.

The effect of an attractive two body pseudopotential is even less clear in the light of the pair correlation functions, evaluated for the ^{3}He atoms and for the auxiliary backflow particles; we see in fact that backflow particles of higher orders are systematically more localized than the real ^{3}He atoms; if this effect were due only to a two body psedupotential this pseudopotential should be much more repulsive even than

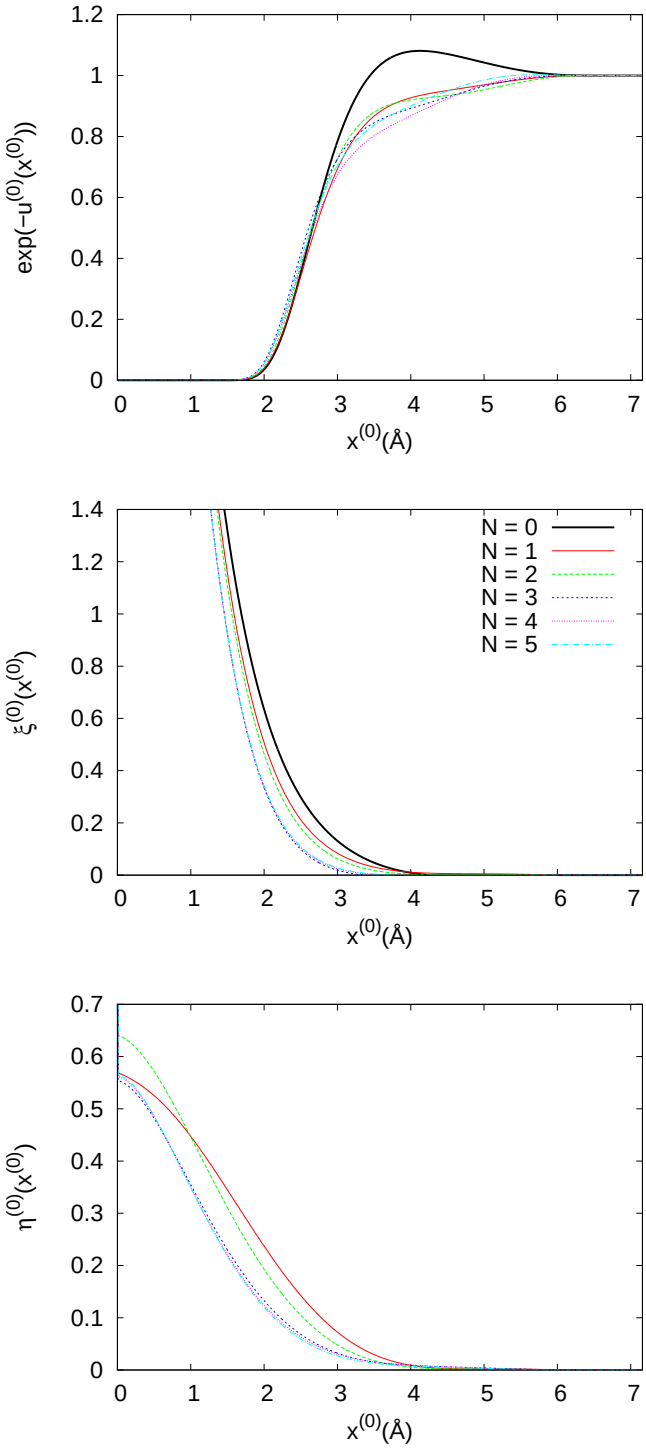

Figure 4.1: Pseudopotentials for two body correlations, three body correlations and backflow transformations for the real atomic coordinates in a two dimensional ^{3}He system with different a number of backflow iterations. The system is unpolarized and at freezing ($\rho = 0.060\text{Å}^{-2}$) and with $N = 26$ atoms.

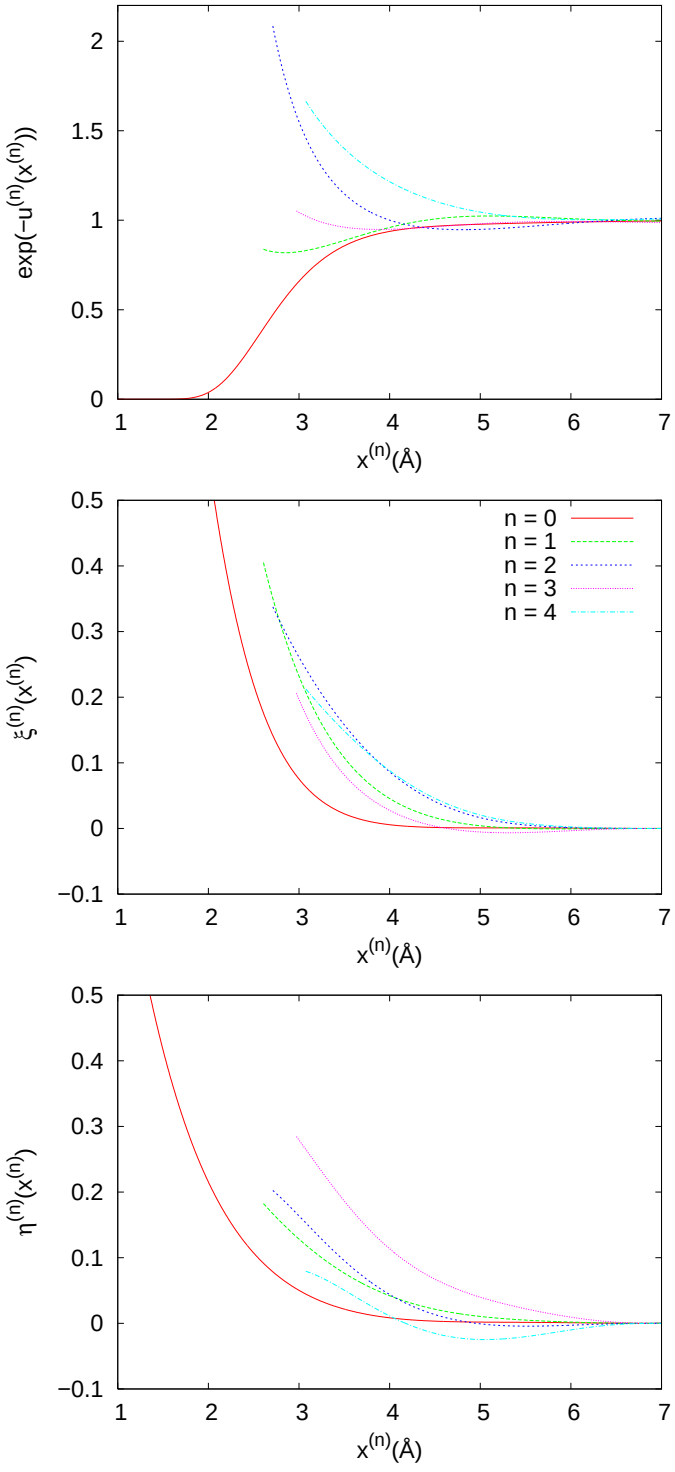

Figure 4.2: Optimized pseudopotentials of the trial function $\Psi_T^{(5)}$ for $N = 26$, $\zeta = 0$. The lines are broken where the pair distribution functions of the relevant (quasi)coordinates become negligibly small, $g(x^{(n)}) \lesssim 10^{-3}$ (see Fig. 4.3) The index 0 refers to pseudopotentials for the real atoms.

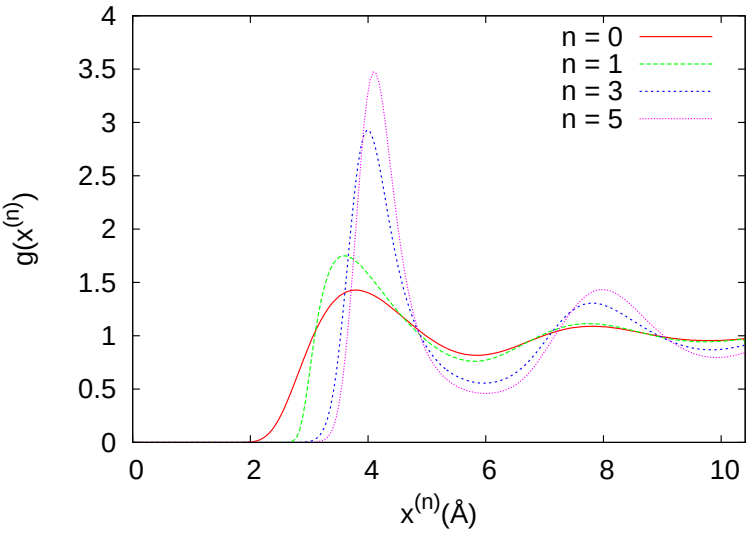

Figure 4.3: Pair correlation functions calculated in a VMC simulation with the $\Psi^{(5)}(\mathbf{R})$ trial function, using the atomic coordinates $\mathbf{X}^{(0)} = \mathbf{R}$ (solid line), and the backflow coordinates $\mathbf{X}^{(1)}$, $\mathbf{X}^{(3)}$, and $\mathbf{X}^{(5)}$ (dotted, dash-dotted and dashed lines, respectively).

the one of the helium atoms (seen in figure 4.1). The localization of the backflow particles reminds a similar effect observed in the pair correlation functions of shadow particles, auxiliary particles introduced using Shadow Wave Functions [96], and suggests the intriguing possibility that at higher densities the backflow particles could even crystallize.

We show in figure 4.1 the Variational and Diffusion Monte Carlo data that we obtained. Including one backflow transformation as in the usual backflow wave function leads to a significant improvement of the variational estimates with respect to Jastrow-Slater wave function with plane waves. We can see however that there is still a significant excess energy with respect to the exact results obtained with the Transient Estimate, when available. This excess can be reduced using the iterative backflow procedure, both in the VMC computations, where the excess energy in the unpolarized system is decreasing from 0.3 K to less than 0.1 K, and in the DMC computations (form about 0.05 K to about 0.015 K), and we can observe that the energy discrepancy is reduced to about a third. In the polarized system the existing results are more accurate, but the iterative procedure still allows to reduce the difference with the Transient Estimate result.

In order to reduce the computational effort of the optimization procedure we wondered if it was possible to use some simpler iteration schemes, trying to decrease the computational effort and at the same time not to lose too much accuracy. We tried to use wave functions without correlation between backflow particles, i. e. given by the product of just one Jastrow term for the correlations of the helium atoms and a Slater determinant of auxiliary coordinates obtained iterating backflow transformations; we

also used a procedure in which the only pseudopotentials to be optimized are the newly added ones, so that lower order pseudopotentials are left unchanged from the previous iterations. From the results in table 4.2 we see that not explicitly including correlations for backflow coordinates (data set I) leads to significantly higher energies in the VMC estimates, of about 0.2 K at each order. Moreover even if the variational estimate has an improvement of more that 10^{-2} K going from $\Psi^{(2)}$ to $\Psi^{(3)}$ further iterations leads to smaller energy gains, of the order of the mK. The VMC results are somewhat better using wave functions in which only the highest order pseudopotentials are optimized (II), but the variational estimates are still above the results with the fully optimized wave functions of several hundredths of K. DMC energies are better but still higher of some mK with respect to the data shown in table 4.1. Such energies differences can be significant for example when studying the energy as a function of polarization of ^{3}He, in which accuracy of the order of mK is required.

On the other hand we also tried more accurate wave functions, using different backflow transformations for parallel and antiparallel spins. The energy is somewhat lower in the Variational estimates, but the energy gain becomes negligible in the Diffusion Monte Carlo data. We show in table 4.2 the energies obtained with these modified wave functions.

The results of the zero variance extrapolations discussed in section 4.4 are shown in Figs (4.4), (4.5) and (4.6) and listed in Table 4.1. We observe that with our data both the conditions 4.43 and 4.51 for the lower bound extrapolations hold, as can be seen from the the value of the energy gap between the ground state and the first excited state (computed using Transient Estimate) and of $1/2A$, obtained from the data fit. Both quantities are larger when considering the fully polarized system; this is not surprising, as the energy of $\Psi^{(0)}$ and $\Psi^{(1)}$ were already closer to the exact result. Since these conditions both hold we expect that both the zero variance extrapolations should give good results. This is in fact the case. The extrapolation of the VMC data, both for the energy and its lower bound, give results that are within few tens of mK of the exact result. While the extrapolation of the DMC energies is less formally sound it still can give a very accurate result, consistent with the Transient Estimate (the difference between the extrapolated and transient estimate energy is basically the sum of the error bars of both data). Even when the Transient Estimate is not available, as is the case for the larger system, we can see that the extrapolations of the energy and the lower bound from VMC data leads to an uncertainty on the exact ground state energy of about 60mK, and that the extrapolation of the DMC falls inside this interval.

We conclude observing that the zone in which it is possible to obtain the lower bound 4.51 shrinks when we increase the size of the system, and eventually it vanishes in the thermodynamic limit [92]. This means that extrapolating a lower bound for the exact ground state energy may not be possible for large systems. On the other hand this region is still large enough to perform computations for systems whose size forbids exact evaluation of the energy, such as the system with 58 atoms we considered.

	N=26, $\zeta = 0$			
	E_{VMC}/N	σ^2/N	Δ	E_{DMC}/N
$\Psi^{(0)}$	3.011(1)	28.29		2.419(2)
$\Psi^{(1)}$	2.688(1)	13.05	0.323	2.353(2)
$\Psi^{(2)}$	2.471(1)	4.58	0.540	2.336(2)
$\Psi^{(3)}$	2.4258(8)	2.86	0.585	2.3284(9)
$\Psi^{(4)}$	2.4049(9)	2.47	0.606	2.3223(4)
$\Psi^{(5)}$	2.400(1)	2.29	0.611	2.323(1)
VMC_{ext}	2.338(5)			
DMC_{ext}	2.317(3)			
LB_{ext}	2.275(14)			
TE	2.307(7)			
	N=58, $\zeta = 0$			
	E_{VMC}/N	σ^2/N	Δ	E_{DMC}/N
$\Psi^{(0)}$	2.900(1)	28.07		2.373(2)
$\Psi^{(1)}$	2.584(1)	13.34	0.316	2.283(2)
$\Psi^{(2)}$	2.356(2)	4.93	0.544	
$\Psi^{(3)}$	2.313(2)	3.25	0.587	
$\Psi^{(4)}$	2.297(2)	2.67	0.603	
$\Psi^{(5)}$	2.292(1)	2.49	0.608	2.232(1)
VMC_{ext}	2.217(2)			
DMC_{ext}	2.216(3)			
LB_{ext}	2.149(12)			
TE				
	N=29, $\zeta = 1$			
	E_{VMC}/N	σ^2/N	Δ	E_{DMC}/N
$\Psi^{(0)}$	2.5831(6)	7.51		2.402(1)
$\Psi^{(1)}$	2.5133(5)	5.34	0.070	2.4005(6)
$\Psi^{(2)}$	2.4383(3)	2.20	0.145	2.3918(5)
$\Psi^{(3)}$	2.4193(3)	1.54	0.164	2.3877(4)
$\Psi^{(4)}$	2.4136(2)	1.36	0.170	2.387(1)
$\Psi^{(5)}$	2.4109(7)	1.25	0.173	2.3869(5)
VMC_{ext}	2.384(6)			
DMC_{ext}	2.379(1)			
LB_{ext}	2.390(26)			
TE	2.375(3)			

Table 4.1: Ground-state energy per particle, in K, of liquid ^{3}He in two dimensions at $\rho = 0.060\text{Å}^{-2}$, obtained with VMC ($E_{VMC}/N$) and FN-DMC ($E_{DMC}/N$) using different trial wave functions: without backflow ($\Psi^{(0)}$) and with M-times iterated backflow ($\Psi^{(M)}$). ζ is the spin polarization and N is the number of particles. Δ is the gain in VMC energy per particle relative to the PW value, and σ^2 is the variance of the VMC energy. TE are exact results calculated with the transient estimate method [19]. VMC_{ext}, DMC_{ext} and LB_{ext} are the extrapolations to zero variance of E_{VMC}/N, E_{DMC}/N and of the lower bound 4.45 respectively. Statistical uncertainties on the last digit(s) are given in parentheses.

	$N = 26, \zeta = 0$							
	E_T/N				E_{DMC}/N			
	0	I	II	III	0	I	II	III
$\Psi^{(0)}$								
$\Psi^{(1)}$								
$\Psi^{(2)}$	2.471(1)	2.599(2)	2.515(1)	2.461(1)	2.336(2)	2.337(2)	2.337(2)	
$\Psi^{(3)}$	2.4258(8)	2.585(2)	2.480(1)	2.413(1)	2.3284(9)	2.335(2)	2.332(1)	2.3256(9)
$\Psi^{(4)}$	2.4049(9)	2.584(2)	2.472(1)	2.398(1)	2.3223(4)	2.335(2)	2.326(1)	2.3215(4)
$\Psi^{(5)}$	2.400(1)	2.580(2)	2.470(1)	2.390(2)	2.323(1)	2.331(1)	2.325(3)	2.324(1)

Table 4.2: Some of the energies of Table 4.1 compared to the corresponding values obtained with downgraded or upgraded wave functions. Entries 0: energies from Table 4.1; entries I: downgraded wave functions with omitted Jastrow factors of the quasi-coordinates; entries II: downgraded wave functions with Jastrow and backflow potentials from previous iterations not repotimized; entries III: upgraded wave functions with different backflow potentials for atoms/backflow particles with parallel and antiparallel spins.

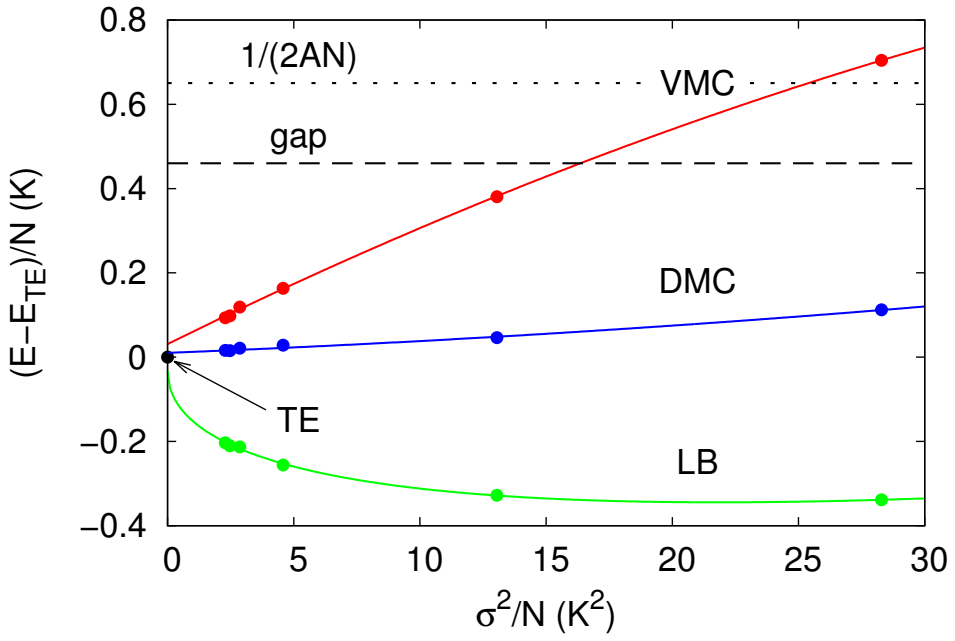

Figure 4.4: VMC and DMC energies for $N = 26$, $\zeta = 0$. The points refer to wave functions with plane waves and then with increasing numbers of backflow transformations. We also show the lower bound for the exact ground state energy. We took as the energy reference a the result of a Transient Estimate computation. All the energy extrapolations are very close to the exact result. We also show the energy of the first excited state and the quantity $1/2A$ to check the validity of the assumptions underlying the lower bound.

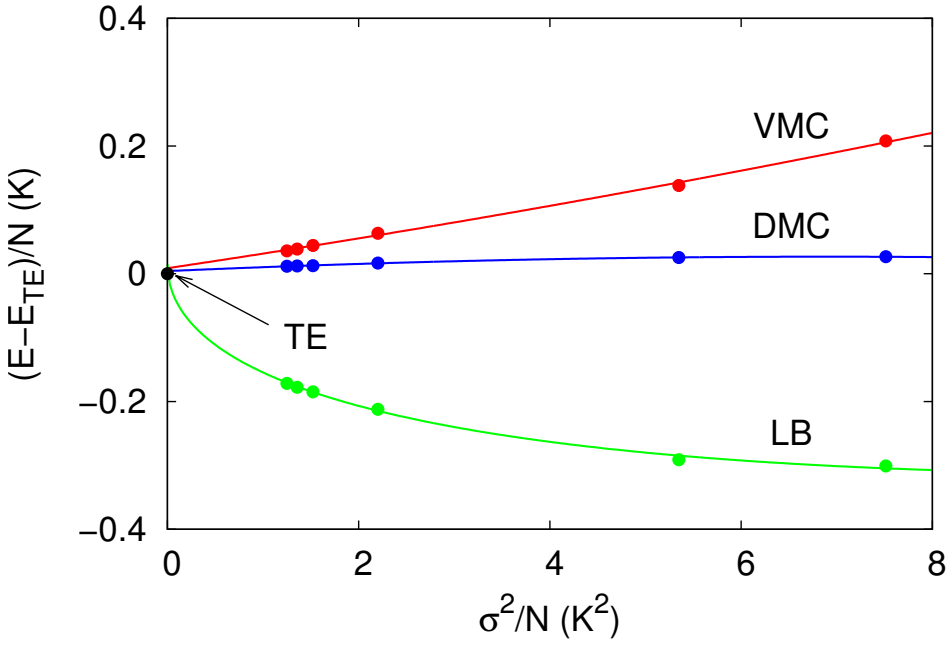

Figure 4.5: VMC and DMC energies for $N = 29$, $\zeta = 1$. The data are the same as in figure 4.4. Here the first excited state (about 0.6 K) and $1/2A$ (0.772 K) are off scale.

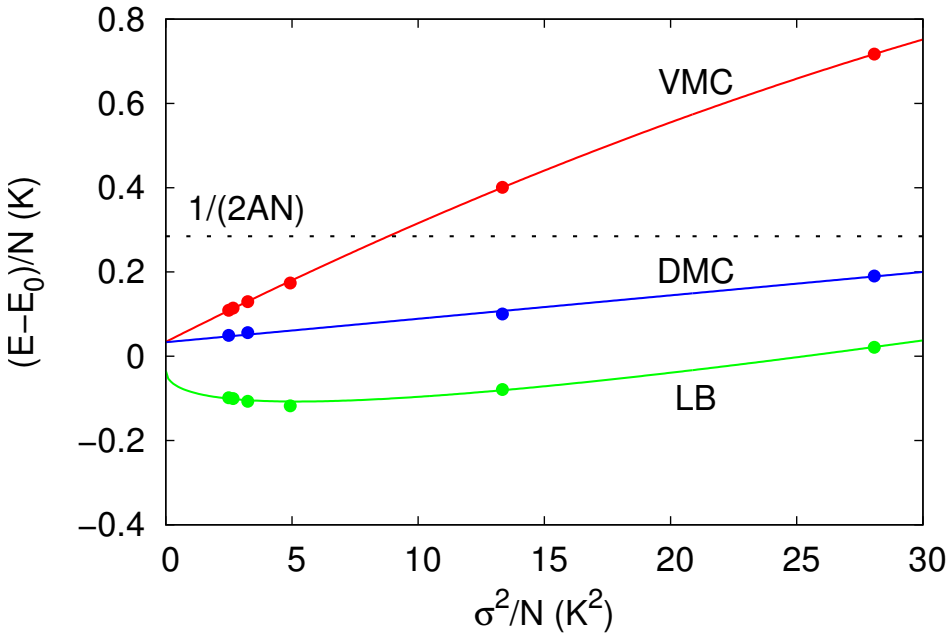

Figure 4.6: VMC and DMC energies for $N = 58$, $\zeta = 0$. The data are the same as in figure 4.4. Here Transient Estimate results were not available, so we don't have estimates for the exact ground state energy and for the gap between the ground state and the first excited state; we used as a reference for the energy the average between the VMC and the lower bound extrapolations.

4.6 Three dimensional ^{4}He

We have seen however that backflow transformations can be iterated, and they also affect the interparticle correlations in the Jastrow term. The improvement of the description of the interparticle interactions is significant, and it does not imply a large increase of the computational cost. It is worth to investigate other applications aside from ^{3}He, such as Bose systems of other Fermi systems such as the electron gas or electrons in atoms, molecules or solids. Here we show results of the use of our iterative backflow procedure in the simulation of a Bose system, three dimensional liquid ^{4}He.

^{4}He is a system that has been extensively studied with Quantum Monte Carlo simulations for a long time [10, 4, 94, 96]. As ^{4}He is a Bose particle, ^{4}He systems must be described by a wave function that is symmetric under particle exchange. We note that if we drop the Slater determinant part in the wave functions 4.55 we used for ^{3}He the resulting wave function is fully symmetric, and thus suitable to describe a Bose system. When dealing with Bose systems we are using a slightly different notation in the definition of the wave functions: here $\Psi^{(0)}(\mathbf{R})$ is a Jastrow wave function, while in the function $\Psi^{(M)}$ we use M backflow transformations and include M additional Jastrow terms

$$\Psi^{(M)}(\mathbf{R}) = \prod_{m=0}^{M} J^{(m)}(\mathbf{X}^{(m)}). \tag{4.61}$$

The fact that ^{4}He is a boson means that exact results, obtained with Diffusion or Path Integral Ground State Monte Carlo, are available [94]. We study this system with variational simulations to assess the quality of our wave functions and to estimate the accuracy of the zero variance extrapolations.

In addition it is interesting to compare the performance of our wave functions with other classes of wave functions, in particular with Shadow Wave Functions [93, 94, 95, 96]. Shadow Wave Functions are a class of wave functions that are widely used in the study of ^{4}He and are considered very good, especially at higher densities. It is very interesting to see if the better description of interparticle correlations due to an increased number of backflow transformations is enough to achieve a better accuracy.

While backflow transformations were introduced to study a Bose system, in QMC simulations they are mostly used for the study of Fermi systems. The reason is that backflow transformations do not have significant effects on the only single particle orbital that is occupied in a Bosonic ground state. To our knowledge this is the first time backflow transformations are used to describe a Bose system in the ground state.

The Hamiltonian of this system is the same as in 4.54, the only difference being the atomic mass. We decided to study a three dimensional system with $N = 64$ atoms at three different densities: 0.0196 Å^{-3}, 0.0218 Å^{-3} (equilibrium density) and 0.0262 Å^{-3} (freezing). Along with the energies we studied the radial pair correlation function $g(r)$ and the one body density matrix $n(r)$, and compare our results with exact data. Some wave functions give better variational estimates for the energy, while the results for other quantities are less accurate: having a good comparison with exact data for more physical quantities would be a very strong evidence of the overall accuracy of the wave functions.

As with the Fermi system we started using Jastrow wave functions with two and three body correlation and then we added one backflow transformation at a time, optimizing the wave function at each step. Instead of using correlated sampling here we used another optimization technique the linear optimization procedure [50]. We used the linear procedure as it is more efficient than correlated sampling when we have to optimize a large number of variational parameters. We show optimized pseudopotentials for a bosonic wave function at equilibrium density with five backflow transformations in figure 4.7. We can see that pseudopotential change when they refer to different orders of backflow coordinates; again we see that the two body term is purely repulsive for the real atoms and then it can be attractive for backflow particles. Changes are mostly quantitative in the three body and the backflow pseudopotential, with the partial exception of $\zeta^{(1)}(x^{(1)})$, that becomes negative at intermediate distances. Again the effect of the behaviour of the physical system is not immediately evident from the pseudopotentials. It is interesting to observe the radial correlation functions, both for the real atoms and the backflow coordinates; we show pair correlation functions for the helium atoms and the backflow particles at equilibrium density in figure 4.8. We see that as in the fermionic two dimensional case backflow particles of higher order are more localized. We note anyway that the peaks of the pair correlation function are less defined than for ^{3}He in two dimensions; we note that the Fermi systems was at freezing density while the Bose system considered here is at equilibrium. The sharpest peaks may suggest near freezing a crystallization of the backflow particles that arises before the formation of the real, physical solidification. We also note an interesting parallel with the behaviour of Shadow Wave Functions [95], that show more localized pair correlation functions for the shadow particle than the real atoms. This suggests that our wave functions may provide a stable ordered phase at high density, a feature that is at the moment unique of Shadow Wave Functions [97].

The variational estimates of the energy, along with the exact DMC data and estimates obtained using Shadow Wave Functions [96] are shown in table 4.3. At all densities including backflow transformations significantly lowers the energy. This effect is more important at higher densities: the energy improvement we observed went from about 0.13 K at the lowest density we considered (0.0196 Å^{-3}) to almost 0.5 K at freezing. Including correlations between the backflow coordinates we obtain energies that are lower than the Shadow Wave Function results [96]. Iterating the backflow procedure improves the energies even more; the energy gain obtained with every new iteration is lower and lower when the total number of backflow transformations increases. At the lowest density the energy difference between the energy of the trial wave functions with $M = 1$ and $M = 2$ transformations is of the order of 0.01K; the energy difference between the same wave functions at equilibrium was about three times larger, and five times larger at freezing. It is evident that the effect of the backflow transformation is especially important at high density. In our computations we used wave functions with up to two backflow transformations for the lowest density, five for the equilibrium and 3 for freezing. We decided to stop at two and three iterations for the lowest and highest density respectively because we did not observe significant energy gains when we added the last iteration; we went on up to five iterations for the

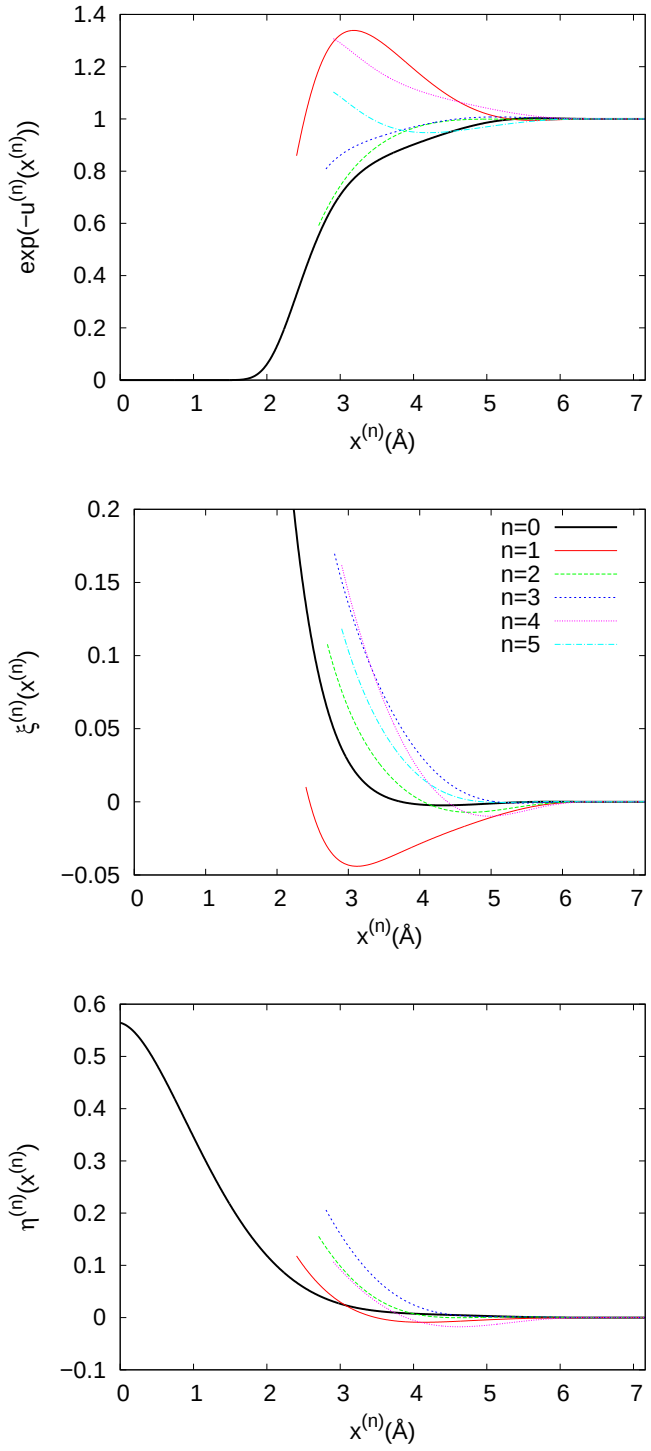

Figure 4.7: Optimized pseudopotentials of the trial function $\Psi_T^{(5)}$ for $N = 64$, $\rho = 0.0218$ Å^{-3}. The lines are broken where the pair distribution functions of the relevant (quasi)coordinates become negligibly small, $g(x^{(n)}) \lesssim 10^{-3}$. The index 0 refers to pseudopotentials for the real atoms.

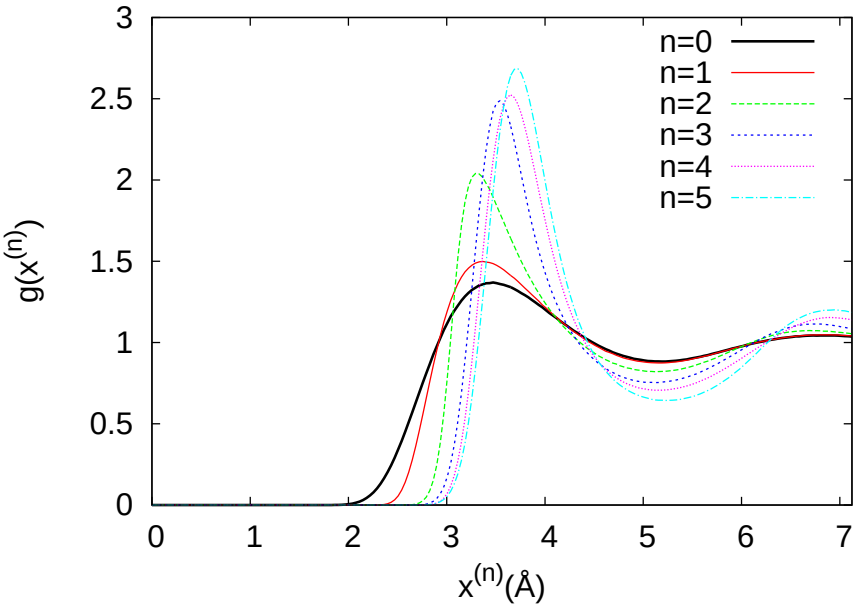

Figure 4.8: radial correlation functions for the atoms and the backflow coordinates, for a system of $N = 64$ ^{4}He at equilibrium ($\rho = 0.0218$ Å^{-3}). $g(x^{(0)}) = g(r)$ is the pair correlation function of the real atoms.

equilibrium as we were interested to study the effect of the iterative backflow procedure on other observables, and the shape of the optimized pseudopotentials. We show the equation of state we obtained in figure 4.9, and the energy difference between the variational and exact (DMC) energies in figure 4.10.

As in the Fermi system we performed extrapolations for the energy as a function of its variance and for the lower bound. We show our data in table 4.3. A bosonic superfluid has a large energy gap between the ground state and the first excited state, and thus we expect that the interval of validity for the energy and lower bound extrapolations will be larger than in the Fermi system. We show the extrapolations for the equilibrium density in figure 4.11. We can see that we have good agreement with the DMC data, especially at the equilibrium density where more points are available, and the energy discrepancy is at most of a few 10^{-2}K. We estimate the gap between the ground state and the first excited state to be of about 1 K. We obtained this estimate fitting the decaying of the energy from the variational energy to the exact ground state energy during a DMC simulation

$$\langle \Psi_G(\mathbf{R})|H|\exp(-\tau(H-E_T))\Psi_G(\mathbf{R})\rangle \simeq E_0 + \alpha \exp\left[-(E_1-E_0)\tau\right]. \tag{4.62}$$

The estimate for the gap and the values of the quantity $1/2A$ are larger than in the Fermi system, and lie outside figure 4.11, confirming the scarcity of low energy excitations for a Bose superfluid. We also note that with such a large gap we can expect to obtain good results from the extrapolations, as the condition for the upper and lower bounds are easily satisfied.

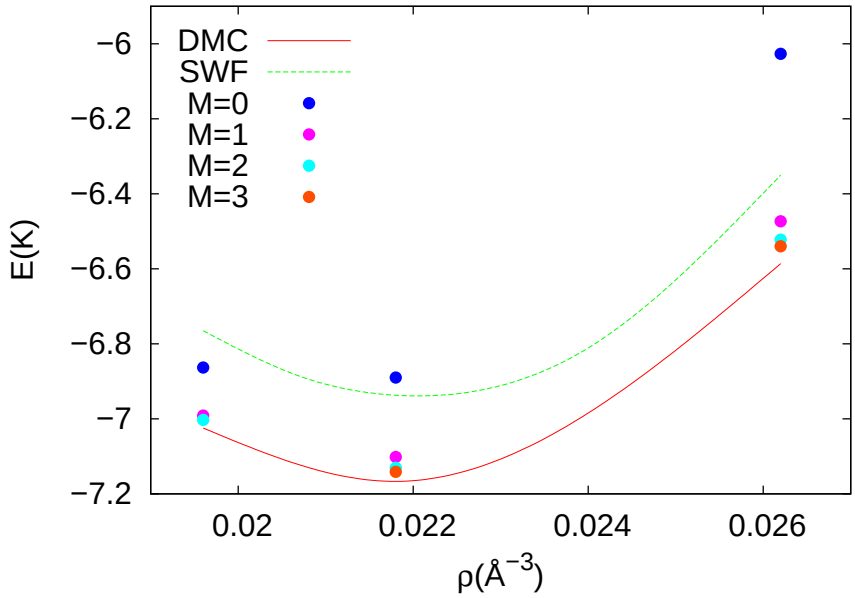

Figure 4.9: Equation of state for a three dimensional system of ^{4}He; Variational data are obtained using Shadow Wave Functions (SWF) and wave functions $\Psi^{(M)}(\mathbf{R})$ with several backflow transformations ($M = 0, ..., 3$); Diffusion Monte Carlo and Shadow Wave Function results are from [96].

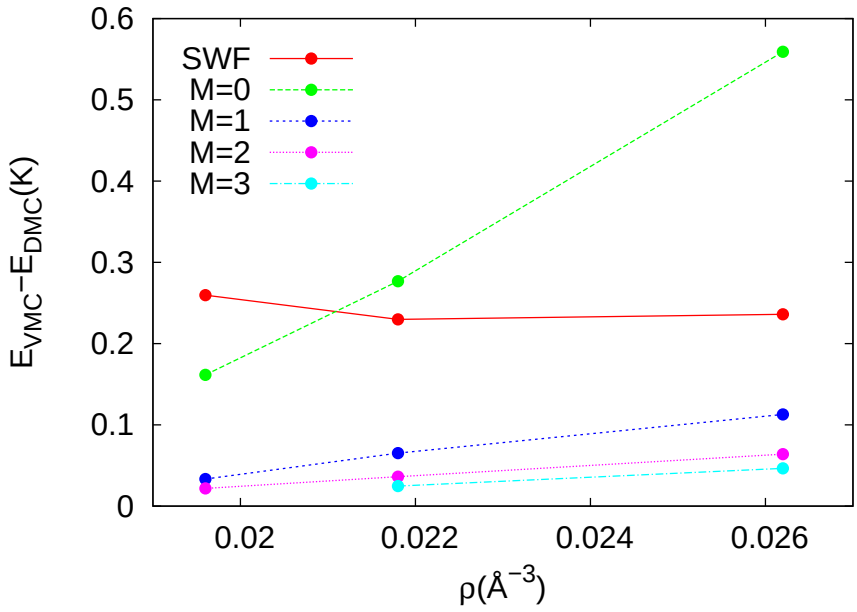

Figure 4.10: Energy difference between VMC and DMC ground state energies of liquid ^{4}He in three dimensions at three densities. VMC data are obtained using Shadow Wave Functions and our iterative backflow procedure with up to three backflow transformations (two for the lowest density).

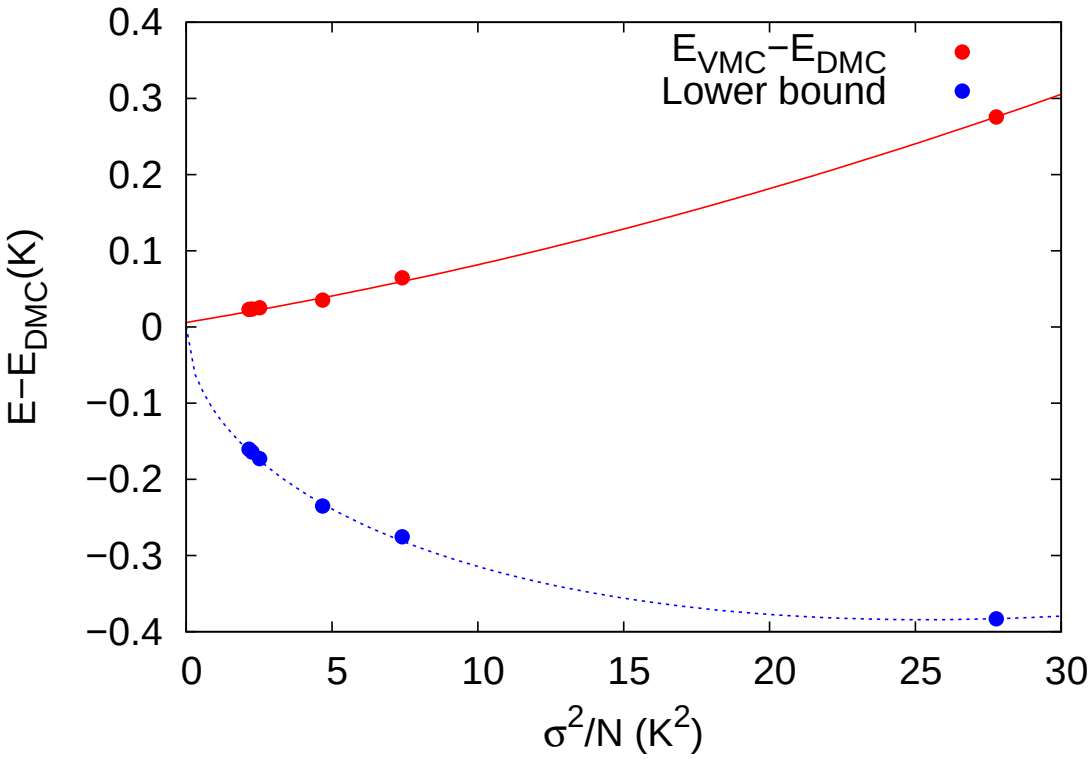

Figure 4.11: Energy per atom as a function of the variance per atom and lower bound for the ground state energy in liquid ^{4}He system in three dimensions at equilibrium density ($\rho = 0.0218$ Å^{-3}). We perform fits to extrapolate the exact ground state energy. The extrapolated energy agrees well with the DMC energy.

	$\rho = 0.0196$ Å^{-3}			
	E_{VMC}/N	σ^2/N	E_{SWF}/N	E_{DMC}/N
$\Psi^{(0)}$	-6.8631(3)	14.1363		
$\Psi^{(1)}$	-6.9913(1)	3.5677	-6.765(8)	-7.0246(1)
$\Psi^{(2)}$	-7.0027(2)	2.3468		
Ext.	-7.033(2)			
L.B.	-7.109(16)			
	$\rho = 0.0218$ Å^{-3}			
	E_{VMC}/N	σ^2/N	E_{SWF}/N	E_{DMC}/N
$\Psi^{(0)}$	-6.8911(3)	27.7709		
$\Psi^{(1)}$	-7.1016(8)	7.4108		
$\Psi^{(2)}$	-7.1314(5)	4.6977		
$\Psi^{(3)}$	-7.1415(4)	2.5141	-6.937(6)	-7.1661(5)
$\Psi^{(4)}$	-7.1438(4)	2.1541		
$\Psi^{(5)}$	-7.1432(5)	2.2564		
Ext.	-7.161(6)			
L.B.	-7.166(12)			
	$\rho = 0.0262$ Å^{-3}			
	E_{VMC}/N	σ^2/N	E_{SWF}/N	E_{DMC}/N
$\Psi^{(0)}$	-6.0268(5)	58.0268		
$\Psi^{(1)}$	-6.4731(3)	13.8264		
$\Psi^{(2)}$	-6.5221(3)	9.2970	-6.350(6)	-6.5860(11)
$\Psi^{(3)}$	-6.5395(8)	6.0700		
Ext.	-6.613(4)			
L.B.	-6.662(7)			

Table 4.3: Ground state energy per particle, in K, of liquid ^{4}He in three dimensions at different densities, obtained with Variational Monte Carlo (E_{VMC}/N,E_{SWF}/N) and Diffusion Monte Carlo (E_{DMC}/N) using different types of trial wave functions: Jastrow wave function without backflow (J), with n iterated backflow transformations (BF$^{(n)}$) and Shadow Wave Functions [96]. We also report the result of the zero variance energy extrapolation. Statistical uncertainties on the last digit(s) are given in parentheses.

In order to estimate the accuracy of our wave function we used them to evaluate the pair correlation function and the one body density matrix. For both these quantities we focused on the equilibrium density, $\rho = 0.0218$ Å^{-3}, and we included up to 5 backflow transformations in the wave functions.

We compare the pair correlation function for the real atoms obtained variationally with different number of backflow transformations with exact data obtained via Diffusion Monte Carlo in figure 4.12. We see that including backflow terms in the wave functions significantly improves the agreement between the Variational and Diffusion Monte Carlo data. This is especially evident in the enlargement of the radial correlation function, in which we can see that the correlations function for the backflow wave function basically overlaps with the exact data.

Finally we present results for the radial one body density matrix $n(r)$. We note that the obtaining a good estimate of the one body density matrix with VMC simulations is not trivial: when optimizing the wave functions to minimize the energy it is possible to obtain density matrices (and in particular condensate fractions) that are in poor agreement with exact data [94, 95]. It is interesting to check if our wave functions can lead to good density matrices along with low variational energies.

The density matrix is defined as

$$n(\mathbf{r}) = \frac{\int d\mathbf{R}\Psi_T^*(\mathbf{r}_1 + \mathbf{r}, \mathbf{r}_2, ..., \mathbf{r}_N)\Psi_T(\mathbf{r}_1, \mathbf{r}_2, ..., \mathbf{r}_N)}{\int d\mathbf{R}|\Psi_T(\mathbf{r}_1, \mathbf{r}_2, ..., \mathbf{r}_N)|^2} \tag{4.63}$$

and its angular average is the radial density matrix. The density matrix can be easily and efficiently computed in Variational Monte Carlo simulations [10, 49]. The radial density matrix can in fact written as

$$n(|\mathbf{r}' - \mathbf{r}|) = \left\langle \frac{\Psi_T(\mathbf{r}_1, ..., \mathbf{r}', ..., \mathbf{r}_N)}{\Psi_T(\mathbf{r}_1, ..., \mathbf{r}, ..., \mathbf{r}_N)} \right\rangle. \tag{4.64}$$

In practice this means that at each Monte Carlo step a random point $\mathbf{r}'$ is taken in the simulation box and we compute the ratios in 4.64 substituting each time the coordinate of a single atom with $\mathbf{r}$; these ratios are put in a histogram, whose average is an estimate of the actual density matrix.We show in figure 4.13 the results for the radial one body density matrix for the system at equilibrium. We show the matrices obtained with a wave function without any backflow term, a wave function with 5 backflow iterations and exact data obtained with the Path Integral Ground State (PIGS) technique [98]. We see that the agreement with PIGS data here is quite good even without including the backflow transformations; adding more and more transformations does not decrease this agreement and on the opposite slightly improves the accuracy of the computed density matrix. We can thus say that our wave functions are able to give good estimates for the radial one body density matrix, especially given the difficulty of obtaining accurate estimate of the one body density matrix with VMC simulations.

We have seen that adding just one backflow transformation to Jastrow wave functions significantly improves the agreement with exact data, both for the pair correlation function and for the one body density matrix; more iterations don't seem to have a big effect; it is worth noting that this holds just for the equilibrium density; it is very well

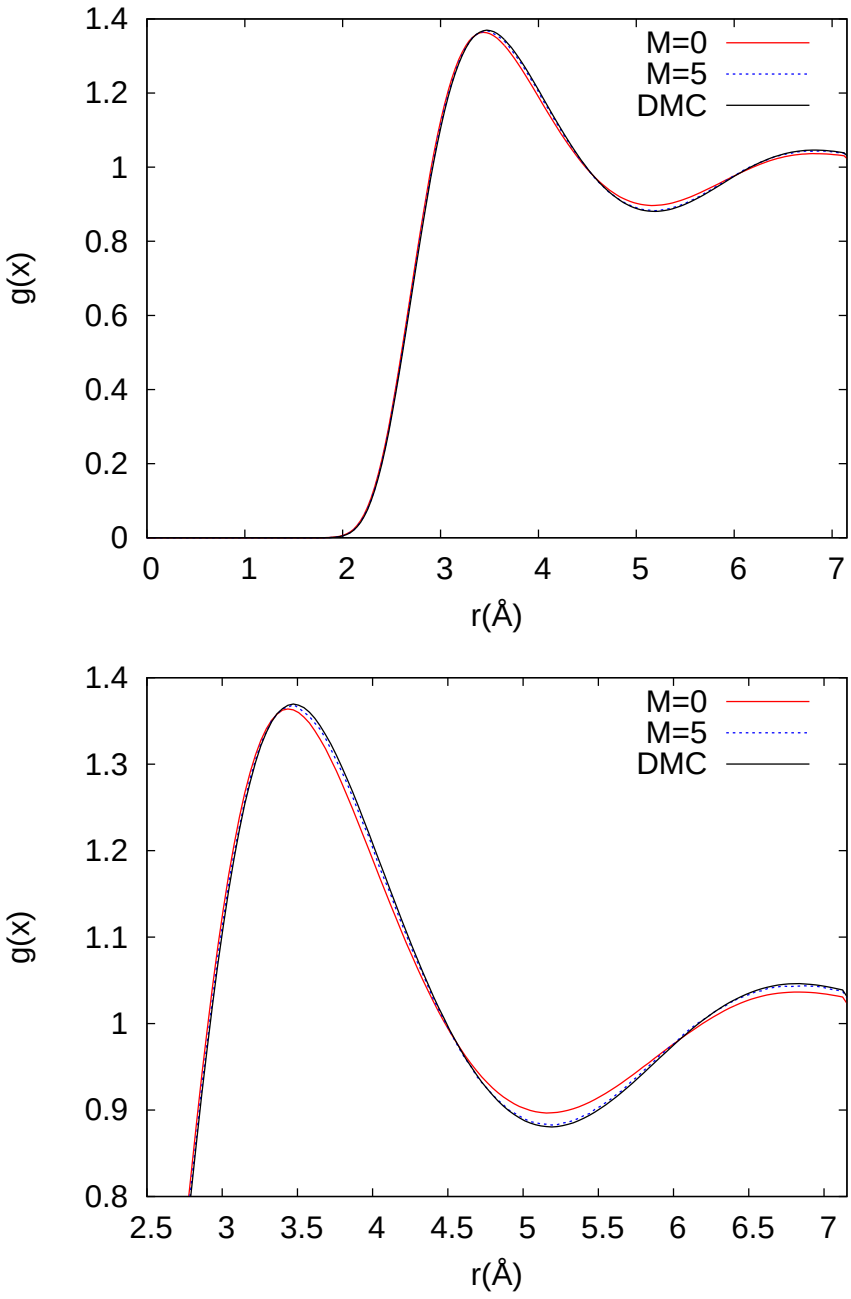

Figure 4.12: Comparison between pair correlation functions obtained with Variational Monte Carlo simulations with wave functions with no backflow transformations and with five backflow transformations with exact result obtained with Diffusion Monte Carlo. The simulations were performed with system of $N = 64$ atoms at a density of $\rho = 0.0218$ Å^{-3}.

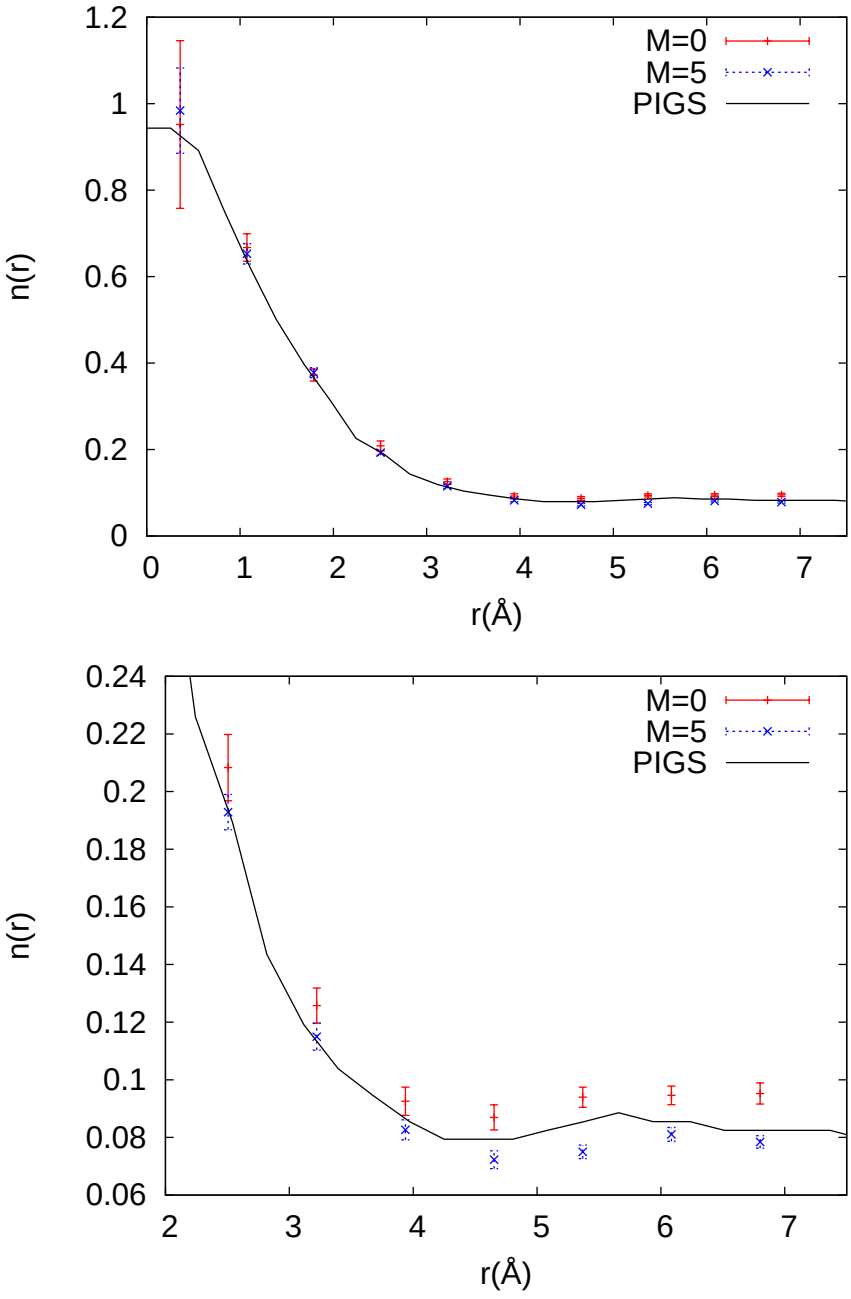

Figure 4.13: One body density matrix obtained with Variational Monte Carlo simulation of a system of $N = 64$ ^{4}He atoms using a Jastrow wave function without backflow transformation (red) and using five backflow transformations (blue); the results are compared with an exact PIGS estimate [98] (black line).

possible that at higher densities the effect of additional backflow transformation could be more evident.

The wave functions with iterated backflow gave remarkably good results in variational simulation of ^{4}He; in particular we see that adding even one backflow transformation dramatically improves the result, both for the energy and for other properties, i.e. the pair correlation function and the one body density matrix. Adding more iterations has the effect of lowering the variational energy even more. Studying ^{4}He allowed us to compare the performance of our new wave functions with Shadow Wave Functions, a class of trial wave function that describes with great success Bose liquids; we have seen that the iterative backflow wave functions can give even better results. This success suggests a wide versatility of the iterated backflow transformations, that can find applications outside the study of normal Fermi liquids: aside Bose systems they could also be included in the study for example of electrons, both as the homogeneous electron gas but also in the case of atoms, molecules or solids.

Conclusions

In this thesis we have shown the results of Quantum Monte Carlo simulations of systems of ^{3}He, in a two dimensional of quasi two dimensional environment. Our aim was to study the behaviour of quasi two dimensional ^{3}He at low density, and to design a new class of wave functions to describe strongly correlated systems.

We have confirmed that in a strictly two dimensional environment ^{3}He is a homogeneous fluid, but we have seen that the situations changes when we consider a system adsorbed on a substrate. The zero point motion in the transverse direction, that leads to an effective softening of the hard core repulsion between atoms, and the corrugation of the substrate may lead to the stabilization of a liquid phase.

^{3}He adsorbed on weak substrate can condense in a liquid phase, and in presence of corrugation a coexistence of different fluid phase is possible even on very attractive substrates, such as graphite. In agreement with the observation of Fukuyama we observe a remarkably similar behaviour on the first and second layer of ^{3}He adsorbed on graphite. We argue however that this is a feature of the graphite substrate, and not a general property of ^{3}He, as we observed significantly different behaviour for ^{3}He adsorbed on alkali or in a two dimensional environment. In any case no self bound liquid was observed for quasi two dimensional ^{3}He.

The study of helium adsorbed on graphite proves to be challenging, as we observed that small differences in the modellization of the system may lead to qualitative changes in the physical behaviour predicted in simulations. In particular a very accurate description of the interaction between the helium atoms and between helium and graphite is needed to obtain more definitive results. Moreover the effect of the substrate on the helium-helium interaction has never been thoroughly investigated, and may very well have important effects.

We defined an iterative backflow procedure to improve the wave functions used to describe strongly correlated systems. Using these functions it is possible to define a systematic procedure to estimate upper and lower bounds for the ground state energy of a Fermi system, that can be used to estimate the ground state energy, simply including more backflow transformations in the wave function. We used these wave functions to study two dimensional ^{3}He at freezing, obtaining variational estimate significantly more accurate than the available results. The zero variance extrapolations of the upper and lower bounds for the energy allow to obtain an estimate of the ground state energy that is in agreement with the exact Transient Estimate data, when available. Our results in the study of strongly correlated ^{3}He suggest that the iterated backflow procedure can give enough accuracy to estimate the polarization energy of ^{3}He even at high density,

where most of the actual computation can't give accurate results.

The iterative backflow transformations give remarkably good results even when used in the variational description of three dimensional ^{4}He in the ground state, at freezing, equilibrium and at very low density. The energy estimates we obtained compares favourably to Shadow Wave Functions results; the energy extrapolations for the Bose systems give estimate for the ground state energy that are close to exact results. Wave functions that include iterated backflow transformation are in good agreement with exact data not only for the energy but also for other properties, such as pair correlation functions or one body density matrices.

The good results we were able to obtain for both a strongly correlated Fermi liquid and a Bose liquid in different density regimes suggest that these now wave functions are very flexible, and could be used to successfully study a wide array of quantum systems.

Bibliography

[1] M. Ruggeri, S. Moroni and M. Boninsegni, Phys. Rev. Lett. **111**, 045303 (2013)

[2] M. Taddei, M. Ruggeri, S. Moroni and M. Holzmann, Phys. Rev. B. **91**, 115106 (2015)

[3] H. M. Bohm, E. Krotscheck, M. Panholzer, H. Godfrin, H. J. Lauter and M. Meschke, J. Low Temp. Phys **158**, 194 (2010)

[4] D. M. Ceperley, Rev. Mod. Phys. **67**, 279 (1995)

[5] G. Baym, C. Pethik, *Landau Fermi-liquid theory: concepts and applications*, Wiley, 1991

[6] J. Hubbard, Proc. Roy. Soc. A **276**, 238 (1963)

[7] K. Levin and O. T. Valls, Physics Report **98** 1 (1983)

[8] M. T. Béal-Monod, J. Low Temp. Phys. **37**, 123 (1979); err. **39**, 231 (1980)

[9] D. Vollhardt, Rev. Mod. Phys **56**, 99 (1984)

[10] W. L. McMillan, Phys. Rev. A **138**, 442 (1965)

[11] C. J. Umrigar, M. P. Nightingale and K. J. Runge, J. Chem. Phys. **99**, 2865 (2003)

[12] J. B. Anderson, J. Chem. Phys. **65**, 4121 (1976)

[13] V. Grau, J. Boronat and J. Casulleras, Phys. Rev. Lett. **89**, 045301-1 (2002)

[14] B. Krishnamachari and G. V. Chester, Phys. Rev. B **59**, 8852 (1999)

[15] F. Y. Wu and E. Feenberg, Phys. Rev. **128**, 943 (1962)

[16] F. H. Zong, C. Lin and D. M. Ceperley, Phys. Rev. E **66**, 036703 (2002)

[17] N. D. Drummond and R. J. Needs, Phys. Rev. Lett. **102**, 126402 (2009)

[18] M. Holzmann, B. Bernu and D. M. Ceperley, Phys. Rev. B **74**, 104510 (2006)

[19] G. Carleo, S. Moroni, F. Becca and S.Baroni, Phys. Rev. B **83**, 060411 (R) (2011)

[20] M. Nava, A. Motta, D. E. Galli, E. Vitali and S. Moroni, Phys. Rev. B **85**, 184401 (2012)

[21] P. A. Whitlock, G. V. Chester and B. Krishnamachari, Phys. Rev. B **58**, 8704 (1998)

[22] A. D. Novaco and C. E. Campbell, Phys. Rev. B **11**, 2525 (1975)

[23] M. D. Miller and L. H. Nosanow, J. Low Temp. Phys. **32**, 145 (1978)

[24] B. Brami, F. Joly and C. Lhuillier, J. Low Temp. Phys **94**, 63 (1994)

[25] P. A. Whitlock, G. V. Chester and M. H. Kalos, Phys. Rev. B **38**, 2418 (1998)

[26] H. Godfrin and H. J. Lauter, *Progress in Low Temperature physics, Volume XIV*, Chapter 4

[27] W. E. Carlos and M. W. Cole, Surf. Science **91**, 339 (1980)

[28] W. E. Carlos and M. W. Cole, Phys. Rev. B **21**, 3713 (1980)

[29] R. A. Aziz, V. P. S. Nain, J. S. Carley, W. L. Taylor and G. T. McConville, J. Chem. Phys. **70**, 4330 (1979)

[30] R.A. Aziz, F.R.W. McCourt and C.C.K. Wong, Molec. Phys. **61**, 1487 (1987)

[31] T. Korona, H. L. Williams, R. Bukowski, B. Jeziorski and K. Szalewicz, J. Chem. Phys. **106**, 5109 (1997)

[32] J. L. Epstein and E. Krotscheck, Phys. Rev. B **37**, 1666 (1988)

[33] D. S. Greywall, Phys. Rev. B **41**, 1842 (1990)

[34] A. M. Dyugaev, J. Low Temp. Phys. **78**, 79 (1990)

[35] H. Fukuyama, J. Phys. Soc. Jpn. 77, 111013 (2008)

[36] B. K. Bhattacharyya and F. M. Gasparini, Phys. Rev. B **31**, 2719 (1985)

[37] F. M. Gasparini, Physics **5**, 136 (2012)

[38] Y. Matsuyama, D. Tsuji, S. Murakawa, H. Akisato, H. Kambara and H. Fukuyama, J. Low Temp. Phys. **138**, 271 (2005)

[39] D. Sato, K. Naruse, T. Matsui and H. Fukuyama, Phys. Rev. Lett. **109** 235306 (2012)

[40] A. Casey, H. Patel, J. Nyéki, B. P. Cowan and J. Saunders, Phys. Rev. Lett. **90**, 115301-1 (2003)

[41] K. D. Morhard, C. Baüerle, J. Bossy, Yu. Bunkov, S. N. Fisher and H. Godfrin, J. Low. Temp. Phys. **101**, 161 (1995)

[42] K. D. Morhard, C. Baüerle, J. Bossy, Yu. Bunkov, S. N. Fisher and H. Godfrin, Phys. Rev. B **53**, 2658 (1996)

[43] R. B. Hallock, *Progress in Low Temperature physics, Volume XIV*, Chapter 5

[44] G. A. Csàthy, E. Kim and M. H. W. Chan Phys. Rev. Lett. **88**, 045301 (2002)

[45] W. Krauth, *Statistical Mechanics: Algorithms and Computations*, Ed. Oxford

[46] N. Metropolis, A. W. Rosenbluth, M. N. Rosenbluth, A. H. Teller and E. Teller, J. Chem. Phys. **21**, 1087 (1953)

[47] W. K. Hastings, Biometrika **57**, 97 (1970)

[48] C. J. Umrigar, K. J. Wilson and J. W. Wilkins, Phys. Rev. Lett. 60, 1719 (1988)

[49] D. M. Ceperley and M. H. Kalos, *Monte Carlo Method in Statistical Physics*, edited by K. Binder, Topics in Current Physics Vol. 7 (Springer, Berlin, Heidelberg, 1979)

[50] J. Toulouse and C. J. Umrigar, J. Chem. Phys. **126**, 084102 (2007)

[51] M. P. Nightingale and V. Melik-Alaverdian, Phys. Rev. Lett. **87**, 043401 (2001)

[52] C. J. Umrigar, J. Toulouse, C. Filippi, S. Sorella and R. Henning, e-print cond-mat/0611094

[53] D. M. Ceperley and B. Bernu, J. Chem. Phys. **89**, 6316 (1988)

[54] M. H. Kalos, D. Levesque and L. Verlet, Phys. Rev. A **9**, 2178 (1974)

[55] P. A. Whitlock, D. M. Ceperley, G. V. Chester and M. H. Kalos, Phys. Rev. B **19**, 5598 (1979)

[56] M. Rossi, M. Nava, L. Reatto and D. E. Galli, J. Chem. Phys. **131**, 154108 (2009)

[57] A. Sarsa, K. E. Schmidt and W. R. Magro, J. Chem. Phys. **113**, 1366 (2000)

[58] S. Baroni and S. Moroni, Phys. Rev. Lett. **82** 4745 (1999)

[59] W. M. C. Foulkes, L. Mitas, R. J. Needs and G. Rajagopal, Rev. Mod. Phys. **73**, 33 (2001)

[60] J. B. Anderson, J. Chem. Phys. **63**, 1499 (1975)

[61] D. M. Ceperley and B. J. Alder, Phys. Rev. Lett. **45** 566 (1980)

[62] M. Boninsegni and S. Moroni, Phys. Rev. E **86**, 056712 (2012)

[63] P. J. Reynolds, D. M. Ceperley, B. J. Alder and W. A. Lester, J. Chem. Phys. **77**, 5539 (1982)

[64] M. A. Lee, K. E. Schmidt, M. H. Kalos and G. V. Chester, Phys. Rev. Lett. **46**, 728 (1981)

[65] J. W. Moskowitz, K. E. Schmidt, M. A. Lee and M. H. Kalos, J. Chem. Phys. **77**, 349 (1982)

[66] D. M. Ceperley and B. J. Alder, J. Chem. Phys. **81**, 5883 (1984)

[67] J. J. Shepherd, G. Booth, A. Grüneis and A. Alavi, Phys. Rev. B **85**, 081103 (R) (2012)

[68] F. Pederiva, S. A. Vitiello, K. Gernoth, S. Fantoni and L. Reatto, Phys. Rev. B **53**, 15129 (1996)

[69] F. Calcavecchia, F. Pederiva, M. H. Kalos, and T. D. Küne, Phys. Rev. E **90**, 053304 (2014)

[70] K. E. Schmidt and M. H. Kalos, *Applications of the Monte Carlo Method in Statistical Physics*, edited by K. Binder, Topics in Current Physics Vol. 36 (Springer, Berlin, Heidelberg, 1986)

[71] G. Vidali and M. W. Cole, Phys. Rev. B **22**, 4661 (1980)

[72] K. E. Schmidt, M. A. Lee, M. H. Kalos, and G.V. Chester, Phys. Rev. Lett. **47**, 807 (1981)

[73] R. M. Panoff and J. Carlson, Phys. Rev. Lett. **62**, 1130 (1989)

[74] J. Casulleras and J. Boronat, Phys. Rev. Lett. **84**, 3121 (2000)

[75] S. Moroni, S. Fantoni, and G. Senatore, Phys. Rev. B **52**, 13547 (1995)

[76] F.H. Zong, D.M. Ceperley, S. Moroni, and S. Fantoni, Mol. Phys. **101**, 1705 (2003)

[77] Y. Kwon, D. M. Ceperley and R. M. Martin, Phys. Rev. B **48**, 12037 (1993)

[78] Y. Kwon, D. M. Ceperley and R. M. Martin, Phys. Rev. B **58** , 6800 (1998)

[79] M. Holzmann, D. M. Ceperley, C. Pierleoni and K. Esler, Phys. Rev. **E 68**, 046707 (2003)

[80] R. D. Murphy and J. D. Barker, Phys. Rev. **A**, 1037 (1971)

[81] B. M. Axilrod and E. Teller, J. Chem. Phys. **11**, 299 (1943)

[82] L. Vranješ and S. Kilić, J. Low Temp. Phys. **121**,471 (2000)

[83] A. Chizmeshya, M. W. Cole and E. Zaremba, J. Low Temp. Phys. **110**, 677 (1998)

[84] C. Carraro and M. W. Cole, Phys. Rev. B **46**, 10947 (1994)

[85] S. Kilić, E. Krotscheck and L. Vranješ, J. Low temp. Phys. **119**, 715 (2000)

[86] J.-P. Hanses and D. Levesque, Phys. Rev. **165**, 293 (1968)

[87] R. P. Feynman and M. Cohen, Phys. Rev. **102**, 1189 (1956)

[88] R. P. Feynman Phys. Rev. **94**, 262 (1954)

[89] V. R. Pandharipande and N. Itoh, Phys. Rev. A **8**, 2564 (1973)

[90] E. Feenberg, *Theory of Quantum Fluids*, Academic, New York (1969)

[91] E. Krotscheck in *Introduction to modern methods of quantum many-body theory and their applications*, A. Fabrocini, S. Fantoni and E. Krotscheck (ed.), World Scientific Singapore (2002)

[92] G. Temple, Proc. Roy. Soc. A **119**, 276 (1925)

[93] S. Vitiello, K. Runge, G. V. Chester and M. H. Kalos, Phys. Rev. B **42**, 228 (1990)

[94] L. Reatto and G. L. Masserini, Phys. Rev. B **38**, 4516 (1988)

[95] T. McFarland, S. Vitiello, L. Reatto, G. V. Chester and M. H. Kalos, Phys. Rev. B **50**, 13577 (1994)

[96] S. Moroni, D. E. Galli, S. Fantoni and L. Reatto Phys. Rev. B **58**, 909 (1998)

[97] F. Pederiva, A. Ferrante, S. Fantoni and L. Reatto, Phys. Rev. B **52**, 7564 (1995)

[98] R. Rota and J. Boronat, J. Low Temp. Phys. **166**, 21 (2012)